

UNCLASSIFIED

AD NUMBER
AD838870
NEW LIMITATION CHANGE
TO Approved for public release, distribution unlimited
FROM Distribution authorized to U.S. Gov't. agencies and their contractors; Administrative/Operational use; Aug 1968. Other requests shall be referred to Rome Air Development Center, Griffiss AFB NY.
AUTHORITY
RADC, USAE ltr, 17 Sep 1971

THIS PAGE IS UNCLASSIFIED

Best Available Copy

RADC-TR-68-312
Final Report
August 1968



MICROWAVE PROPERTIES OF PARTIALLY MAGNETIZED FERRITES

AD838870

Contractor: Raytheon Company
Contract Number: F30602-68-C-0005
Effective Date of Contract: 23 June 1967
Contract Expiration Date: 23 July 1968
Amount of Contract: \$59,200.00
Program Code Number: 9684

Principal Investigator: J. J. Green, Raytheon
Phone: 617-899-8400 x2475

Project Engineer: P. A. Romanelli, RADC
Phone: 315-330-4251

Sponsored by
Advanced Research Projects Agency
ARPA Order No. 550

THIS DOCUMENT IS SUBJECT TO SPECIAL
EXPORT CONTROLS AND EACH TRANSMITTAL
TO FOREIGN GOVERNMENTS, FOREIGN NA-
TIONALS OR REPRESENTATIVES THERETO MAY
BE MADE ONLY WITH PRIOR APPROVAL OF
RADC (EMATE), GAFB, N.Y.
THE DISTRIBUTION OF THIS DOCUMENT IS
LIMITED UNDER THE U.S. MUTUAL SECURITY
ACTS OF 1949.

Rome Air Development Center
Air Force Systems Command
Griffiss Air Force Base, New York

Best Available Copy

ACCESSION FOR	
CPSTI	WHITE SECTION <input type="checkbox"/>
DDC	DIFF SECTION <input checked="" type="checkbox"/>
UNANNOUNCED	<input type="checkbox"/>
JUSTIFICATION	
BY	
DISTRIBUTION AVAILABILITY CODE	
DICT.	A.A.I.L. ENG. OR SPECIAL
2	

NOTICE

When U. S. Government drawings, specifications, or other data are used for any purpose other than a definitely related government procurement operation, the government thereby incurs no responsibility nor any obligation whatsoever; and the fact that the government may have formulated, furnished, or in any way supplied the said drawings, specifications, or other data is not to be regarded by implication or otherwise, as in any manner licensing the holder or any other person or corporation, or conveying any rights or permission to manufacture, use, or sell any patented invention that may in any way be related thereto.

MICROWAVE PROPERTIES OF PARTIALLY MAGNETIZED FERRITES

J. J. Green

C. E. Patton

F. Sandy

Raytheon Research Division

**THIS DOCUMENT IS SUBJECT TO SPECIAL
EXPORT CONTROLS AND EACH TRANSMITTAL
TO FOREIGN GOVERNMENTS, FOREIGN NA-
TIONALS OR REPRESENTATIVES THERETO MAY
BE MADE ONLY WITH PRIOR APPROVAL OF
RADC (EMATE), GAFB, N.Y. 13440**

**This research was supported by the
Advanced Research Projects Agency
of the Department of Defense and
was monitored by P.A. Romanelli,
RADC (EMATE), GAFB, N.Y. 13440
under Contract No. F30602-68-C-0005**

Best Available Copy

Best Available Copy

FOREWORD

This final report was prepared by the Raytheon Company,
28 Seyon Street, Waltham, Massachusetts 02154 under ARPA Contract
F30602-68-C-0005, ARPA Order 550.

The R C Program Monitor was Patsy A. Romanelli (EMATE).

This report has been reviewed and is approved.

Best Available Copy

ABSTRACT

The microwave properties of partially magnetized materials have been investigated. The real parts (μ' , κ' , μ'_z) of the components of the permeability tensor have been measured as a function of the ratios of saturation magnetization ($4\pi M_s$) to angular frequency (ω) and average magnetization ($4\pi M$) to angular frequency and location on the magnetic hysteresis loop on an yttrium iron garnet (YIG) and magnesium manganese ferrite (MgMnF). The off-diagonal component, κ' , gives good agreement with Rado's prediction that $\kappa' \approx \gamma 4\pi M/\omega$. The diagonal components μ' , μ'_z do not fit Rado's prediction, and the cause of the failure of Rado's analysis for μ' , μ'_z is suggested. The dependence of μ' , μ'_z upon $\gamma 4\pi M/\omega$, $\gamma 4\pi M_s/\omega$ has been empirically fitted by certain mathematical functions. The imaginary components (μ'' , κ'' , μ''_z) have been measured for $0.7 \leq \gamma 4\pi M_s/\omega \leq 1$ using circularly polarized cavities. For $\gamma 4\pi M_s/\omega < 0.8$, it has been found that $\kappa'' \ll \mu''$ and that the loss of the partially magnetized state can be characterized by a single value of μ'' , that for the completely demagnetized state. For values of $\gamma 4\pi M_s/\omega \leq 0.7$ large rectangular samples and exact the solution to the waveguide cavity mode have been utilized to obtain μ'' for the demagnetized state.

The high power threshold has been measured on YIG as a function of sample shape, the polarization of the rf magnetic field, and the orientation of the rf field to the static magnetization. The Suhl and Schlömann theories for high power nonlinearity have been extended to include arbitrary ellipsoids, linearly polarized rf magnetic field, anti-Larmor circularly polarized rf magnetic field, and arbitrary orientation between the rf magnetic field and the static magnetization. The experimental data and the extended theory give good agreement for saturated samples. For thin disk geometries, it has been found that the threshold is very critical to alignment when the dc magnetic field is perpendicular to the plane of the disk. If a needle-like anti-parallel domain structure is assumed for the demagnetized state, then the experimental results for the demagnetized state can be explained in terms of the results of the saturated state.

TABLE OF CONTENTS

	<u>Page</u>
I. GENERAL INTRODUCTION	1
II. PERMEABILITY TENSOR OF PARTIALLY MAGNETIZED MAGNETIC MATERIALS.....	4
A. Introduction.....	4
B. Measurements of μ' and κ'	12
C. Measurements of μ'_z	13
D. Measurements of μ'' and κ''	30
E. Measurements of μ''_z	48
F. Low Magnetic Losses.....	51
III. THE HIGH POWER PROPERTIES OF PARTIALLY MAG- NETIZED MATERIALS	60
A. Introduction	60
B. Experimental Technique and Instrumentation	64
C. Sample Shape and the Perpendicular Pump Threshold	76
D. Parallel and Perpendicular Pumping in Thin Disks.....	85
E. Larmor and Anti-Larmor Pumping in Rod Samples	103
IV. SUMMARY AND CONCLUSIONS.....	108
V. REFERENCES	110
Appendix I - The First-Order Spin-Wave Instability Threshold in Ferromagnetic Insulators of Ellipsoidal Shape with an Arbitrary Pumping Configuration	
Appendix II - Threshold Microwave Field Amplitude for the Unstable Growth of Spin Waves Under Oblique Pumping	

LIST OF FIGURES

<u>Figure</u>	<u>Title</u>	<u>Page</u>
1	Cylindrical TM_{110} Cavity	14
2	Cylindrical TM_{110} Cavity and Sample Mounted in Magnet	15
3	κ' vs $\gamma 4\pi M/\omega$ on G-113 at 5.5 and 9.2 GHz	17
4	μ' vs $\gamma 4\pi M/\omega$ on G-113 at 5.5 GHz	18
5	κ' vs $\gamma 4\pi M/\omega$ on TT1-390 at 5.5 GHz	20
6	μ' vs $\gamma 4\pi M/\omega$ on TT1-390 at 5.5 GHz	21
7	μ' vs $\gamma 4\pi M/\omega$ on TT1-390 at 5.5 GHz	23
8	μ' vs $\gamma 4M/\omega$ on MMF-10 at 5.5 GHz	24
9	μ' vs $\gamma 4\pi M/\omega$ at 9.2 GHz	25
10	μ'_z vs $\gamma 4\pi M/\omega$ on YIG 1 percent Dy at 5.5 GHz	27
11	μ'_z vs $\gamma 4\pi M/\omega$ on MMF-10 at 5.5 GHz	28
12	$\mu''-\kappa''$ and $4\pi M$ vs External Magnetic Field for Unannealed G-113 at 5.5 GHz	32
13	$\mu''-\kappa''$ and $4\pi M$ vs External Magnetic Field for Annealed G-113 at 5.5 GHz	33
14	μ'' vs $\gamma 4\pi M/\omega$ for YIG 1 percent Dy at 5.5 GHz	35
15	κ'' vs $\gamma 4\pi M/\omega$ for YIG 1 percent Dy at 5.5 GHz	36
16	μ'' and κ'' vs $\gamma 4\pi M/\tau$ for TT1-390 at 5.5 GHz	38
17	μ'' vs $\gamma 4\pi M/\omega$ for TT1-390 at 5.5 GHz	39
18	κ'' vs $\gamma 4\pi M/\omega$ for TT1-390 at 5.5 GHz	40
19	μ'' vs $\gamma 4\pi M/\omega$ for MMF-10 at 5.5 GHz	41
20	κ'' vs $\gamma 4\pi M/\omega$ for MMF-10 at 5.5 GHz	42
21	μ'' and κ'' vs ω_M/ω for YIG 1 percent Dy at 5.5 GHz	43
22	μ'' vs ω_M/ω for TT1-390 at 5.5 GHz	44
23	κ'' vs ω_M/ω for MMF-10 at 5.5 GHz	45

LIST OF FIGURES (Cont'd)

<u>Figure</u>	<u>Title</u>	<u>Page</u>
24	μ'' vs ω_M/ω for MMF-10 at 5.5 GHz	46
25	κ'' vs ω_M/ω for MMF-10 at 5.5 GHz	47
26	μ_z'' vs $\gamma 4\pi M/\omega$ for YIG 1 percent DY at 5.5 GHz	49
27	μ_z'' vs $\gamma 4\pi M/\omega$ for MMF-10 at 5.5 GHz	50
28	Subthreshold μ_z'' vs Frequency	52
29	Rectangular TE ₁₀₂ Cavity for Measuring Very Low μ''	54
30	μ'' vs ω_M/ω at $4\pi M = 0$ for Low Loss Materials	59
31	Block Diagram of the Microwave System and General Instrumentation for the Semiautomatic System for Determining Instability Threshold Fields.	67
32	Schematic Representation of the Relevant Pulse Sequences for Operation of the Semiautomatic System.	68
33	Block Diagram of the Electronic Instrumentation for Semiautomatic System	70
34	Sample Recorder Outputs of the Cavity Reflection Coefficient as a Function of Microwave Field Amplitude.	72
35	Photograph of the Alignment Apparatus Utilized in Obtaining Data on Disk-Shaped Samples.	74
36	Threshold Field h_{crit} as a Function of the Static External Field H_0 for Perpendicular Pumping with H_0 Normal to the Disk with the Misalignment Angle Between H_0 and the Disk Normal as a Parameter.	75
37	Threshold Field h_{crit} as a Function of the Static External Field H_0 for Axially Magnetized 40-mil Diam Rods, 1 mm Diam Spheres, and Normally Magnetized 10-mil Thick, 1 cm Diam Disks, Before and After a 1 hr Anneal at 1200°C	77
38	Threshold Field h_{crit} as a Function of the Static External Field H_0 for the Annealed Spherical Sample of Fig. 7 and Both Parallel and Perpendicular Pump Configurations	79
39	(a) Spinwave Linewidth ΔH_k as a Function of Spinwave Angle θ_k for Parallel and Perpendicular Pumping and Wavenumber k Equal to Zero; (b) ΔH_k vs k for Parallel Pumping ($\theta_k = \pi/2$) and Perpendicular Pumping ($\theta_k \approx \pi/4$).	80

LIST OF FIGURES (Cont'd)

<u>Figure</u>	<u>Title</u>	<u>Page</u>
40	Threshold Field h_{crit} as a Function of the Static External Field H_0 as in Fig. 7 for the Annealed Rod, Sphere, and Disk Samples.	82
41	Summary of the Various Pump Configuration Examined for the Disk-Shaped Samples	87
42	Threshold Field h_{crit} as a Function of the Static External Field H_0 for the (1, 1, 1) Configuration.	88
43	Threshold Field h_{crit} as a Function of the Static External Field H_0 for the (1, 1, 1) Configuration.	89
44	Threshold Field h_{crit} as a Function of the Static External Field H_0 for the (1, 1, 1) Configuration.	90
45	Threshold Field h_{crit} as a Function of the Static External Field H_0 for the (1, 1, 1) Configuration.	91
46	Threshold Field h_{crit} as a Function of the Static External Field H_0 for the (1, 1, 1) Configuration.	92
47	Threshold Field h_{crit} as a Function of the Static External Field H_0 for the (1, 1, 1) Configuration with Static Field H_0 Less than 200 Oe.	94
48	Threshold Field h_{crit} as a Function of the Static External Field H_0 for a 10 Mil Disk and the (1, 1, 1) Configuration.	97
49	The Threshold Field, Relative to the Value at $H_0 = 0$ with H_0 Increasing, as a Function of Static External Field for 75 Mil Diam Rods and Circular Polarized Perpendicular Pump Excitation.	105
50	The Threshold Field, Relative to the Value at $H_0 = 0$ with H_0 Increasing, as a Function of Static External Field Circular Polarized Perpendicular Pump Excitation.	106

I. GENERAL INTRODUCTION

Great impetus has been given to ferrite device development in recent years by the phased array radar development. The average phased array antenna requires several thousand phase-shifting elements. These elements must be cheap, reliable, all identical, and of course have acceptable operating characteristics such as low insertion loss, a certain peak power capability, low drive power for phase setting, rapid phase switching, bandwidth, and a capability to operate over a wide temperature environment. The drive power requirement has essentially limited consideration to those devices where the magnetic material is partially magnetized. Devices in which the ferrite is latched into the remanent state have been particularly popular. These devices have been waveguide, coax, strip-line, and, most recently, microstrip geometries. This latter geometry is receiving a great deal of attention today because of its application in microwave integration and miniaturization.

The requirements on these devices offer a challenge to both the microwave designer and materials physicist. Results to date indicate that there is a real need for clever design and for better materials. The results also indicate there is a need for a better understanding of how material characteristics affect device performance. But this is not possible if the material characteristics of partially magnetized materials are not known. Therefore, the goal of our program is to experimentally determine, and when possible to create a theoretical model of the significant microwave characteristics of partially magnetized materials.

A question frequently posed by the microwave designer to the materials physicist is: what is the optimum ratio of saturation magnetization ($4\pi M_s$) to operating frequency (ω) to obtain the minimum insertion loss? Or, in general, how does insertion loss vary with $\gamma 4\pi M_s / \omega$ in a 360° phase shifter? We have a vague idea how this may vary in some nonreciprocal geometries

but no inkling of how it may vary in a reciprocal geometry. This is a particularly difficult question since changing $\gamma_4\pi M_s$ means changing composition and ceramic microstructure. These are two variables to which magnetic loss is very sensitive. Consequently, in this program we have put a strong emphasis on temperature and frequency measurements in which composition and ceramic microstructure are held constant.

Designing for low insertion loss is further complicated by peak power requirements. Since peak power threshold and insertion loss are dependent upon similar relaxation mechanisms, low insertion loss usually means low peak power performance. Techniques for improving the peak power capability of a material frequently result in an increase of insertion loss. Therefore, it is important to understand the source of the peak-power nonlinearity in each type of device structure. To do this we must first have some idea of the field distribution in the device and second must understand how the nonlinearity threshold for partially magnetized materials depends upon the type of rf polarization (linear, elliptical, circular), the angle between the rf field and the dc magnetization and the sample geometry. Clearly device configurations that locate material in regions of low peak power threshold and low phase shift activity are undesirable. Such a situation can occur in latching phase shifters where it is necessary to include magnetic material within the microwave structure for the purposes of providing a closed dc magnetic path. Such material can contribute little to the phase-shifting properties but can be the source of the peak power instability

An eventual goal of this program is a handbook of the microwave properties of partially magnetized materials which could be used in computer-aided device design. Theory now exists that permits some such design on nonreciprocal waveguide phase shifters and junction circulators. Computer design of these geometries and other geometries for which a suitable theoretical approach is developed can optimize performance more quickly and cheaply than the present laboratory approach. In such a handbook, it would be desirable to classify the phase shifting, insertion loss, and peak power performance as a function of all the compositional and microstructure parameters.

Unfortunately, our present understanding of the effect of microstructure and composition upon loss and critical power level is not sufficiently well developed to allow such a classification within the resources of the present program. A more realistic approach is to measure the phase shifting, loss, and critical power characteristics of the most popular commercial phase shifting materials. Then the handbook will permit computer-aided design with today's materials. Such design will be a valuable feedback for future material development.

This report describes the progress during the first year of this program and is divided into two parts. The first part deals with the low power determination of the real and imaginary parts of the components of the permeability tensor, the second with high power measurements as a function of geometry, polarization, and pumping angle. In both phases of our investigation established experimental techniques were employed. However, certain modifications and innovations were required either because the material was partially magnetized or because of the novel geometry. Since these modifications and innovations comprised a significant portion of our effort during the first year of this program, they are described in detail. The remainder of our effort involved measurements on three materials: G-113 (YIG), TT1-390 (MgMnF), and MMF-10 (MgMnF). In a certain sense these three materials have been trial horses. The usual problems of drift, temperature control, sensitivity, reproducibility, etc., have been worked out in the process of measuring these materials.

II. PERMEABILITY TENSOR OF PARTIALLY MAGNETIZED MAGNETIC MATERIALS

A. Introduction

Much work has been done in recent years to develop microwave devices such as phase shifters and circulators that operate in partially magnetized states. These states include all those from the completely demagnetized state to the remanent state and even slightly higher using small additional bias fields. In addition to the experimental investigations of these devices, various geometries have been theoretically¹ examined and computer programs exist which describe the performance of the device in terms of the components of the permeability tensor of the ferrimagnetic materials in them. Unfortunately, information² available in the literature describes only in broad generalities how these tensor components depend on the state of magnetization, and the saturation magnetization of the material and the operating frequency. However, these computer programs need numerical values, preferably in a functional form, so that numerous cases can be evaluated and device geometry and magnetic materials can be optimized. Thus one of the objectives of this program is to describe quantitatively how the permeability tensor, including both its real and imaginary parts, varies as one moves about the magnetic hysteresis loop and as one varies frequency and saturation magnetization.

When a magnetic material is placed in a small rf magnetic field an rf magnetization, $4\pi\bar{m}$, is produced, having components related to those of the driving rf magnetic field, \bar{h} , by a tensor permeability $\bar{\mu}$

$$4\pi\bar{m} = (\bar{\mu} - 1) \cdot \bar{h}$$
$$\bar{\mu} = \begin{pmatrix} \mu_{xx} & \mu_{xy} & \mu_{xz} \\ \mu_{yx} & \mu_{yy} & \mu_{yz} \\ \mu_{zx} & \mu_{zy} & \mu_{zz} \end{pmatrix}$$

Since a polycrystalline material exhibits rotational symmetry about the direction of magnetization, which we may take as the z direction, this tensor takes the simpler form:

$$\bar{\mu} = \begin{pmatrix} \mu & -j\kappa & 0 \\ j\kappa & \mu & 0 \\ 0 & 0 & \mu_z \end{pmatrix}$$

having only three independent quantities μ , κ , and μ_z . Each of the components of these tensors will, in general, be complex:

$$\mu = \mu' - j\mu''$$

$$\kappa = \kappa' - j\kappa''$$

$$\mu_z = \mu'_z - j\mu''_z$$

The real parts of these components produce dispersion, while the imaginary parts produce absorption.

If the material is saturated by a variable internal magnetic field H in the z direction, the elements μ and κ undergo a resonance at a field ω/γ where γ is approximately 2.8 Oe/MHz. The line shape of this resonance has been analyzed³ and is outside the scope of this work. We are interested only in the region where H approaches zero and the sample is not completely magnetized. If the internal magnetic field could be reduced to exactly zero without any demagnetization taking place, the theories applicable to saturated materials would still be applicable and we would have

$$\mu' = 1$$

$$\mu'_z = 1$$

$$\kappa' = \omega_M/\omega \text{ where } \omega_M = \gamma 4\pi M_s$$

In practice however, this state can never be attained experimentally, since at zero internal field the magnetization has dropped from its saturation value to its remanence value, which is usually substantially lower. Values of magnetization somewhat higher than remanence, but still below saturation, can be obtained with magnetic fields small enough not to contribute significantly to the permeability themselves.

In the partially magnetized state the imaginary parts of permeability components become very large if $\omega_M/\omega \geq 1$, producing what is called "low field loss." This effect has been explained by Polder and Smit.⁴ Because of it, ferrite devices that operate in the partially magnetized state always operate with $\omega_M/\omega < 1$.

A theory of Rado⁵ states that if $\omega_M/\omega \ll 1$, μ' and μ'' are both equal to 1.0 for all unsaturated states and $\kappa' = \gamma 4\pi M/\omega$ where $4\pi M$ is the microscopic magnetization averaged over the domains. Although it has been generally accepted that Rado's theory for κ' is a good approximation even as ω_M/ω gets fairly close to 1.0, the theory for μ' and μ'' is valid only in the limit $\omega_M \rightarrow 0$. Rado's results are derived by averaging the torque equation

$$4\pi \overline{\mathbf{M}} = \gamma 4\pi \overline{\mathbf{M}} \times \overline{\mathbf{H}} \quad (1)$$

over the sample. By making several assumptions, including $\omega_M/\omega \ll 1.0$, on the relative size of various components of the magnetization $4\pi M$ and the magnetic field H , he reduced the torque equation at a given point in the material to

$$4\pi \overline{\mathbf{m}} = i \frac{\gamma 4\pi M_s}{\omega} \overline{\mathbf{h}} \times \overline{\mathbf{u}} \quad (2)$$

Here $\overline{\mathbf{u}}$ is a unit vector in the direction of the static magnetization in the domain in question, $4\pi \overline{\mathbf{m}}$ is the rf magnetization, and $\overline{\mathbf{h}}$ is the rf magnetic

field. The field \bar{h} includes a spatially constant part consisting of the applied rf drive field less the demagnetizing fields from the sample boundary and a spatially fluctuating component due to demagnetizing fields from poles on the domain and grain boundaries. Although the spatial average over the sample of this fluctuating field is zero, it is the source of the deviations of μ' and μ'_z from 1.0 as well as the small deviations in κ' from $\gamma 4\pi M/\omega$ which we have observed in some materials. Unfortunately Rado did not take into account the effect of this spatially fluctuating field.

When $\omega_M/\omega \ll 1$, these spatially fluctuating fields become small and hence Rado's results become more accurate. The condition $\omega_M/\omega \ll 1$ was not required, however, at the point where he invoked it, namely in simplifying the torque equation.

In order to derive a bulk susceptibility from the point relationship, Eq. (2), one must take a spatial average of Eq. (2) over the whole sample

$$\langle 4\pi\bar{m} \rangle_{av} = i \frac{\gamma 4\pi M_s}{\omega} \langle \bar{h} \times \bar{u} \rangle_{av} \quad (3)$$

By writing

$$\bar{h} = \langle \bar{h} \rangle_{av} + \delta\bar{h}$$

$$\bar{u} = \langle \bar{u} \rangle_{av} + \delta\bar{u}$$

where $\delta\bar{h}$ and $\delta\bar{u}$ are the spatially fluctuating components of \bar{h} and \bar{u} , one obtains with a small amount of manipulating

$$\langle \bar{h} \times \bar{u} \rangle_{av} = \langle \bar{h} \rangle_{av} \times \langle \bar{u} \rangle_{av} + \langle \delta\bar{h} \times \delta\bar{u} \rangle_{av} \quad (4)$$

The error in Rado's theory is his assertion that $\delta\bar{h}$ and $\delta\bar{u}$ are uncorrelated and hence $\langle \delta\bar{h} \times \delta\bar{u} \rangle_{av} = 0$. Using this assumption, and the fact that $\langle \bar{u} \rangle_{av} = 4\pi\bar{M}/4\pi M_s$, Rado's results that $\mu' = \mu'_z = 1.0$ and $\kappa' = 4\pi M/\omega$ are easily obtained.

It will be shown below that the assumption that $\delta\bar{u}$ and $\delta\bar{h}$ are uncorrelated is incorrect. The demagnetizing fields from poles on domain and grain boundaries far from the point in question average to zero and hence do not contribute to $\delta\bar{h}$. The fields from poles close to the point in question but not on its own domain or grain boundary contribute to $\delta\bar{h}$ and may be reasonably uncorrelated with $\delta\bar{u}$. It is the field due poles on the boundary of the domain or grain in question, which is a substantial part of $\delta\bar{h}$, that is strongly correlated to $\delta\bar{u}$. These poles are produced by the rf magnetization of the domain which is precessing about a direction determined in large part by \bar{u} (as well as by the domain shape). If we change the direction of the \bar{u} , the precessional path of the rf magnetization will change with it and hence demagnetizing field of that domain or grain which is contributing to $\delta\bar{h}$ will change. Thus $\delta\bar{h}$ is correlated with $\delta\bar{u}$.

If we look at an oversimplified picture of a single domain we can see why this neglect of correlation produces errors primarily in μ' and μ'_2 rather than in κ' . We will consider the domain to be an ellipsoid of revolution about the direction of \bar{u} . We will also consider only the contribution to $\delta\bar{h}$ is from the poles on its own boundary. All other demagnetizing fields, including those from adjacent domains and grains, are assumed to sum to zero. The precessing magnetization driven by the applied field $\langle\bar{h}\rangle_{av}$ will have two orthogonal components in the plane perpendicular to $\delta\bar{u}$. These are in the directions of $\delta\bar{u} \times \langle\bar{h}\rangle_{av}$ and $\delta\bar{u} \times (\delta\bar{u} \times \langle\bar{h}\rangle_{av})$. The rf magnetization will produce a $\delta\bar{h}$ in the same direction as the rf magnetization and related to it by the transverse demagnetizing factor of the ellipsoid. In computing the average $\langle\delta\bar{u} \times \delta\bar{h}\rangle_{av}$ we will thus have terms proportional to

$$\delta\bar{u} \times (\delta\bar{u} \times \langle\bar{h}\rangle_{av}) \text{ and } \delta\bar{u} \times (\delta\bar{u} \times (\delta\bar{u} \times \langle\bar{h}\rangle_{av})) \quad (5)$$

We now assume further that, for each domain like the one under consideration, there is one of the same shape with opposite $\delta\bar{u}$. This assumption is probably not exactly true since only the average value of $\delta\bar{u}$ is zero. It is

not necessary there be an equal number of domains with $\pm \delta \bar{u}$ of each size and shape. However, within the framework of this assumption we see the following. If we change the sign of $\delta \bar{u}$ in the term above containing the series of cross products with three $\delta \bar{u}$'s, the sign of the term changes and hence its average over the sample is zero. However, the average $\langle \delta \bar{u} \times \delta \bar{h} \rangle_{av}$ still contains the remaining term $\langle \delta \bar{u} \times (\delta \bar{u} \times \langle \bar{h} \rangle_{av}) \rangle_{av}$ which is not zero. Applying a vector identity to this term gives

$$\delta \bar{u} \times (\delta \bar{u} \times \langle \bar{h} \rangle_{av}) = (\delta \bar{u} \cdot \langle \bar{h} \rangle_{av}) \delta \bar{u} - (\delta \bar{u} \cdot \delta \bar{u}) \langle \bar{h} \rangle_{av} \quad (6)$$

We can define the x direction so that $\langle \bar{h} \rangle_{av}$ is in the x-z plane. Taking the average of the first term on the right side of Eq. (6) above over all domains gives

$$\langle \delta \bar{u} \cdot \langle \bar{h} \rangle_{av} \rangle_{av} \delta \bar{u} = \langle \delta u_x^2 \rangle_{av} \hat{x} + \langle \delta u_z^2 \rangle_{av} \langle \bar{h} \rangle_{av} \hat{z} \quad (7)$$

where \hat{x} and \hat{z} are unit vectors in the x and z directions. The average of of the second term in Eq. (6) is just

$$\langle (\delta \bar{u} \cdot \delta \bar{u}) \langle \bar{h} \rangle_{av} \rangle_{av} = \langle |\delta u|^2 \rangle_{av} (\langle h_x \rangle_{av} \hat{x} + \langle h_z \rangle_{av} \hat{z}) \quad (8)$$

Combining these averages with Eqs. (3) and (4) gives contributions to the rf magnetization of

$$\begin{aligned} \langle 4\pi m_x \rangle_{av} &= (\mu' - 1) \langle h_x \rangle_{av} \\ \langle 4\pi m_z \rangle_{av} &= (\mu'_z - 1) \langle h_z \rangle_{av} \end{aligned} \quad (9)$$

where

$$\begin{aligned} (\mu' - 1) &\propto \langle \delta u_x^2 \rangle_{av} - \langle |\delta u|^2 \rangle_{av} \\ (\mu'_z - 1) &\propto \langle \delta u_z^2 \rangle_{av} - \langle |\delta u|^2 \rangle_{av} \end{aligned} \quad (10)$$

The constant of proportionality depends on the appropriate susceptibility term of an isolated magnetic moment $\delta\bar{u}$ times its average transverse demagnetizing factor. No additional contribution to κ' is made in this approximation. It must be emphasized again that very rough approximations are made in this paragraph and that κ' may be expected to deviate from Rado's theory, but the deviation is less than that for μ' and μ'_z .

It should also be emphasized that there is no a priori reason for the components of the permeability to be unique functions of the dc magnetization. States having the same magnetization but on opposite sides of B-H hysteresis curve have different domain structures, and hence the spatial average $\langle \delta\bar{u} \times \delta\bar{h} \rangle_{av}$ should not be expected to be the same for them. The differences, however, are second-order effects as are the deviations of κ' from Rado's theory.

Other authors^{6,7} have theoretically considered the permeability of partially magnetized ferrites from a superficially different point of view. They start with the tensor permeability of a randomly oriented domain and average over-all orientations arriving at the same result as Rado. This is to be expected since their tensor permeability is derived from the same torque equation Rado used, and they too neglected the spatially fluctuating rf magnetic field within the material.

It has not yet been possible to evaluate the average $\langle \delta\bar{u} \times \delta\bar{h} \rangle_{av}$ in terms of a physical model of the domain structure and hence give explicit formulae for μ' and μ'_z . In this report we therefore present graphs of our measurements, along with phenomenological formulae for use in device design.

A separate theoretical analysis of μ' and μ'_z in the totally demagnetized state (where they are equal) was made by Sandy and Green⁸ in which a somewhat different approach was taken. The spatially fluctuating rf fields were treated in the manner used by Polder and Smit⁴ to explain low-field loss

when $\omega_M/\omega > 1.0$. They showed that these demagnetizing fields cause the domains to undergo ferromagnetic resonance at frequencies from zero to ω_M . While we are concerned with the region $\omega_M/\omega < 1.0$, it is the high frequency tails of these resonances that make μ' and μ'_z differ from 1.0. Using this approach, the domains were assumed to have an unknown distribution function $D(\omega_R)$ of resonant frequencies between zero and ω_M and that each of these resonances was Lorentzian in shape. By integrating various guesses of $D(\omega_R)$ times the Lorentzian lineshape, it was found that the frequency dependence of the permeability above ω_M was not strongly dependent on the choice of distribution function, and reasonable functions were found that fit experimental data on the frequency dependence of the initial permeability of several ferrites. However, no single distribution function fit all ferrites, indicating the presence of significantly different types of domain and grain structures.

In considering interactions between magnetic moments and magnetic fields, it is generally valid to scale all magnetizations and fields to ω/γ . Thus the question immediately arises whether μ' and μ'_z depend on $4\pi M$, $4\pi M_s$, and ω independently or only on the two ratios $\gamma 4\pi M/\omega$ and $\gamma 4\pi M_s/\omega$. This suggested dependence was confirmed experimentally for $\gamma 4\pi M_s/\omega$ in the work cited earlier.⁸ Further confirmation for $\gamma 4\pi M/\omega$ will be given later in this report.

We have also studied, experimentally, the imaginary parts of the permeability tensor, μ'' , μ''_z , and κ'' . In addition to all factors important for the real parts, the imaginary parts depend on the intrinsic loss mechanism of the material and hence on chemical composition, impurities, and temperature. They also depend strongly on the degree of internal strain in the crystal structure. This shows up as large surface losses in machined samples that have not been annealed to relieve strains caused by machining.

Our measurements to date have been primarily on two commonly used commercial ferrites made by Trans Tech: G-113, an yttrium iron garnet with $4\pi M_s = 1750$ gauss at room temperature; TT1-390, a magnesium

manganese spinel with $4\pi M_s = 2150$ gauss at room temperature; and on MMF-10, another commercial magnesium manganese spinel, made by Airtron, having a $4\pi M_s = 2400$ gauss at room temperature. This latter material was included because it contains no second phase while a substantial amount is present in TT1-390, and it was desired to determine if this was a major factor in any of the observed properties. Measurements were also made on YIG with 1 percent Dy in order to improve the sensitivity of the loss measurement. Most of our measurements were made at 5.5 GHz where ω_M/ω was close to 1.0 for all three materials at room temperature. By heating the samples, ω_M/ω could be continuously reduced as the Curie temperature was approached. It is assumed that the prime effect of heating on μ' , μ_z' , and κ' arises from the changes in ω_M/ω . Other less important changes may occur due to changes in factors that affect the domain structure. Some evidence, including measurements on other materials at 9.20 GHz and room temperature, will be presented showing that these effects are small. The direct effect of temperature on intrinsic loss parameters on the other hand, is not small. However, the dependence of μ'' , μ_z'' , and κ'' on ω_M/ω is so drastic when ω_M/ω is only slightly < 0.1 that the temperature dependence of the intrinsic loss parameters causes a relatively small change in them. To eliminate this effect, measurements are also being made on μ'' in the demagnetized state at room temperature with frequency, ω , varied and ω_M held constant. In that case the losses will contain the frequency dependence rather than the temperature dependence of the relaxation rate.

B. Measurements of μ' and κ'

To measure μ' and κ' , we have used a cylindrical TM_{110} cavity similar to that used by LeCraw and Spencer.² The sample, a 0.075 in. diam rod, is mounted along the axis of the cavity. The cavity supports two degenerate modes which are split into left and right circularly polarized modes whenever $\kappa' \neq 0$. The frequencies of these two modes are related to $\mu' + \kappa'$ and $\mu' - \kappa'$, respectively. The cavity has four symmetrically placed irises. By feeding two orthogonal ports $\pm 90^\circ$ out of phase, either mode

could be excited separately. To improve the degeneracy of the cavity, a ring of eight tuning screws was placed in one end of the empty cavity, as seen in Fig. 1.

The cavity was mounted with the sample rod between the pole faces of a variable gap electromagnet as shown in Fig. 2. By closing the gap until the pole faces nearly contacted the rod, the demagnetizing poles on the ends of the rod were nearly eliminated and uniformity of the magnetization is improved. The rods used for the measurements at 5.5 GHz were 3 in. long; those used at 9.2 GHz were 2 in. long. The 5.5 GHz measurements were made as a function of temperature in order to vary $4\pi M_s$ and hence ω_M/ω .

In order to know the magnetization of the rod, as the field of the electromagnet was swept, a 2000 turn pickup coil was placed around the rod just outside the cavity. This coil was wired in series with an adjacent 2000 turn coil not containing the sample, wound in the opposite direction in order to buck the flux of the magnet's H field. The two coils were connected to an integrator whose output was proportional to the magnetization of the rod. By mounting the rod and coil in the magnet gap without the cavity and moving the coil along the rod, we found the magnetization over the parts of the rod normally in the cavity or the coil was constant within a few percent for the 3 in. rods and somewhat worse for the 2 in. rods.

The cavity frequency was obtained as a function of magnetization as the magnetization was cycled about a major hysteresis loop, by making the cavity part of a Pound discriminator locking the klystron to the cavity. The correction voltage, fed to the klystron reflector, was calibrated to the klystron frequency and plotted vs the output of the integrator on an x-y recorder. This was done for both circular polarization modes of the cavity. From these two frequencies, the values of μ' and κ' could be computed as a function of magnetization. This could be done either by perturbation theory as described by LeCraw and Spencer² or by an exact solution given by Bussey and Steinert.⁹ The two methods are nearly equivalent at 5.5 GHz where

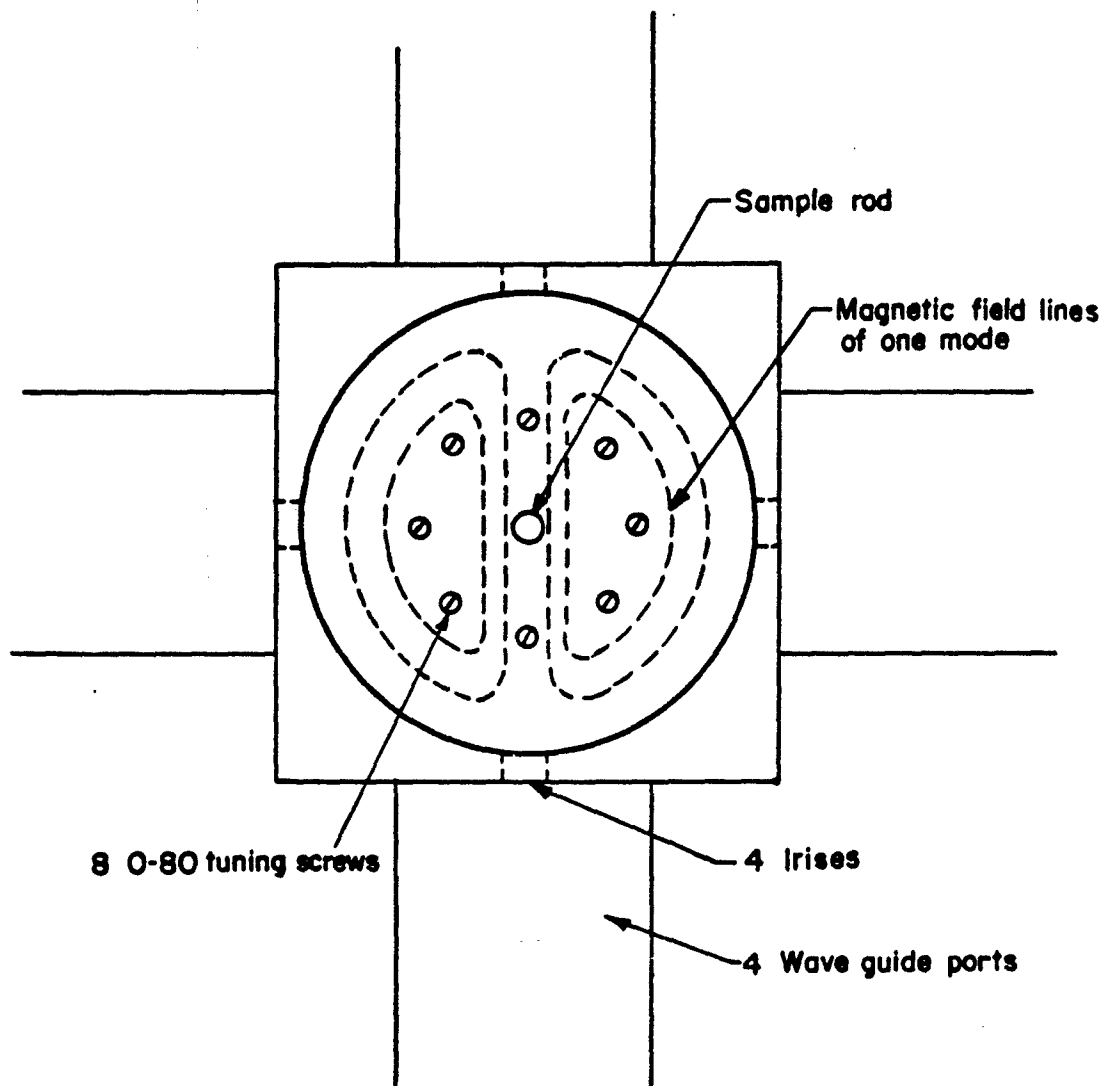


Fig. 1 Cylindrical TM_{110} Cavity

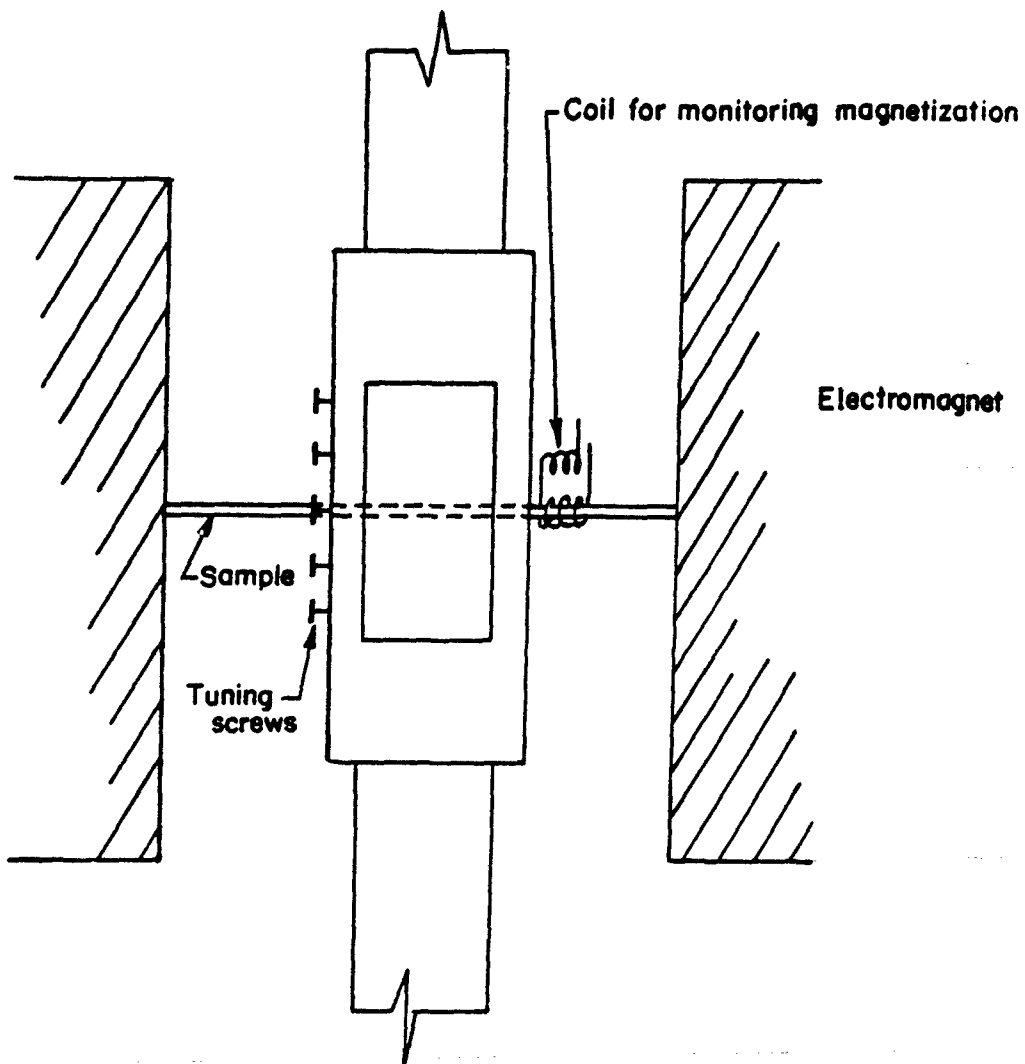


Fig. 2 Cylindrical TM_{110} Cavity and Sample Mounted in Magnet

most of our measurements were made. However, at 9.2 GHz the 0.075 in. rods are too large for perturbation theory to be accurate. We have thus written our data reduction computer programs to use the exact solution.

Measurements of μ' and κ' on MMF-10 were obtained as a by-product of measurements on μ'' and κ'' using a different technique described in Sec. D.

The results of the measurement of κ' vs magnetization on G-113 were reasonably consistent with Rado's theory. The measured values of κ' were generally a bit higher than theoretically expected with the greatest deviations (less than 0.05) occurring at $\gamma 4\pi M/\omega \approx 0.4$. This can be seen in Fig. 3 for κ at room temperature at 5.5 GHz and 9.2 GHz. The deviations were similar at all temperatures at 5.5 GHz, and no real dependence of ω_M/ω could be found. Of significance, however, was the fact that for G-113 there was no dependence of κ' on hysteresis. Although not equal exactly to $\gamma 4\pi M/\omega$, it was a unique function of it.

The measured dependence of μ' and $\gamma 4\pi M/\omega$ and $\gamma 4\pi M_s/\omega$ for G-113 at 5.5 GHz is shown in Fig. 4. $4\pi M_s$ is varied by changing temperature. Again there is no dependence on hysteresis history.

The solid curve in this figure is the function

$$\mu' = \mu'_0 + (1 - \mu'_0) \frac{\tanh(1.25 (M/M_s)^2)}{\tanh(1.25)} \quad (11)$$

where μ'_0 is the value of μ' when $4\pi M = 0$. It can be seen that this function fits the data reasonably well over the entire range of values of $\gamma 4\pi M/\omega$ and $\gamma 4\pi M_s/\omega$. While this functional relationship has no physical significance, it is intended to be useful in optimizing microwave ferrite devices with the aid of computer programs. The deviation of the data from the solid curve at the highest temperature (lowest ω_M/ω) is at least in part due to temperature gradients in the cavity. The point on the outside of the cavity at which

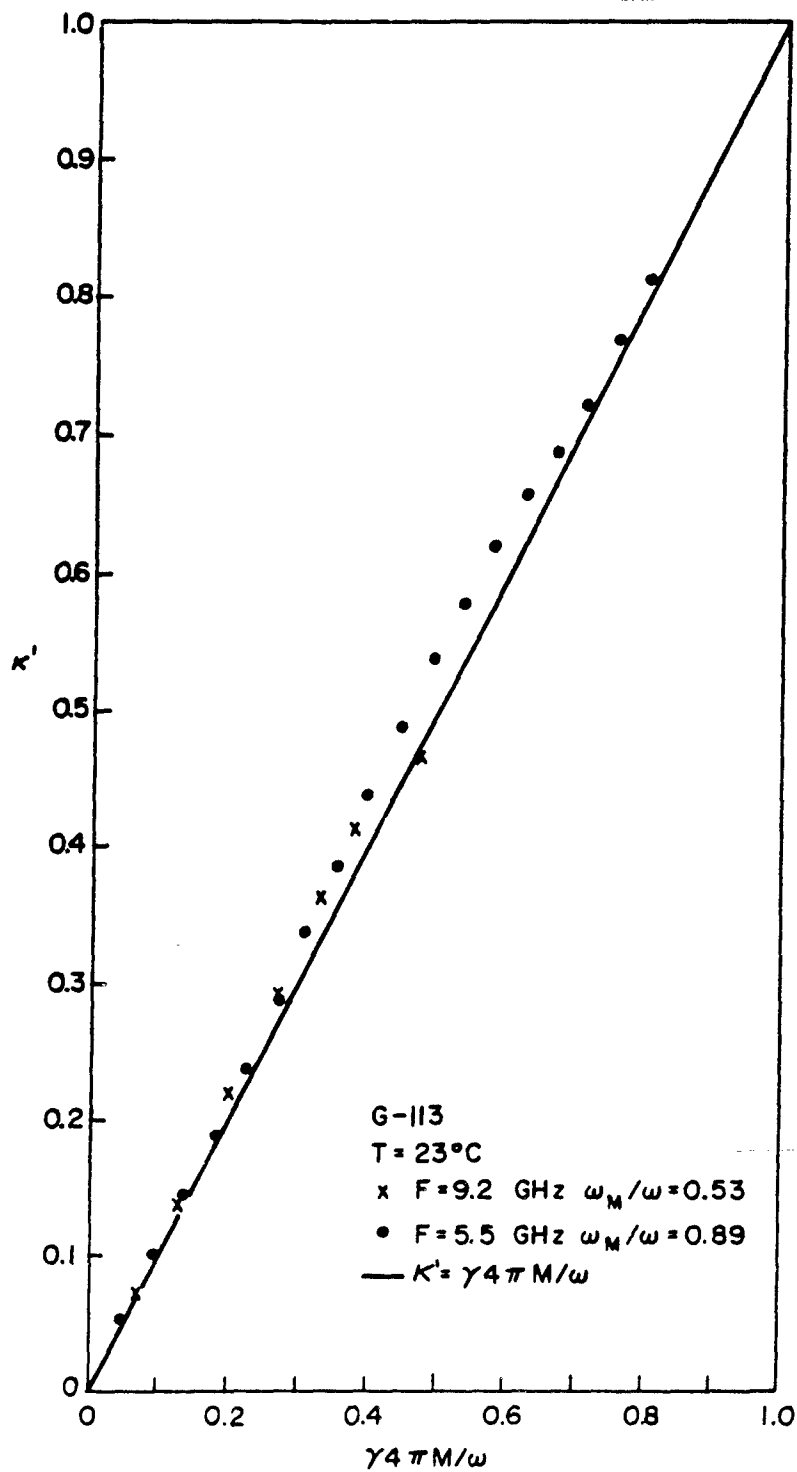


Fig. 3 κ' vs $\gamma 4\pi M/\omega$ on G-113 at 5.5 and 9.2 GHz

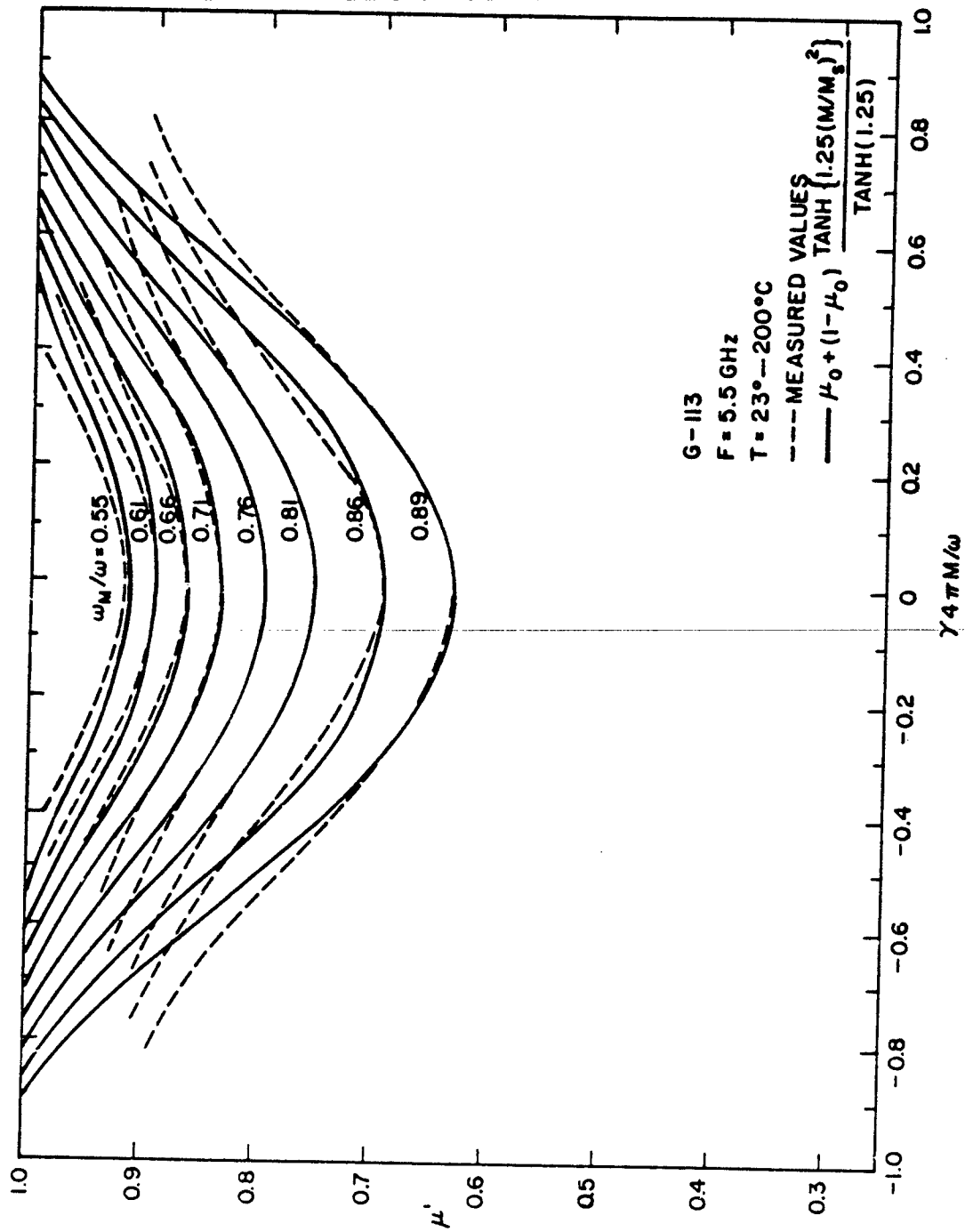


Fig. 4 μ' vs $\gamma 4\pi M/\omega$ on G-113 at 5.5 GHz

our thermocouple was attached may have been a few degrees cooler than the sample inside the cavity. As a result the end point of the solid curves is at too high a value of $\gamma 4\pi M/\omega$ for the actual ω_M/ω of the sample.

In making use of the values of ω_M/ω quoted for each curve in this and subsequent figures, it should be remembered that due to uncertainties in the materials' g factor, and hence in γ , and due to errors in the measurement of $4\pi M_s$, there will be errors of a few percent in ω_M/ω .

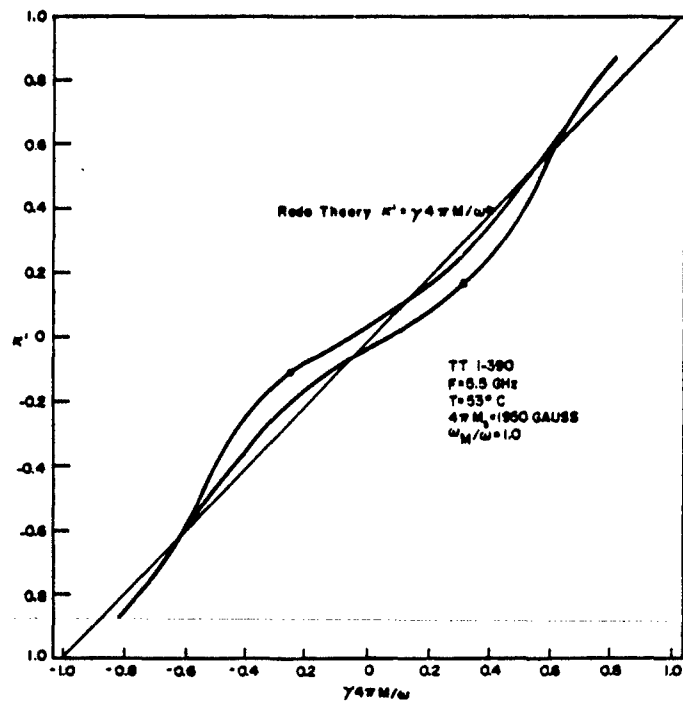
In an earlier report we fit this data with a simpler function:

$$\mu' = \mu'_c \cdot (1 - \mu'_0)(M/M_s)^{3/2} \quad (12)$$

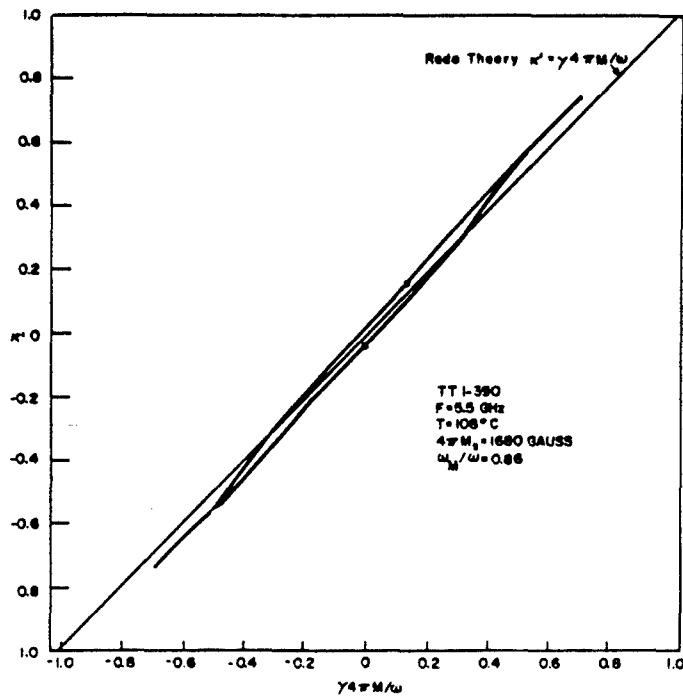
The function in Eq. (11) does not give a better fit than the one in Eq. (12). However, it does give a reasonable fit to the data for TT1-390 and MMF-10 as well as for G-113 which the simpler function failed to do.

At the highest values of $4\pi M$ shown for each curve in this figure, the internal field is about 50 Oe. As a result, there is a small contribution to μ' from the low-field tail of the ferromagnetic resonance curve. This reduces μ' below that produced by its domain structure alone and prevents μ' from approaching 1.0 as $4\pi M$ approaches $4\pi M_s$.

The measurements made on TT1-390, a magnesium-manganese spinel, showed quite different results. At values of ω_M/ω close to 1.0 both μ' and κ' showed significant dependence on hysteresis history rather than depending on magnetization alone. This can be seen in Figs. 5 and 6. This dependence decreases as ω_M/ω decreases but a residual amount was detectable at all temperatures. It should be noted that on major hysteresis loops the two crossings at $4\pi M = 0$ yield the same value of μ' , while the values of κ' are equal in magnitude but opposite in sign. This results from a symmetry of the permeability tensor which requires that μ be an even function of magnetization and its hysteresis while κ is an odd function.



(a)



(b)

Fig. 5 κ' vs $\gamma 4\pi M/\omega$ on TT1-390

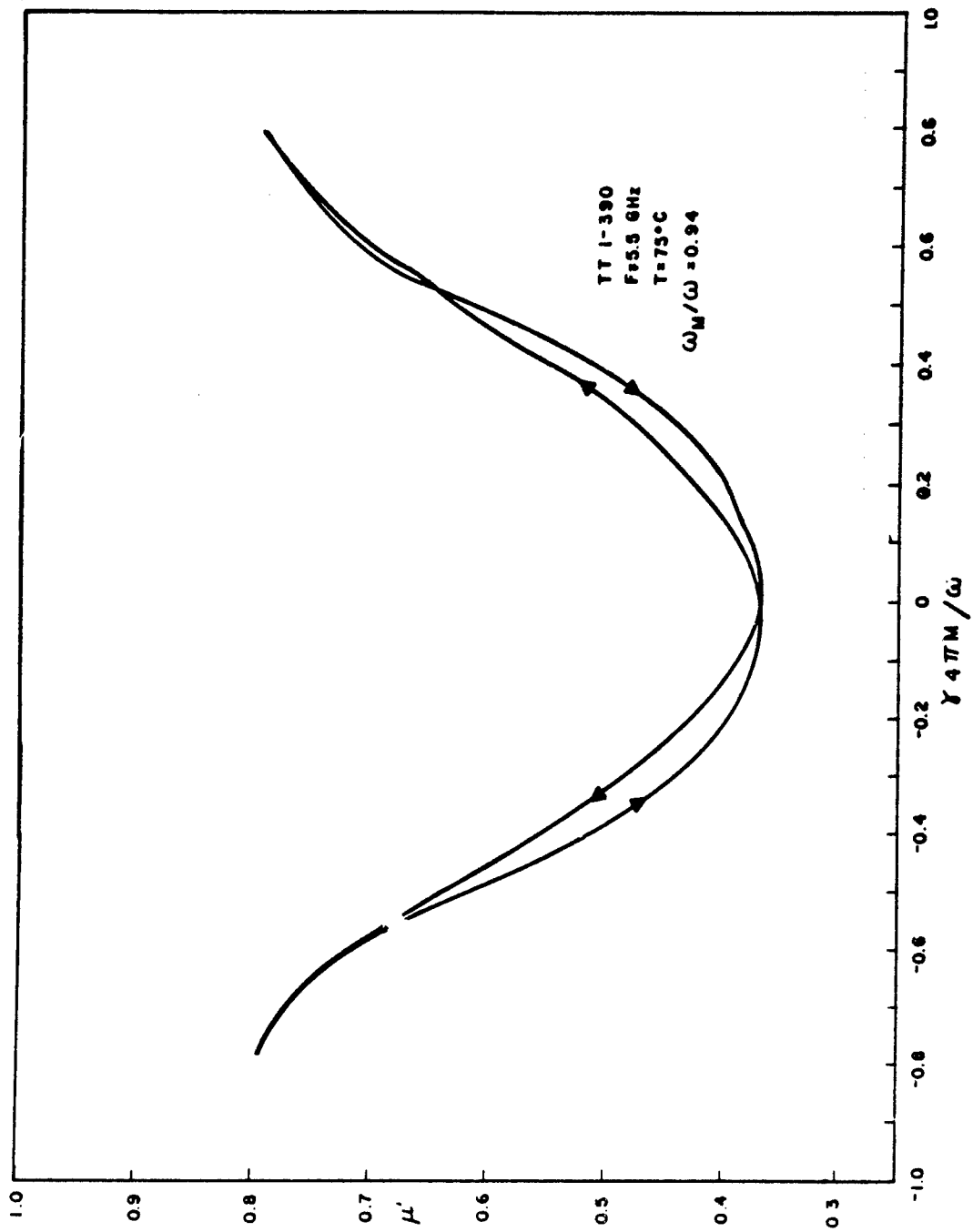


Fig. 6 μ' vs $\gamma_4\pi M/\omega$ on TT1-390 at 5.5 GHz

In Fig. 7 we show both the experimental μ' and that of Eq. (11) as a function of $\gamma 4\pi M/\omega$ for several values of ω_M/ω obtained by heating the sample. Only one branch of each hysteresis curve is shown in this figure for clarity. The other branch is the mirror image of it as can be seen from Fig. 6. In this and all other figures where the full hysteresis curve is not shown, the direction of the branch shown is from positive magnetization to negative magnetizations.

It had been suggested that the reason hysteresis occurred in μ' and κ' vs $\gamma 4\pi M/\omega$ for TT1-390 and not for G-113 was that TT1-390 had a substantial amount of second phase. Measurements have thus also been made on a single-phase magnesium manganese spinel, MMF-10, manufactured by Airtron. The results for μ' are shown in Fig. 8 and are not qualitatively different from TT1-390.

As a confirmation that our results for varying ω_M/ω by heating the sample at constant frequency are valid and also as a confirmation that frequency is not an independent variable in addition to $\gamma 4\pi M/\omega$ and $\gamma 4\pi M_s/\omega$, we show in Fig. 9 μ' vs $\gamma 4\pi M/\omega$ at 9.2 GHz for G-113, R151 (a Raytheon ferrite very similar to TT1-390) and MZMF, a Raytheon magnesium, zinc, manganese ferrite with a $4\pi M_s = 3000$ gauss at room temperature. The shapes of these curves, including their deviations from the solid curves showing Eq. (11), are similar to the comparable curves at 5.5 GHz. The only significant difference occurred for the MZMF; in this material μ' is noticeably larger than the functional form which fits the other materials quite well. In addition its hysteresis in μ' vs $\gamma 4\pi M/\omega$ has the opposite sign to that of TT1-390 and MMF-10.

C. Measurements of μ'_z

Measurements of μ'_z were made on samples placed in the center of a rectangular TE_{102} reflection cavity. Originally we used rod-shaped samples with the rf and dc magnetic fields parallel to each other and perpendicular to the rod. This technique proved unsatisfactory since a rod

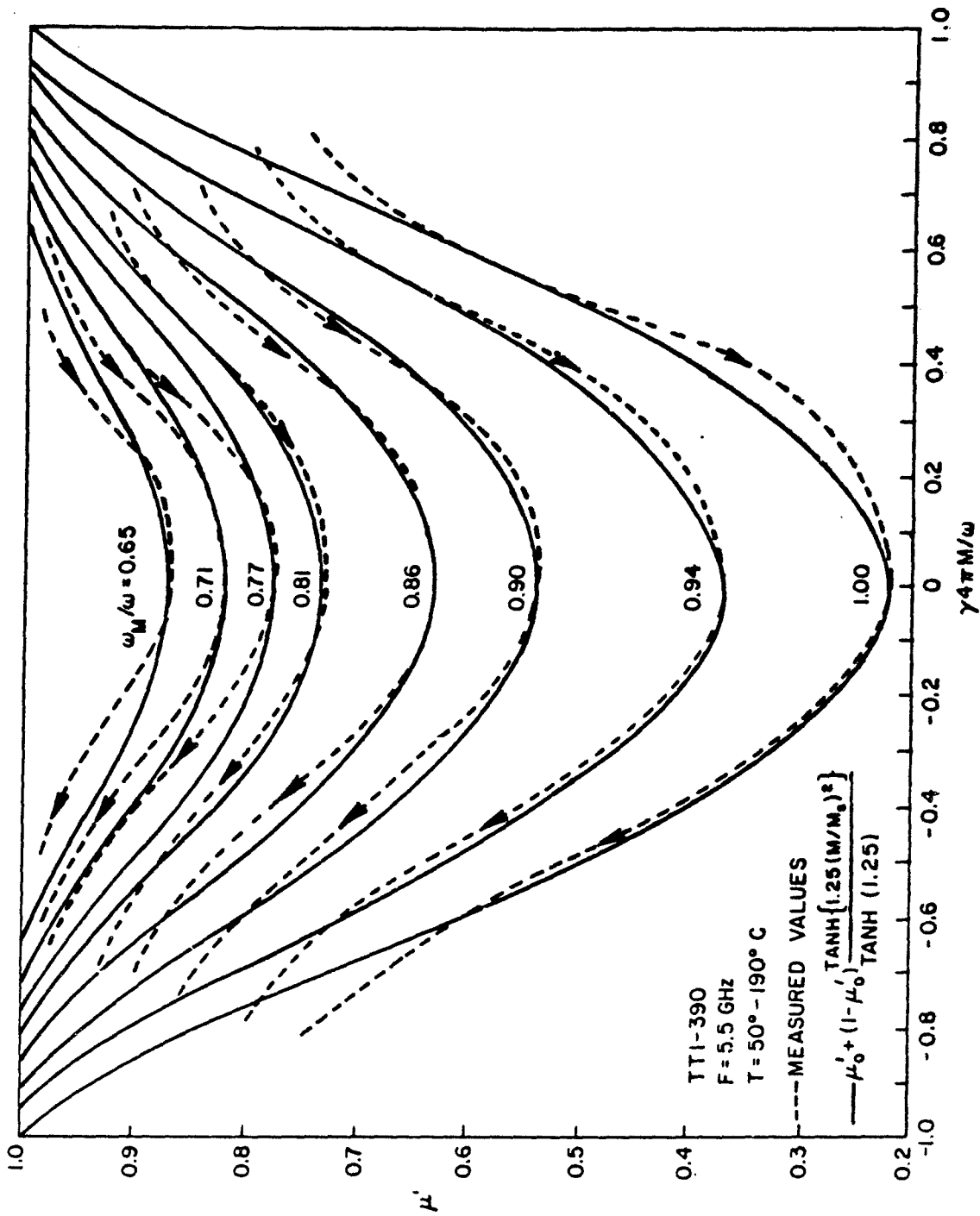


Fig. 7 μ' vs $\gamma 4\pi M/\omega$ on TTI-390 at 5.5 GHz

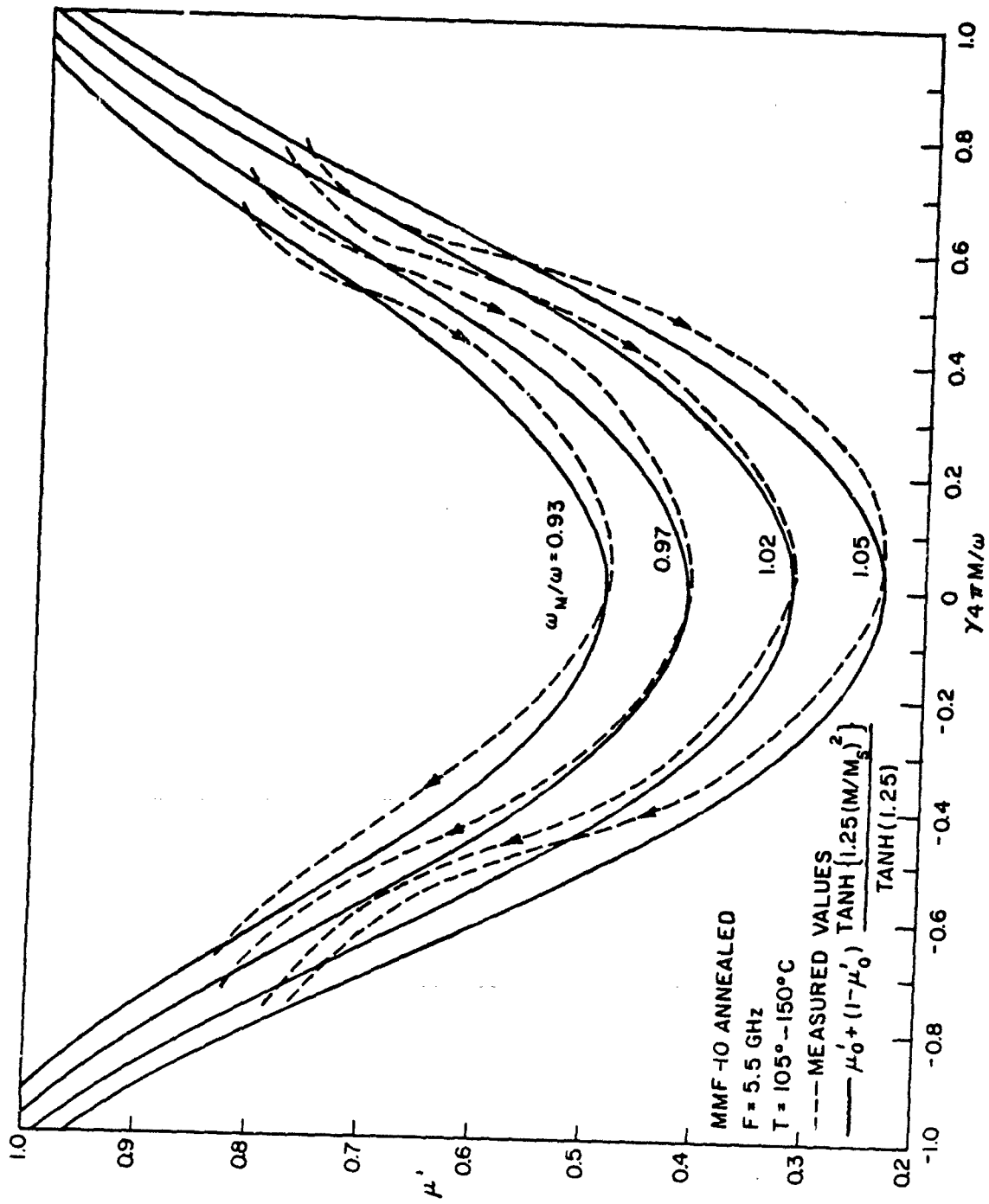


Fig. 8 μ' vs $\gamma 4\pi M/\omega$ on MMF-10 at 5.5 GHz

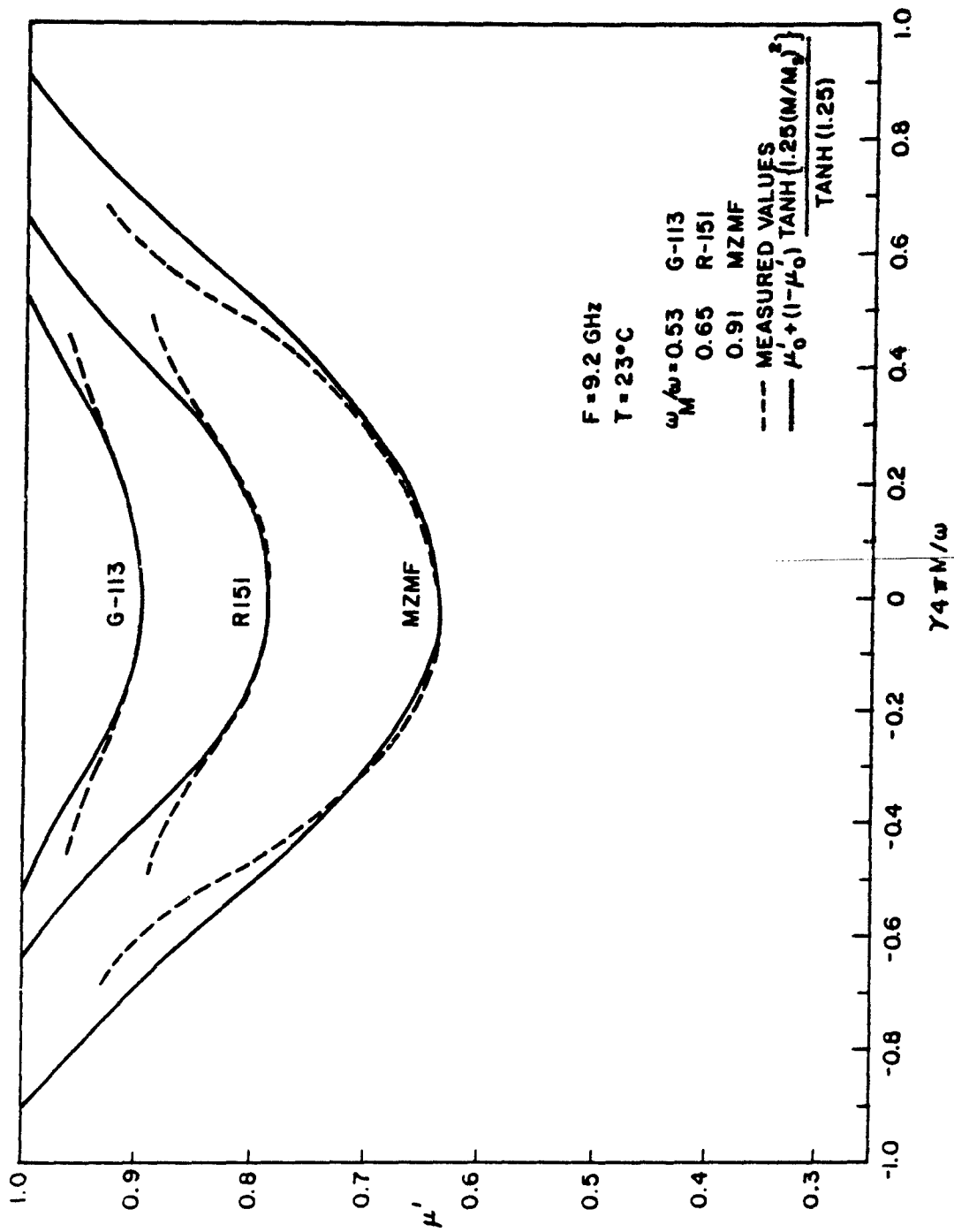


Fig. 9 μ'' vs $\gamma 4\pi M/\omega$ at 9.2 GHz

tends to magnetize along its axis if there is the slightest misalignment of the dc field. The measurements reported here were made on spherical samples. Although this greatly reduced the cavity-filling factor, and hence the sensitivity, it eliminated the serious errors due to misalignment.

Since moderate internal dc fields parallel to the rf field do not cause the sample to approach ferromagnetic resonance, it was possible to measure μ_z at magnetization substantially closer to $4\pi M_s$ than we could when measuring μ and κ .

Measurements were made point by point, varying the dc magnetic field from values large enough to saturate the sample in one direction through zero to values large enough to saturate it in the negative direction. For magnetizations below remanence $4\pi M = 3 H_{dc}$. For high magnetizations, where the internal magnetic field is significant, values of $4\pi M$ vs H_{dc} obtained from a separate measurement of magnetization were used. Apparent values of μ_z' and μ_z'' were obtained from the shift in cavity resonant frequency and reflection coefficient, using the value obtained with a 9.5 kOe field as a reference. Internal values of μ_z were then obtained from the apparent μ_z using the formula

$$\mu_z = \frac{\mu_z \text{ apparent}}{1 - \frac{1}{3} \mu_z \text{ apparent}} \quad (13a)$$

The results for MMF-10 and YIG with 1 percent Dy are shown in Figs. 10 and 11. The solid curves are the function

$$\mu_z' = \mu_z' \circ (1 - (M/M_s)^{5/2}) \quad (13b)$$

Again it should be emphasized that this functional relationship is given because it fits the data reasonably well and hence would be useful in computer-aided design programs for ferrite devices. No real physical basis for this relationship is implied.

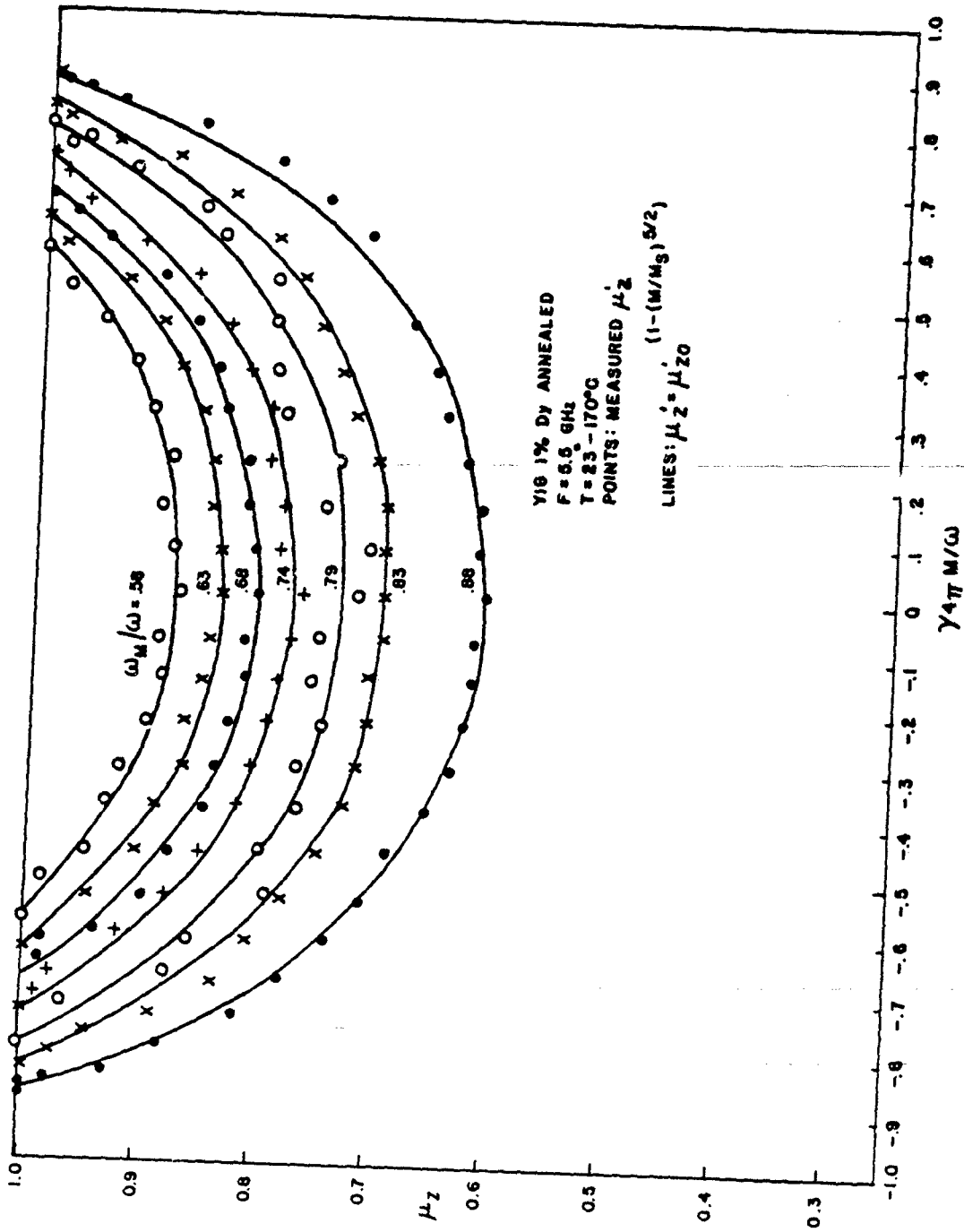


Fig. 10 μ'_2 vs $\gamma 4\pi M/\omega$ on YIG 1 percent Dy at 5.5 GHz

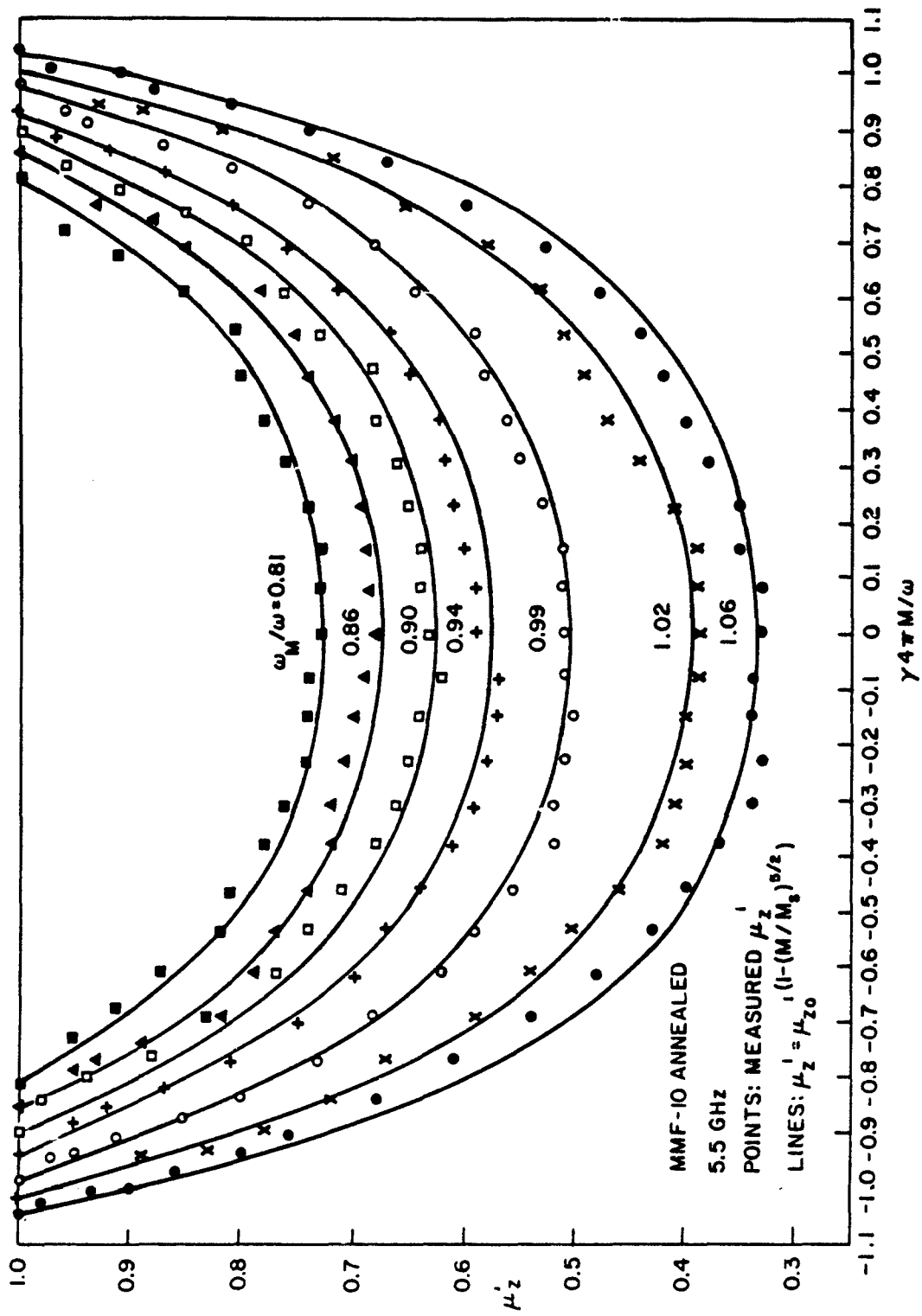


Fig. 11 μ_z^1 vs $\gamma 4\pi M/\omega$ on MMF-10 at 5.5 GHz

In this report we have discussed fitting our data to three different functional forms

$$\begin{aligned}
 F_1 &= \mu'_0 + (1 - \mu'_0) (M/M_s)^{N_1} \\
 F_2 &= \mu'_0 (1 - \mu'_0) \frac{\tanh \{ A (M/M_s)^{N_2} \}}{\tanh (A)} \\
 F_3 &= \mu'_0 (1 - (M/M_s)^{N_3})
 \end{aligned} \tag{14}$$

Each of these functions is identically μ'_0 at $4\pi M = 0$ and 1.0 at $4\pi M = 4\pi M_s$. It is worthwhile to mention how the functions F_2 and F_3 differ in shape for $0 < 4\pi M < 4\pi M_s$ from the more simple function F_1 . Basically F_2 and F_3 with constant N_2 and N_3 are the same as F_1 with a variable N_1 . F_2 is the same as F_1 with $N_1 = N_2$ at $4\pi M = 0$ and an N_1 that decreases as $4\pi M$ approaches $4\pi M_s$. F_3 on the other hand is the same as F_1 with the $N_1 = N_3$ when $4\pi M = 4\pi M_s$ and an N_1 that decreases as $4\pi M$ approaches zero. As each N is increased, all three functions become flatter at $4\pi M = 0$ and increase more sharply as $4\pi M$ approaches $4\pi M_s$. It is found, however, in fitting our data to F_1 that if we choose N_1 so that the function fits our data for small $4\pi M$, then the function is too large for μ'_0 and too small for μ'_2 at large $4\pi M$. Thus we use the functional for F_2 for μ'_0 and F_3 for μ'_2 .

The question of whether there is hysteresis in μ'_2 , i. e., whether μ'_2 is a unique function of magnetization or depends on which side of the B-H hysteresis loop the sample is on, is not as clear cut as it was for μ' and κ' because our measurement technique is less sensitive than that for μ' and κ' . In addition, being a point-by-point measurement rather than a continuous measurement, it is subject to small drift errors. No hysteresis was detectable in μ'_2 for the YIG. A small amount of hysteresis is apparent is

apparent for MMF-10 at low values of $4\pi M$ and values of $\omega_M/\omega > 0.9$. This values of ω_M/ω is greater than the maximum value for YIG however. The hysteresis in μ'_z above this value shows up as smaller values of μ'_z at negative magnetizations than at the corresponding positive magnetization.

D. Measurements of μ'' and κ''

The imaginary parts of μ and κ were measured with the same cavity as the real parts. However, since it is not possible to obtain a continuous plot of Q vs magnetization as the rod is cycled about the B-H hysteresis loop, point-by-point measurements must be made. The cavity Q and frequency were recorded as a function of dc magnetic field since magnetization could not be measured directly point by point. A separate plot of $4\pi M$ vs H was then made. Using these results, one could calculate $\mu'_+ = \mu'' - \kappa''$ as well as $\mu'_+ = \mu' - \kappa'$ as a function of either field or magnetization using perturbation theory. This was done only for our preliminary measurements on G-113 used to test the system. For subsequent measurements the exact solutions for a rod in a cavity were used. This solution required a knowledge of cavity Q and resonant frequency for both senses of circular polarization at each magnetization. This did not mean that measurements had to be made with both senses of circular polarization since the values for one sense are the same as those of the opposite sense when the rod is oppositely magnetized both in magnitude and hysteresis history. Since measurements were made at points with uniformly spaced magnetic fields, data was not directly available at points with equal and opposite magnetization. Therefore, we drew smooth curves through the raw data and used the interpolated values from the smoothed curves rather than the raw data to do the subsequent calculations. The data reduction using the exact solution yields μ' , μ'' , κ' , κ'' directly rather than μ'_+ and μ'_- which are obtained from perturbation theory.

One of the most striking effects which we observed in our early loss measurements was a large surface loss caused by strains induced by grinding the sample to shape. Although we were aware of the existence of surface loss, our first preliminary loss measurements were made on

a rod of G-113 which had not yet been annealed to remove the surface strain and loss. We had expected the effect would be to increase $\mu'_+ = \mu'' - \kappa''$ by a constant scale factor related to ratio of surface loss to bulk loss and the fractional volume of the strained surface layer. We were therefore surprised to find the results for μ'_+ vs H_{dc} shown in Fig. 12. In this figure we also show the magnetic hysteresis loop B vs H. It can be seen that μ'_+ vs H does not close until much larger magnetic fields than those necessary to close the B vs H hysteresis loop. This phenomenon results from the fact that the strained surface layer, whose loss is actually the dominant loss observed in spite of its small volume, also has a very high coercive force. The observed μ'_+ thus has the very different hysteresis properties of the surface layer rather than the average measured hysteresis properties which correspond primarily to the bulk material. The results obtained after this sample was annealed are shown in Fig. 13. The magnitude of μ'_+ is greatly reduced, the two peaks occur at the coercive fields, and the loops close at the same field as the B-H loop shown in Fig. 12 closed.

The scatter shown at negative fields is due to the rf demagnetizing fields on the sample surface. These demagnetizing fields necessitate a correction of the following form to convert the apparent circular susceptibility ($\mu_{+app} - 1$) which is proportional to the change in complex frequency ($f + if/2Q$) of the cavity to true susceptibility ($\mu_+ - 1$)

$$\mu_+ - 1 = \frac{2(\mu_{+app} - 1)}{2 - (\mu_{+app} - 1)} \quad (15)$$

Writing μ_+ and μ_{+app} in complex form, separating real and imaginary parts and noting that $\mu'_{+app} \ll \mu'_{+app} - 1$ gives

$$\mu'_+ - 1 = \frac{2(\mu'_{+app} - 1)}{2 - (\mu'_{+app} - 1)} \quad (16)$$

$$\begin{aligned} \mu''_+ &= \frac{4\mu''_{+app}}{(2 - (\mu'_{+app} - 1))^2} \\ &= \frac{\mu''_{+app} (1 + \mu'_+)^2}{4} \end{aligned} \quad (16)$$

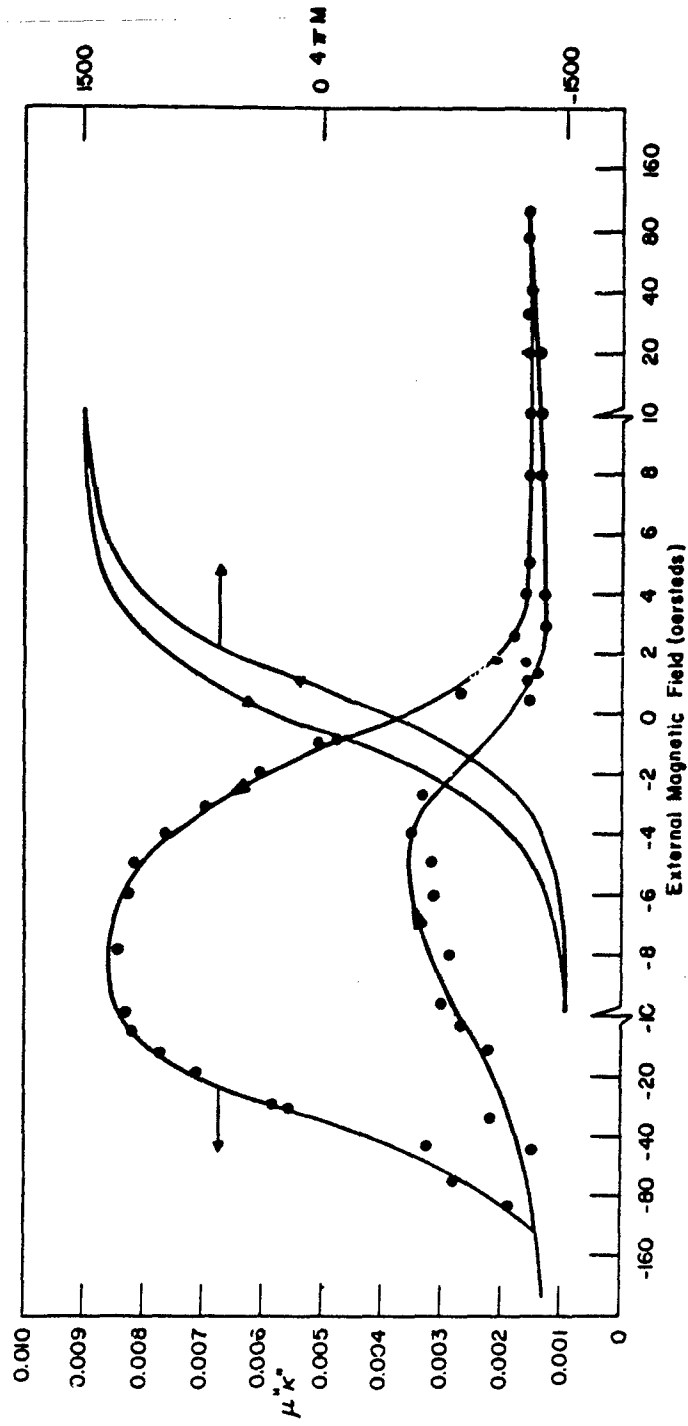


Fig. 12 $\mu''-\kappa''$ and $4\pi M$ vs External Magnetic Field for Unannealed G-113 at 5.5 GHz

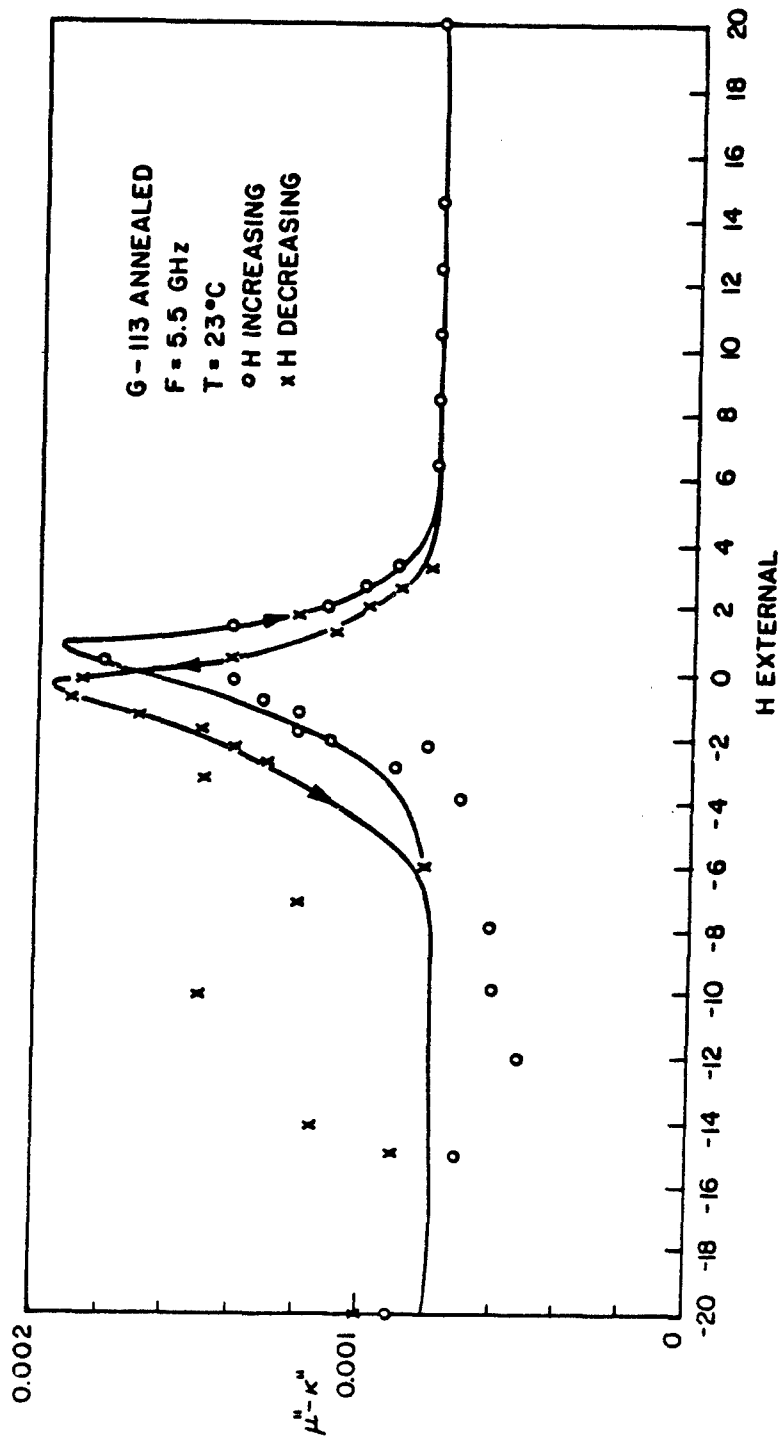


Fig. 13 $\mu''-\kappa''$ and $4\pi M$ vs External Magnetic Field for Annealed G-113 at 5.5 GHz

Since the system sensitivity is inversely proportional to the minimal detectable change in $1/Q$ and this is proportional to μ''_{app} , the scatter in μ'' is proportional to $(1+\mu'_+)^2$. Since $1+\mu'_+$ varies almost from 1.0 to 3.0, the change in sensitivity is almost an order of magnitude as the direction of magnetization changes. Although the sensitivity was improved for subsequent measurements, it was felt that differences between μ'' and κ'' and their dependence on $\gamma 4\pi M/\omega$ could be more accurately observed in an intrinsically lossier material. We therefore used a YIG doped with 1 percent Dy rather than G-113 in subsequent.

The results of μ'' and κ'' for the YIG with 1 percent Dy are shown in Figs. 14 and 15. This and all other materials referred to in the rest of this and the two following sections have been annealed. The variation in ω_M/ω was obtained by heating the sample. Although this also changes the relaxation rate, the shapes of μ'' and κ'' with ω_M/ω at all values of $\gamma 4\pi M/\omega$ is primarily due to the drop in ω_M/ω , but does depend to a noticeable degree on the change in the relaxation rate as ω_M/ω becomes substantially less than 1.0. It is interesting to note that as ω_M/ω decreases, the peak in κ'' at $4\pi M = 0$ disappears and then becomes a minimum. It is believed that this is caused by the following. The observed losses are due to the high-frequency tails of ferromagnetic resonance curves. Near remanence these curves are centered about a resonant frequency of zero since the net internal dc magnetic field including anisotropy and demagnetizing fields is close to zero. In the demagnetized state, Polder and Smit⁴ have shown that these resonances occur at all frequencies from zero to ω_M . When ω is close to ω_M , the resonances close to ω_M predominate and make μ'' larger in the demagnetized state than near remanence. When $\omega \gg \omega_M$, all of the resonance tails contribute equally and there is no tendency for μ'' to peak at $4\pi M = 0$. However, in the demagnetized state, one third of the domains are parallel to the rf drive field and do not contribute to the ferromagnetic resonance tail. Thus μ'' can have a minimum at $4\pi M = 0$ for sufficiently low values of ω_M/ω . This of course assumes that $\mu''_z \ll \mu''$ for $4\pi M = 4\pi M_s$ and an internal field equal zero. There is however a very small but finite μ''_z due to subthreshold parallel pumping. This is discussed in the next section.

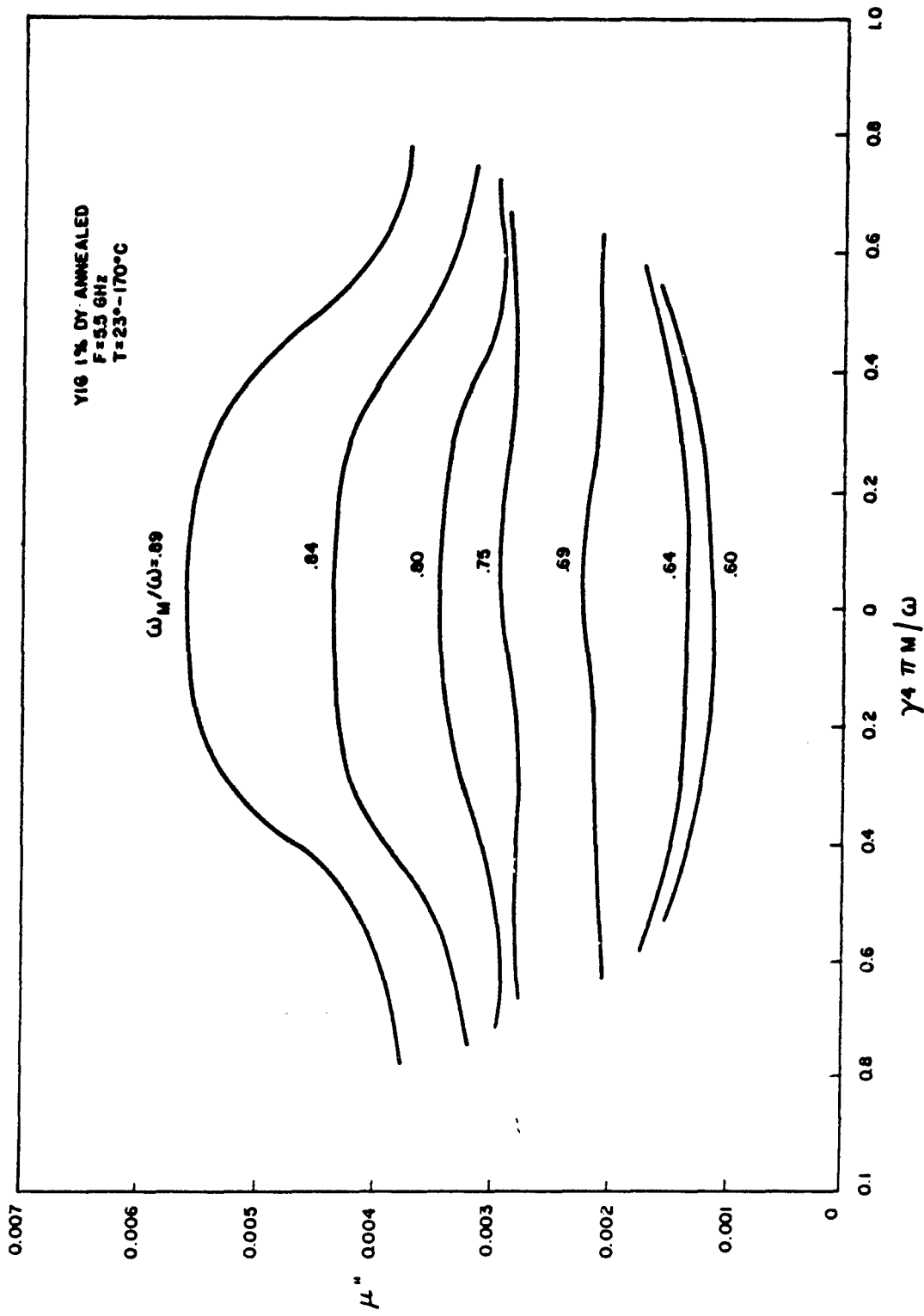


Fig. 14 μ'' vs $\gamma 4 \pi M / \omega$ for YIG 1 percent Dy at 5.5 GHz

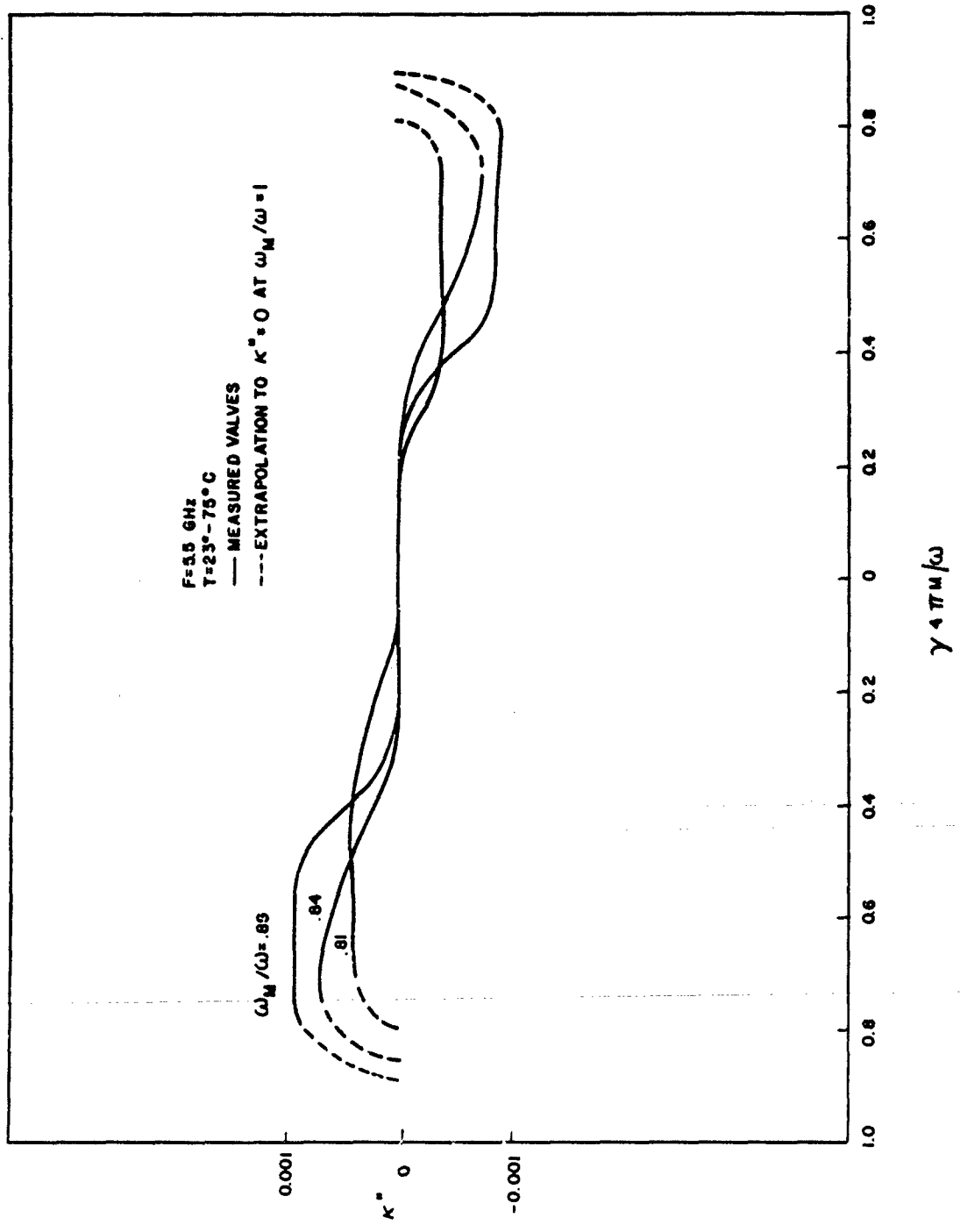


Fig. 15 κ'' vs $\gamma 4 \pi u / \omega$ for YIG 1 percent Dy at 5.5 GHz

It should also be noticed in Figs. 14 and 15 that for all values of ω_M/ω obtainable with YIG, $\kappa'' \ll \mu''$. Since κ is an odd function of $4\pi M$, $\kappa'' = 0$ when $4\pi M = 0$. It is also zero theoretically in the fully saturated state if $H_{dc} = 0$. However, a drop of κ'' toward zero as the material approached maximum magnetization was not observed for this material.

The results of μ'' and κ'' vs $\gamma 4\pi M/\omega$ for various values of ω_M/ω are shown for TT1-390 and MMF-10 in Figs. 16 through 20. These include higher values of ω_M/ω than could be obtained for YIG at 5.5 GHz and at room temperature and above. However, since they are intrinsically low-loss materials, it was not possible to go to as low values of ω_M/ω as with the Dy-doped YIG. In Fig. 16 the full hysteresis loop is shown for μ'' and κ'' . In the remaining figures only one branch is shown, the other branch being its mirror image. At large values of ω_M/ω , μ'' is found to have a double peak. This results from a phenomenon first observed by Le Crow and Spencer¹⁰ in which $\mu''_{\pm} = \mu'' - \kappa''$ peaks at negative magnetizations rather than at zero. They referred to this as "anomalous ferrimagnetic resonance" and gave a qualitative explanation of it.

For both TT1-390 and MMF-10, we found that $|\kappa''|$ peaked at some value of $4\pi M$ between zero and saturation as expected theoretically. As ω_M/ω dropped below 1.0, κ'' becomes much less than μ'' .

Both these materials also showed substantial hysteresis in μ'' and κ'' vs $4\pi M$. The character of their hysteresis is different, however. For magnetization decreasing from positive to negative, the maximum μ'' occurs for negative magnetization in TT1-390 and positive magnetization in MMF-10. The maximum of $|\kappa''|$ occurs for positive magnetizations in TT1-390 and negative magnetizations in MMF-10. This is merely a manifestation of the fact that their domain structures behave differently as the magnetic hysteresis loop is traversed.

In Figs. 21 through 25, μ'' is plotted as a function of ω_M/ω for $4\pi M = 0$ and $4\pi M = 2/3(4\pi M_s)$ for each of the three materials measured. The magnetization $2/3(4\pi M_s)$ is assumed to be roughly the remanence value. The values of κ'' vs ω_M/ω at $2/3(4\pi M_s)$ and at their peaks are also plotted.

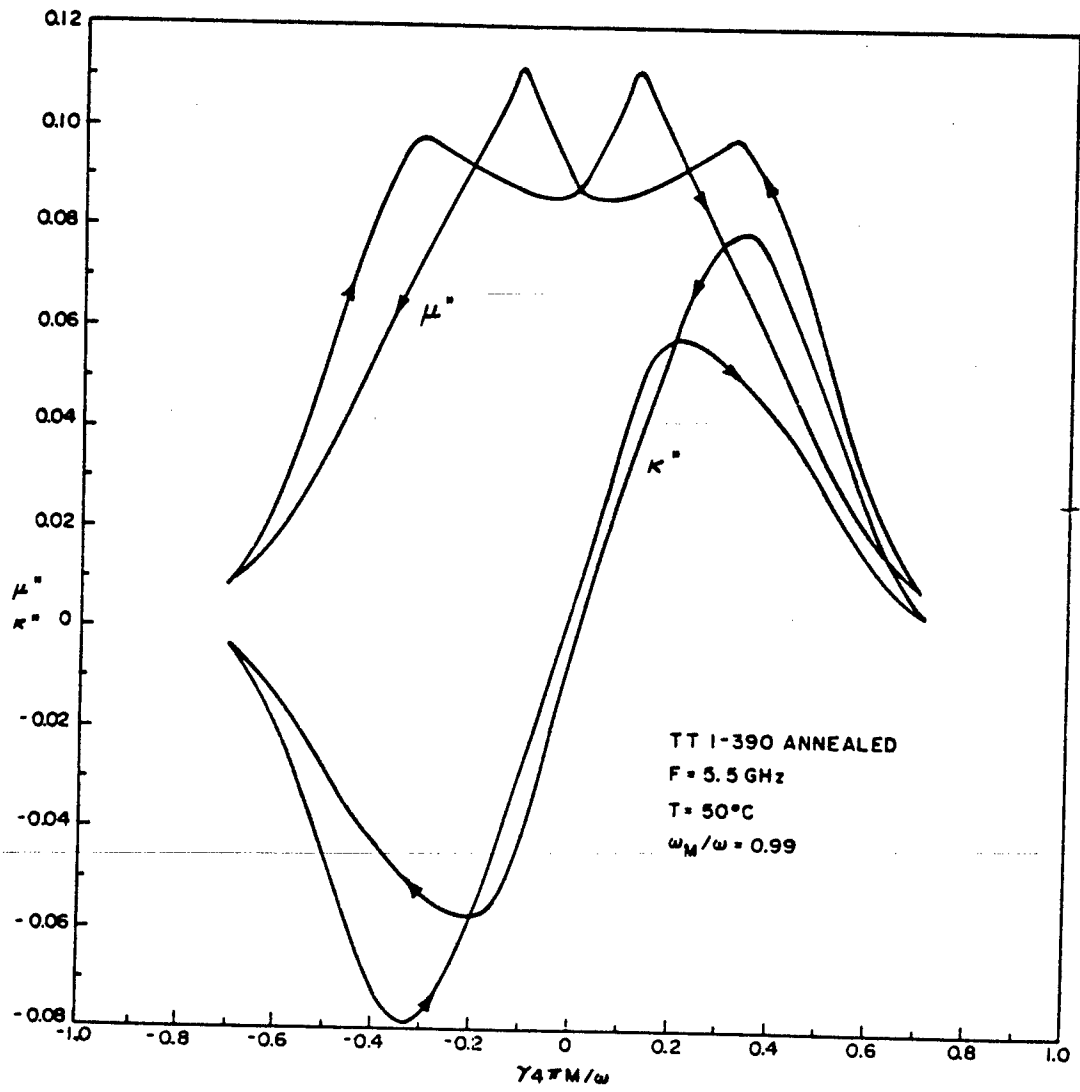
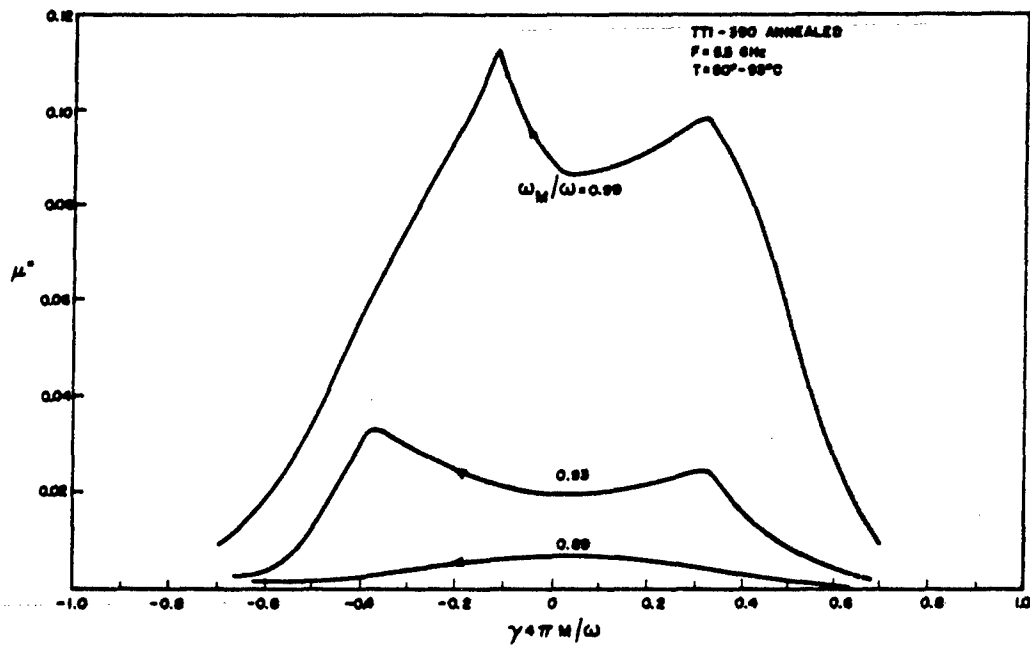
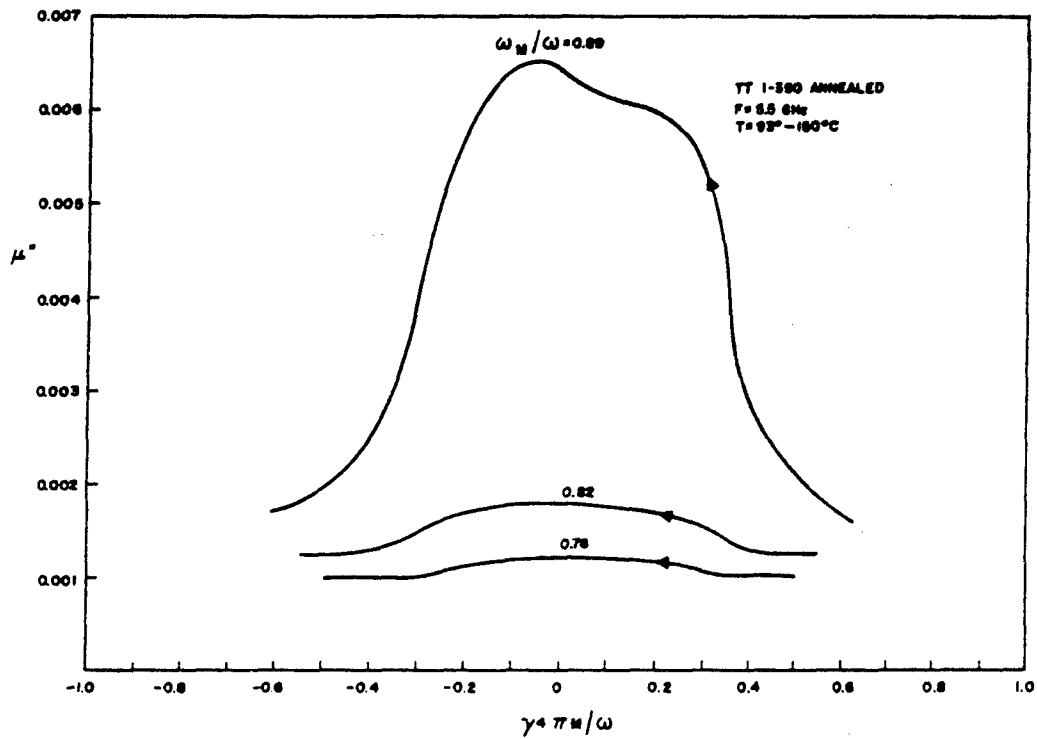


Fig. 16 μ'' and κ'' vs $\gamma 4\pi M/\omega$ for TT1-390 at 5.5 GHz

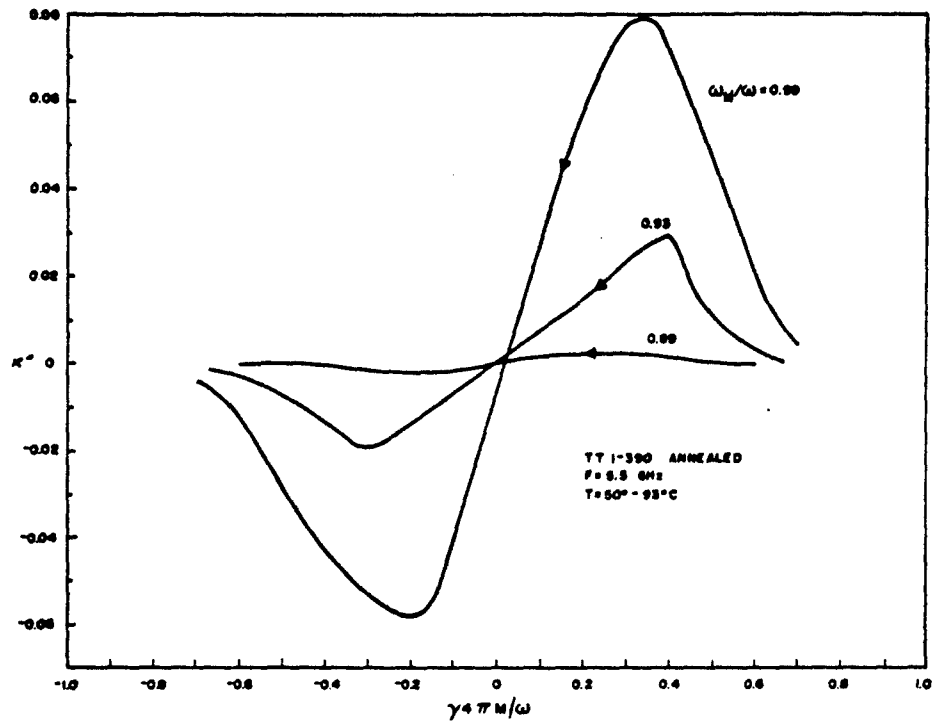


(a)

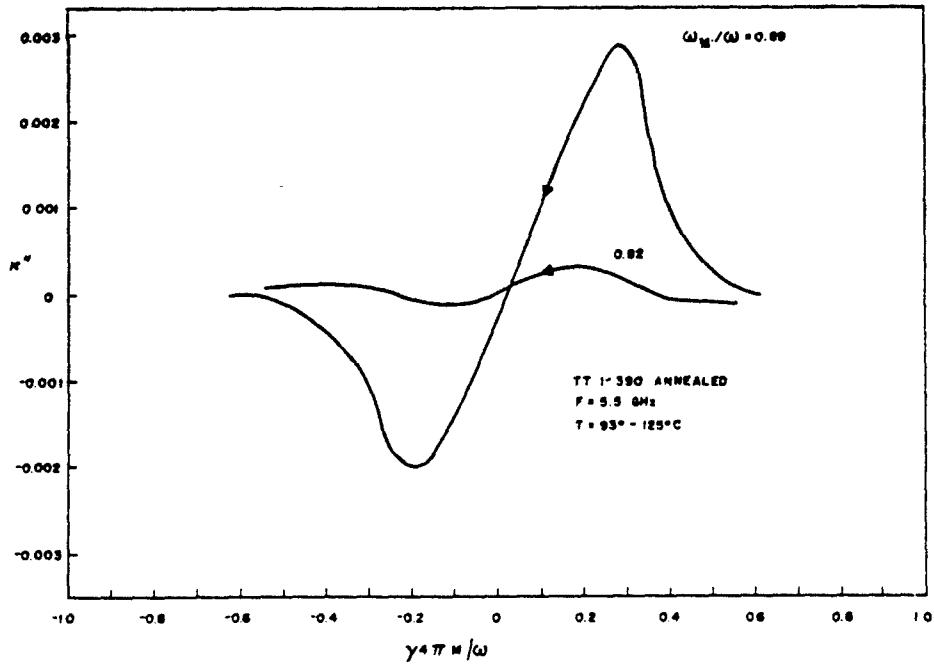


(b)

Fig. 17 μ'' vs $\gamma 4\pi M/\omega$ for TT1-390 at 5.5 GHz



(a)



(b)

Fig. 18 κ'' vs $\gamma 4\pi M/\omega$ for TT1-390 at 5.5 GHz

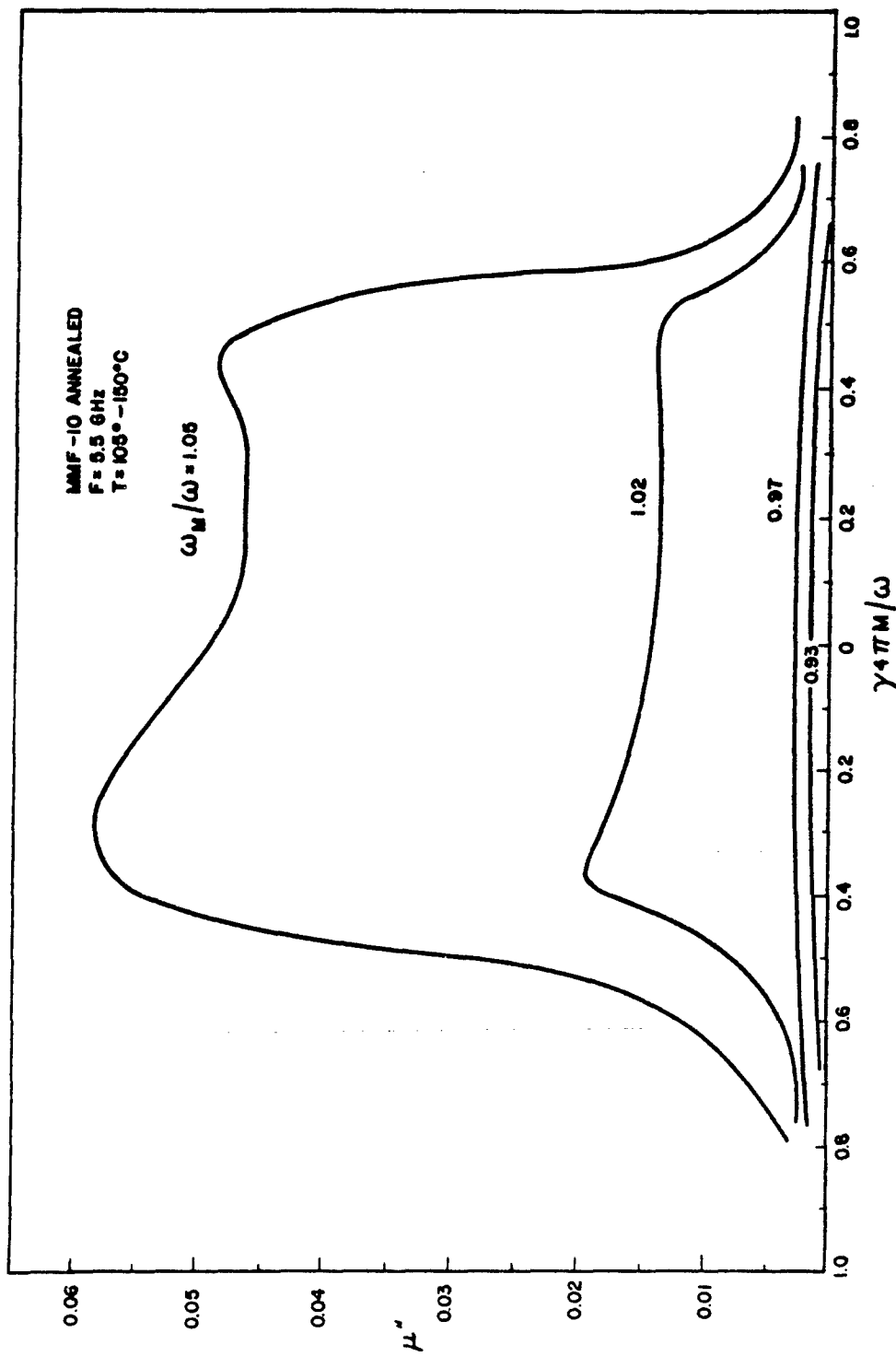


Fig. 19 μ'' vs $\gamma_4\pi M/\omega$ for MMF-10 at 5.5 GHz

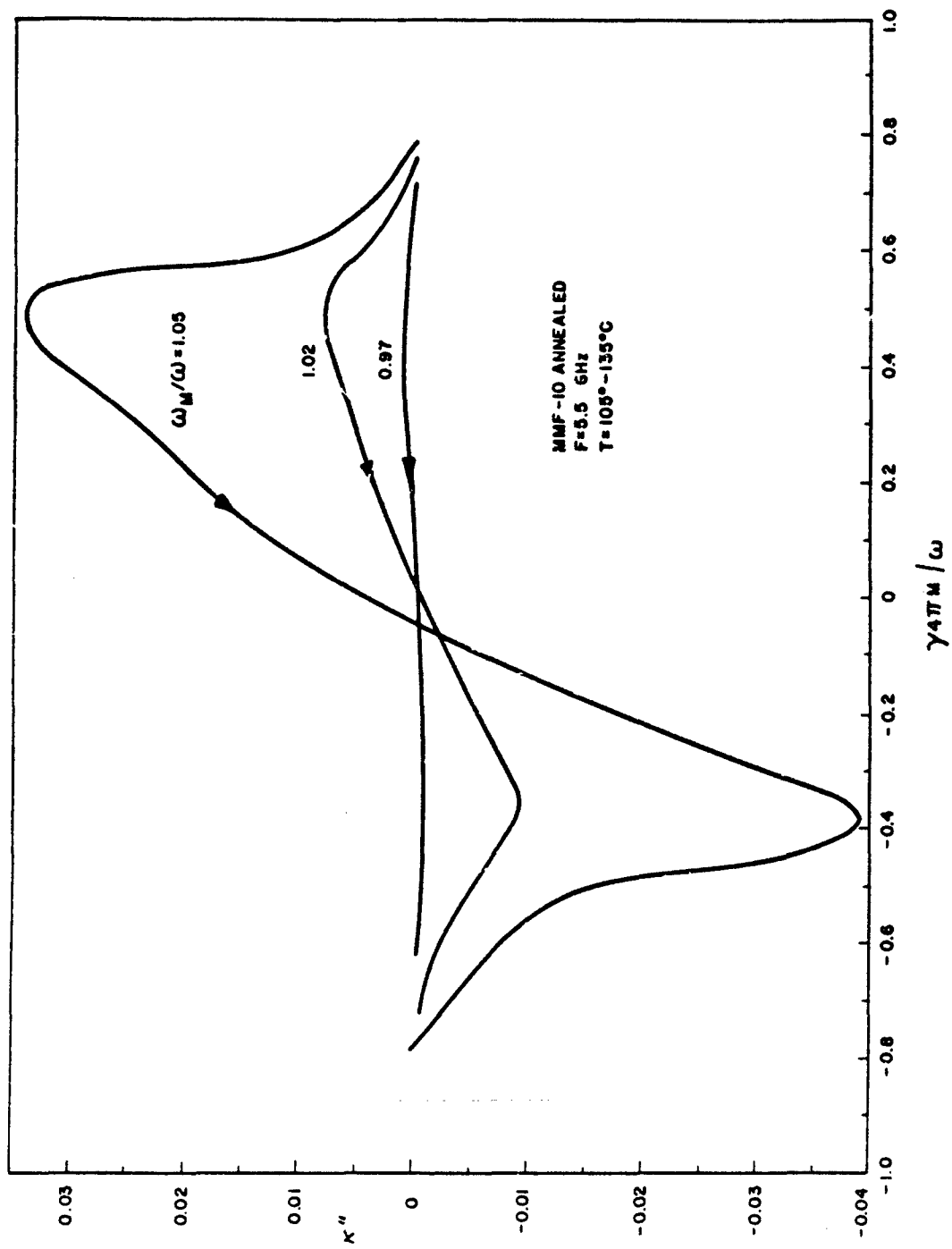


Fig. 20 κ'' vs $\gamma 4\pi M / \omega$ for MMF-10 at 5.5 GHz

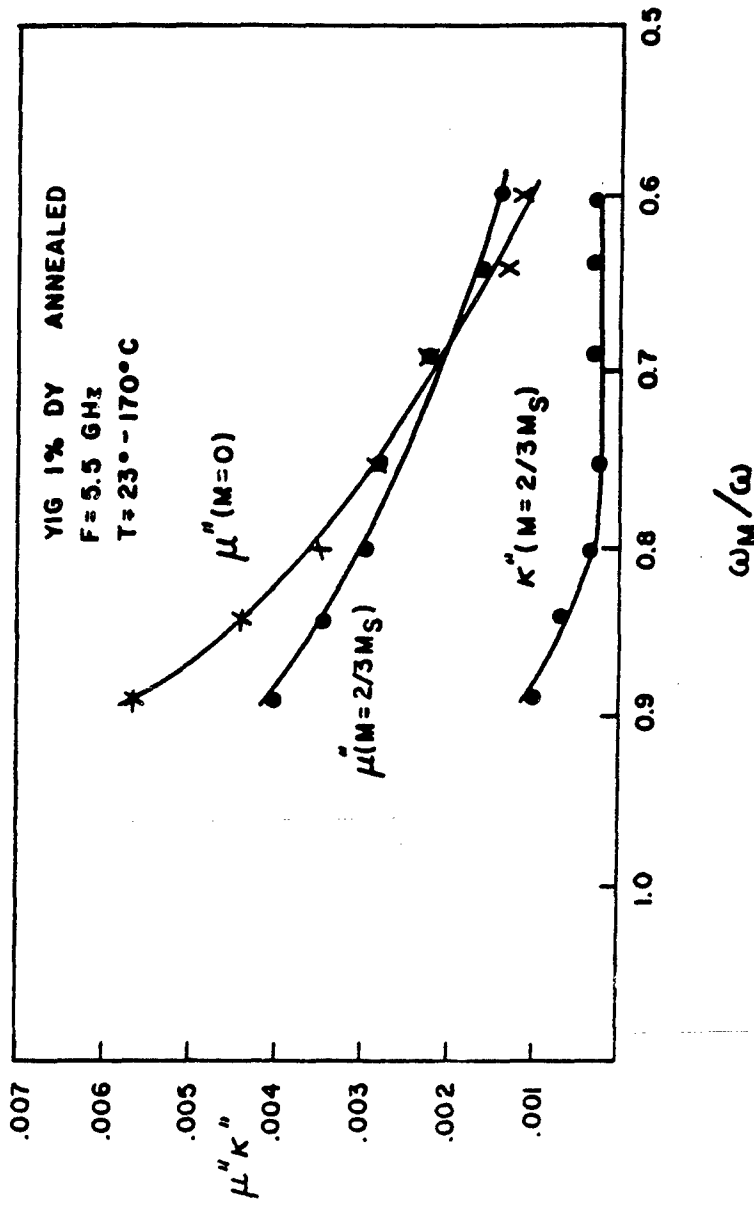


Fig. 21 μ'' and κ'' vs ω_M/ω for YIG 1 percent Dy at 5.5 GHz

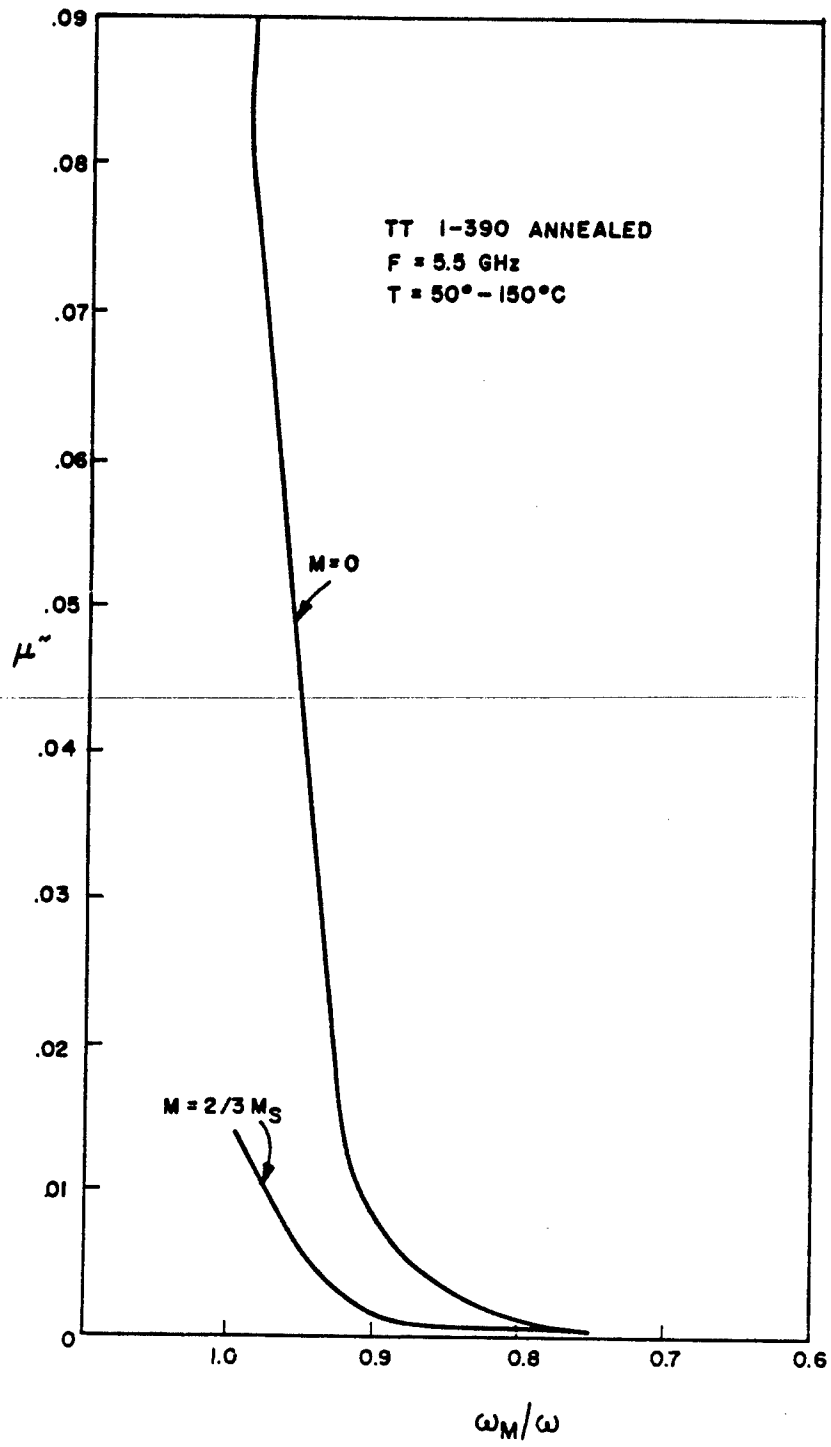


Fig. 22 μ'' vs ω_M/ω for TT1-390 at 5.5 GHz

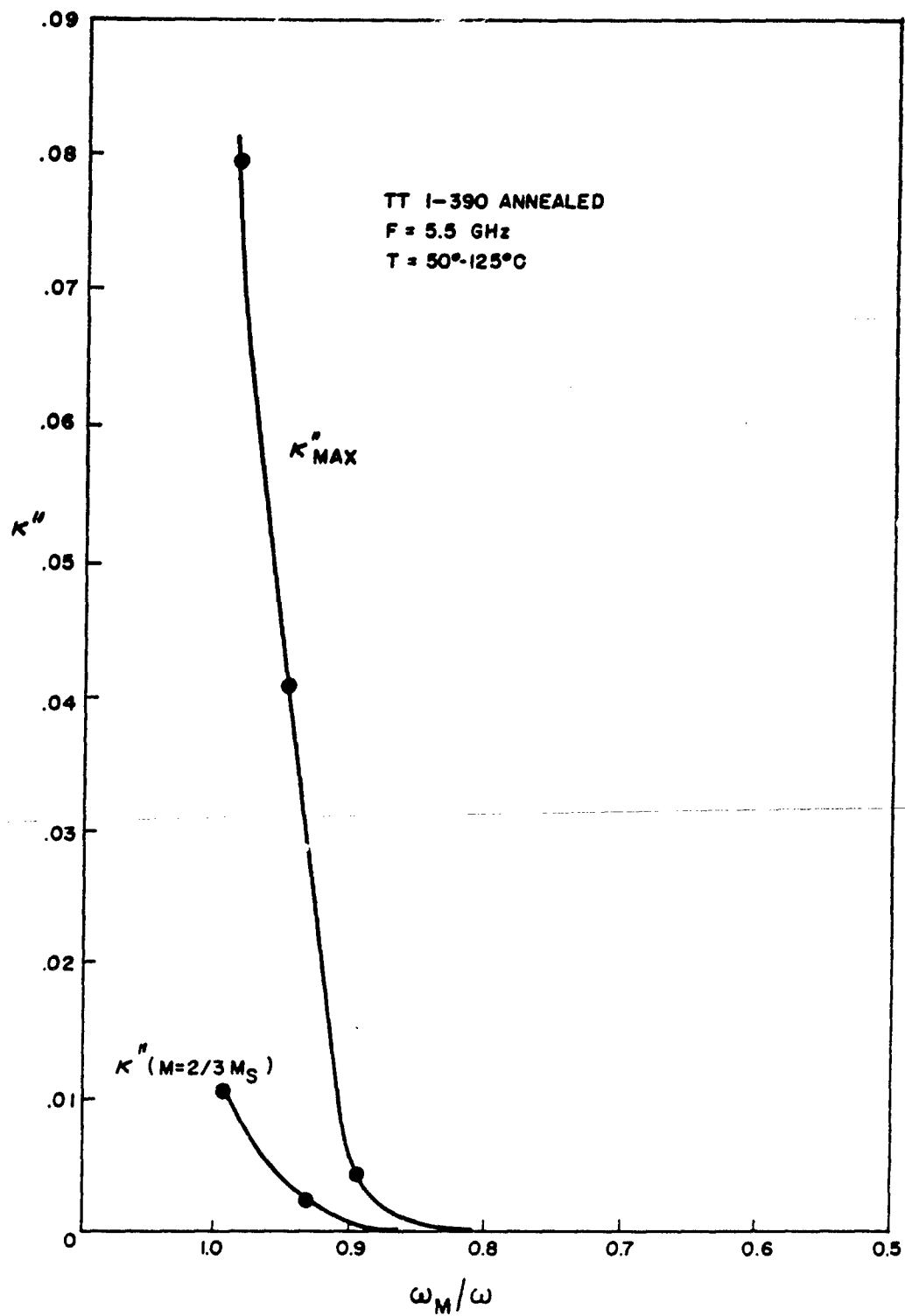


Fig. 23 κ'' vs ω_M/ω for TT1-390 at 5.5 GHz

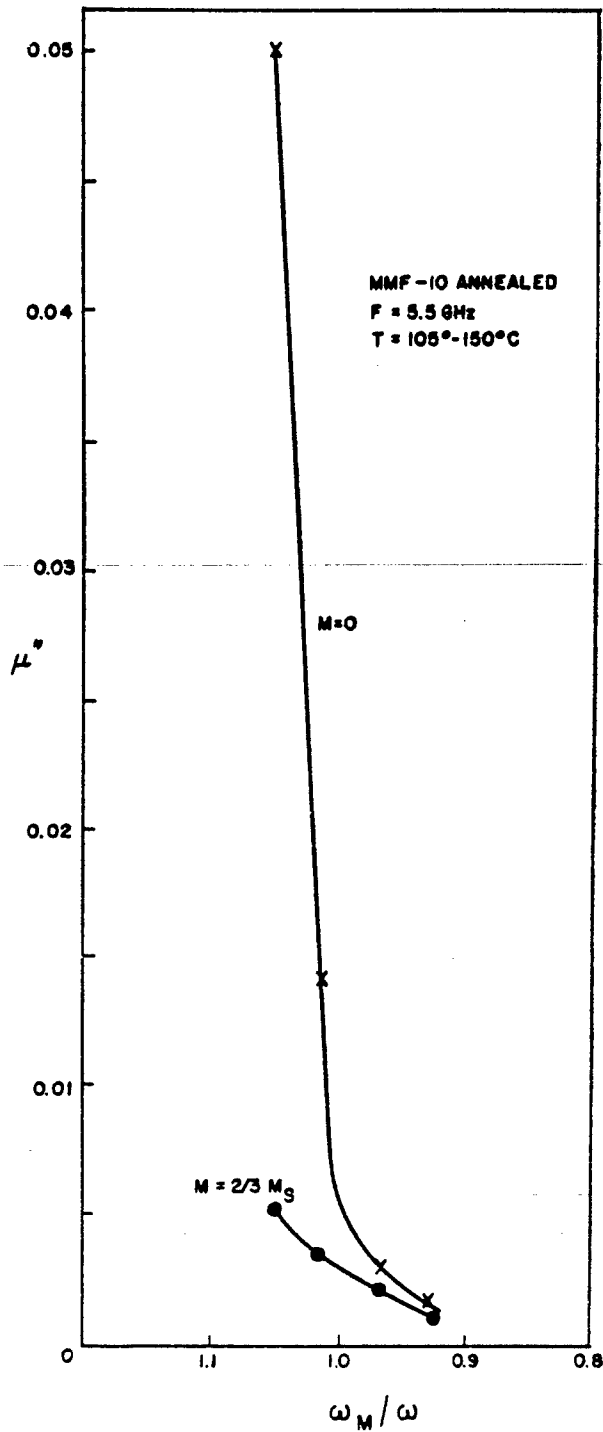


Fig. 24 μ'' vs ω_M/ω for MMF-10 at 5.5 GHz

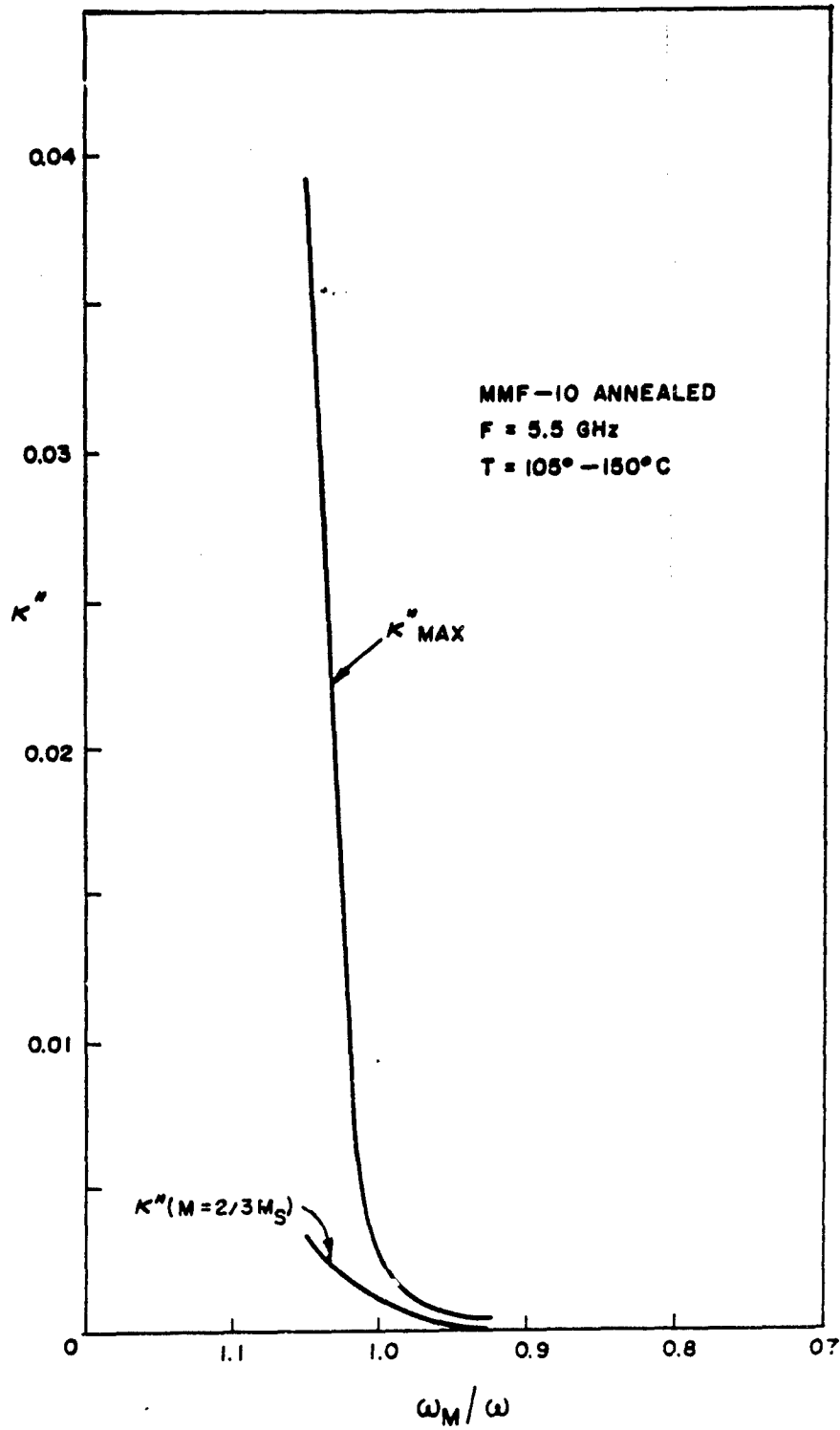


Fig. 25 κ'' vs ω_M/ω for MMF-10 at 5.5 GHz

E. Measurements of μ''_z

Measurements of μ''_z were made on the same system as μ'_z using the change in reflection coefficient of the cavity between 9400 Oe and the measurement field. The results for YIG with 1 percent Dy and MMF-10 are shown in Figs. 26 and 27. The ranges of ω_M/ω for these two materials do not overlap significantly.

For all measured values of ω_M/ω for both materials, μ''_z has a single peak at $4\pi M = 0$. However, the behavior of μ''_z compared to μ'' as $4\pi M$ approaches remanence and higher magnetizations is quite different for the two materials. For the Dy-doped YIG, μ'' levels off near or somewhat below remanence, while μ''_z continues to drop rapidly as saturation is approached. In this region μ''_z is less than μ'' . For MMF-10 both μ'' and μ''_z drop rapidly as magnetization increases but the drop in μ''_z is not as sharp and at high magnetization μ''_z is greater than μ'' . It is not clear if these differences are due to the different ω_M/ω values for the two materials or due to an inherent difference in the materials.

There are two effects which contribute to μ''_z in saturated samples which should be mentioned in any discussion of μ''_z . One of these is Larmor excitation^{11, 12} by inhomogeneities, the other is subthreshold parallel pumping.¹³ The Larmor excitation results because the local magnetization and rf field are not exactly parallel even though the average magnetization and rf field may be parallel. This lack of local parallelism is caused by inhomogeneities such as porosity and crystalline anisotropy. In dense polycrystalline materials the effect is very small and only noticeable for applied dc fields which place the sample in the vicinity of ferromagnetic resonance.

The subthreshold parallel pump absorption results from rf magnetic field pumping of standing spinwaves which are at half the pump frequency. These spinwaves have a net moment along the axis of their precessional cone and can couple to a uniform rf field. The moment is a result of the

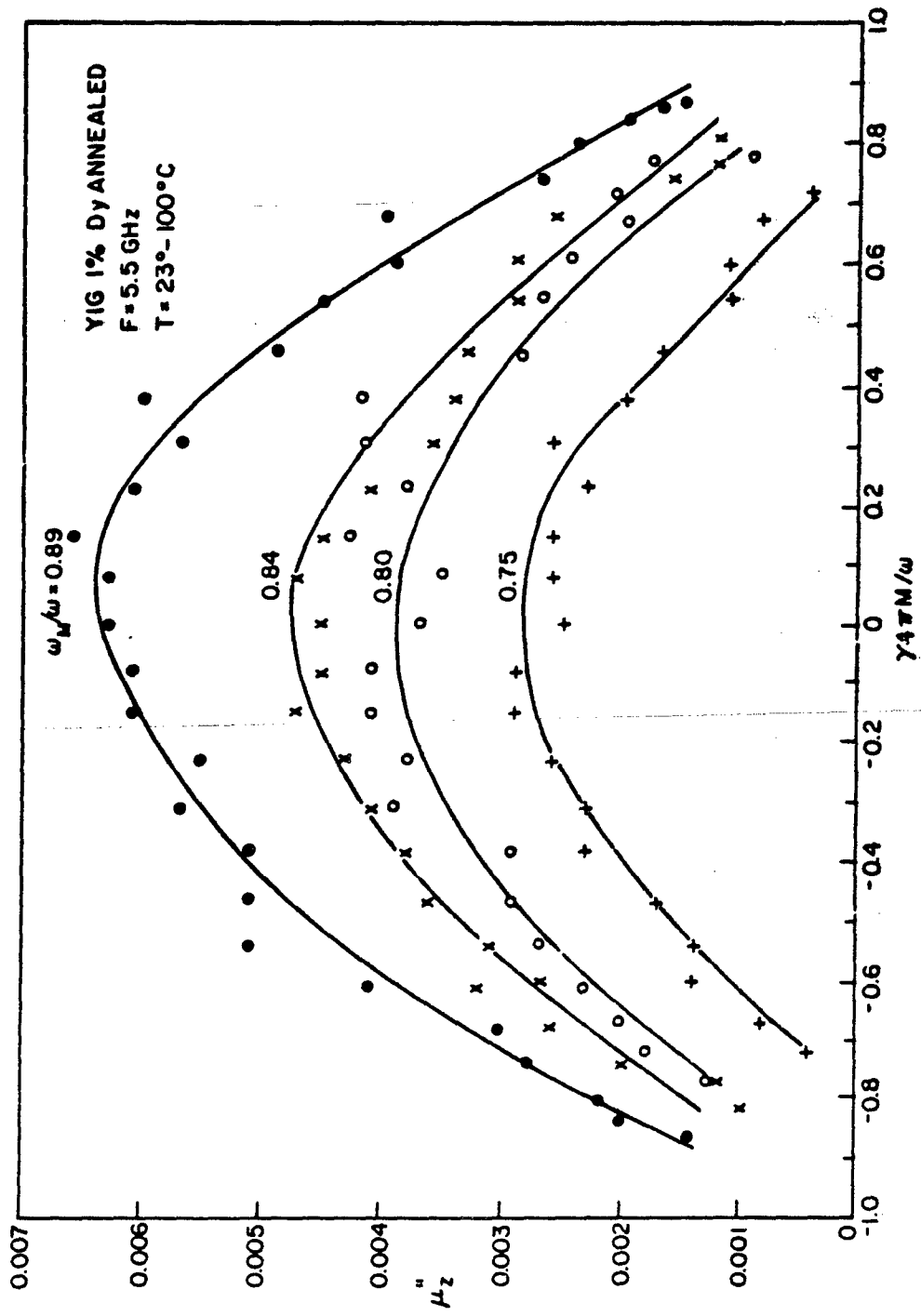


Fig. 26 μ_2'' vs $\gamma 4\pi M/\omega$ for YIG 1 percent Dy at 5.5 GHz

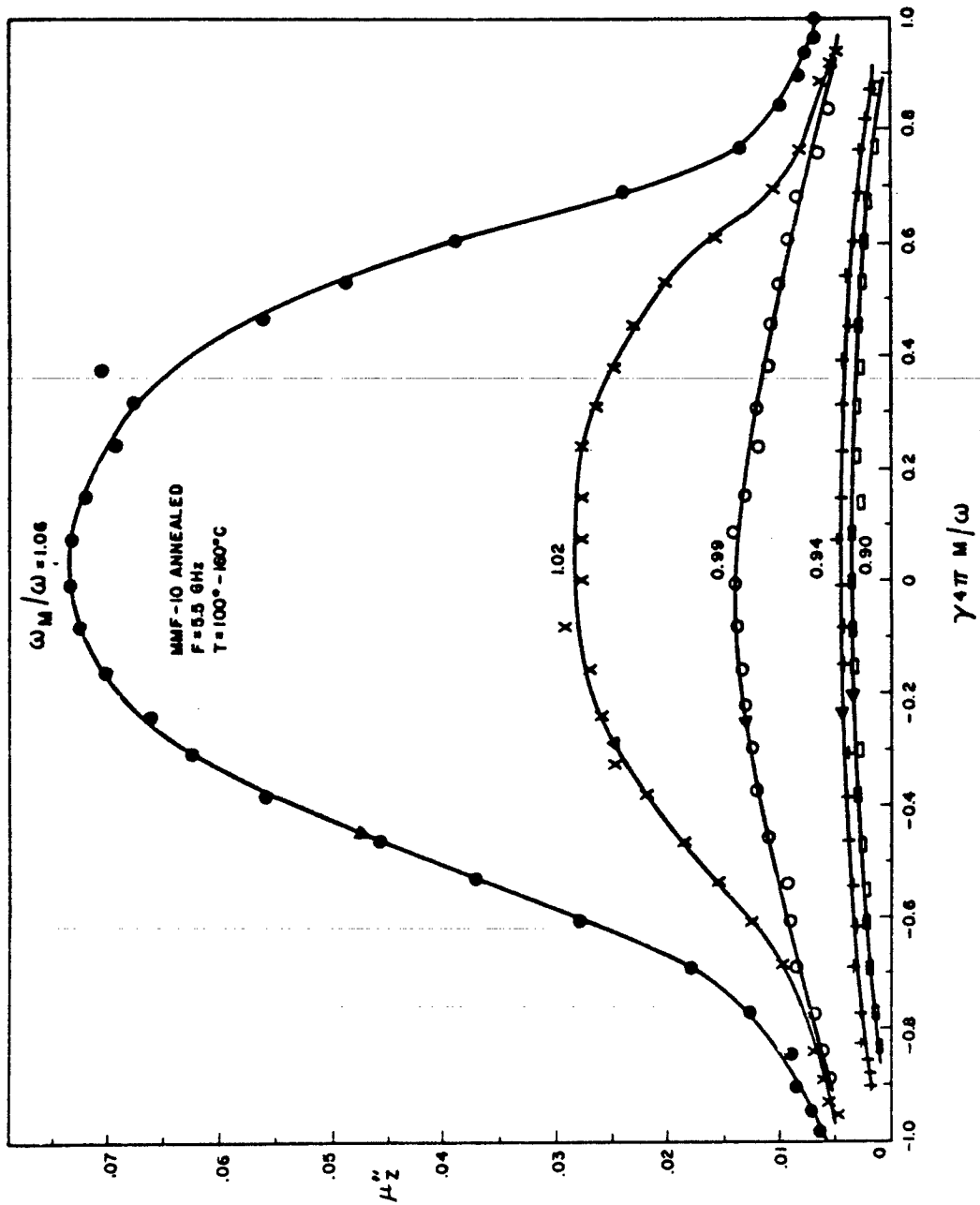


Fig. 27 μ_z'' vs $\gamma 4\pi M / \omega$ for MMF-10 at 5.5 GHz

elliptical precessional motion and the coupling mechanism is the same as that which causes the parallel-pump instability at large rf fields.

The curves in Fig. 28 have been computed using the theoretical equations of Ref. 13. The exchange constant of YIG has been assumed for these curves; this is valid assumption only for YIG. Nevertheless, the results should be a reasonable approximation for other garnets and spinels whose magnetization differs from that of YIG but whose Curie temperatures are close to the Curie temperature of YIG. The curves in Fig. 28 give the subthreshold μ''_2 as a function of frequency for several values of $4\pi M_s$. It has been assumed that the temperature is room temperature, that the sample is saturated, and that the internal dc field is zero. It is necessary to plot μ''_2 in this fashion since it is not a function of only the ratio ω_M/ω . For values of $\omega_M/\omega < 0.8$, the μ''_2 is in the low 10^{-4} or in the 10^{-5} region. When ω_M/ω becomes small this subthreshold absorption may be one of the dominant contributions to μ'' and μ''_2 in the partially magnetized state.

In comparing values μ'' and μ''_2 in the demagnetized state for the same ω_M/ω values (where they are presumably equal), it should be remembered that ω_M will have errors of a few percent due to errors in magnetization measurement and deviation of γ from 2.8 MHz/Oe.

F. Low Magnetic Losses

Certain ferrimagnetic materials have magnetic losses, μ'' , that are much less than 0.001 in the demagnetized state, providing ω_M/ω is not close to one. However, values of μ'' as low as a few times 10^{-4} are difficult to measure accurately by cavity perturbation techniques, because a large sample is required in order to produce a measurable change in cavity Q. If the sample is made too large, the results of perturbation theory are not valid. For large samples an exact solution of the new cavity mode is necessary. This can be done only for certain specific geometries. We have chosen to use a rectangular cavity containing a thick slab that fills the entire

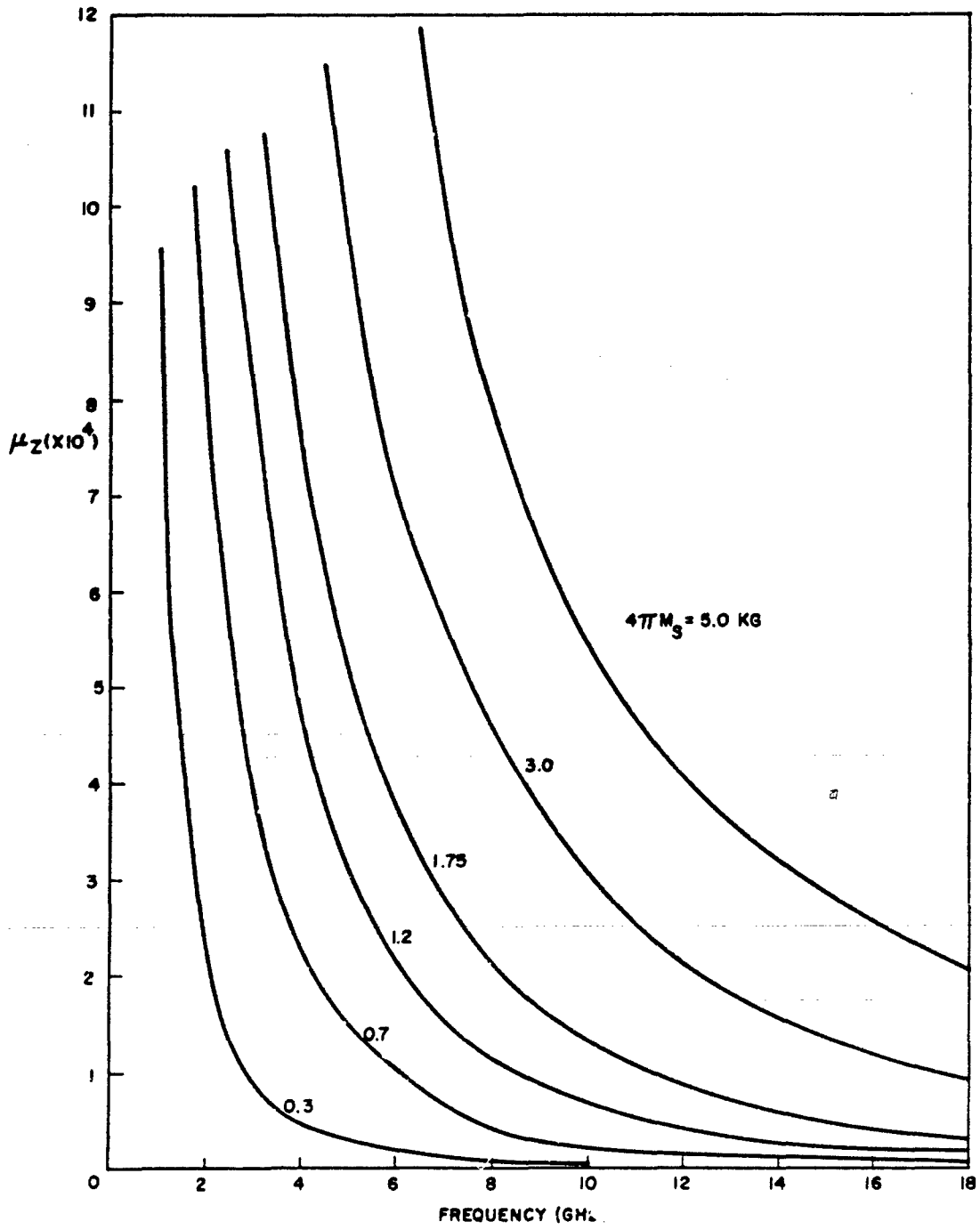
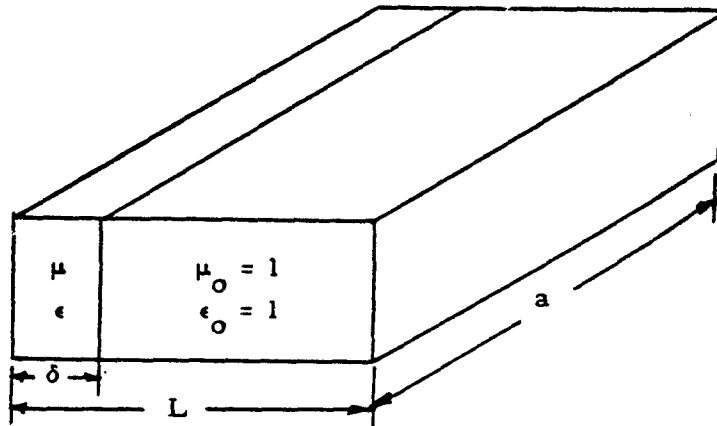


Fig. 28 Subthreshold μ_z'' vs Frequency

cross section at one end wall. A diagram of the cavity is shown in Fig. 29. The method of calculation of resonant frequency and cavity A as a function of the dielectric constant, ϵ , and complex permeability, μ , is outlined below.



Consider a slab of thickness δ in a rectangular waveguide cavity of length L . The cutoff frequencies of the waveguide are:

$$f_0 = \frac{c}{2a} \quad \text{in the empty part}$$

$$f_f = \frac{c}{2a \sqrt{\epsilon \mu}} \quad \text{in the filled part}$$

where a is the width of the waveguide. The propagation constants in the two parts of the waveguide are given by:

$$\gamma_0 = j \frac{2\pi f}{c} \sqrt{1 - \left(\frac{f_0}{f}\right)^2} \quad \text{in the empty part.}$$

$$\gamma_f = j \frac{2\pi f \sqrt{\mu \epsilon}}{c} \sqrt{1 - \left(\frac{f_f}{f}\right)^2} \quad \text{in the filled part.}$$

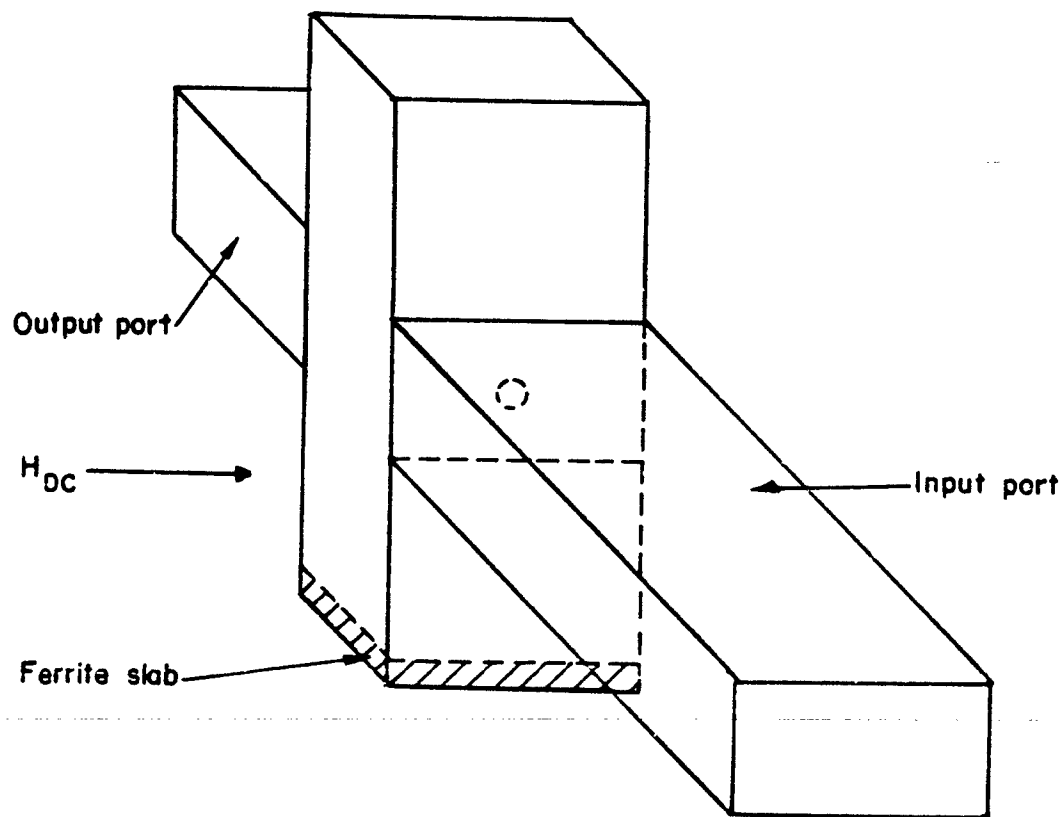


Fig. 29 Rectangular TE_{102} Cavity for Measuring Very Low μ''

The characteristic impedance of each part of the waveguide is:

$$Z_o = \sqrt{1 - \left(\frac{f_o}{f}\right)^2} \quad \text{in the empty part,}$$

$$Z_f = \sqrt{\frac{\mu}{\epsilon}} \sqrt{1 - \left(\frac{f_f}{f}\right)^2} \quad \text{in the filled part.}$$

The cavity is made by placing a short at each end of the waveguide. Standing at the interface between the ferrite-filled and empty waveguide, and looking down the empty waveguide toward one short, one sees an impedance

$$Z = Z_o \tanh(\gamma(L-\delta))$$

Looking back into the ferrite-filled waveguide, one sees an impedance

$$Z = Z_f \tanh(-\gamma\delta)$$

Equating these two values for the impedance gives

$$Z_o \tanh(\gamma(L-\delta)) + Z_f \tanh(\gamma\delta) = 0$$

Using this equation and the preceding equation for Z_o , Z_f , γ_o , γ_f , f_o , and f_f , one can, with the aid of a digital computer, solve for any one of ϵ , μ , L , and the resonant frequency f in terms of the other three. Naturally if μ is complex the resonant frequency must also be complex, its imaginary part being $f'' = f'/2Q$

In practice the procedure used is the following. The frequency of the empty cavity is first measured and used to compute the effective length of the cavity to the accuracy of the frequency measurement. Then the sample is inserted and a large dc magnetic field is applied parallel to the rf magnetic field in the sample. This makes $\mu = 1$ and allows the effective dielectric constant, ϵ , to be computed. This effective dielectric constant

may be slightly less than the real dielectric constant since there must be some very small air gap between the sample and broad wall of the waveguide. This gap acts as small capacitance in series with the large capacitance of the high dielectric constant ferrite and the net effective dielectric constant is given by

$$\epsilon_{\text{eff}} = \epsilon \left(1 - \frac{d\epsilon}{b} \right)$$

where d is the gap thickness and b is the height waveguide, 0.62 in. at 5.5 GHz. If $d = 0.002$ in. and $\epsilon = 16$ the correction factor is 0.95. In addition, the measurement of the effective dielectric constant on the sample in question automatically takes into account any variation in dielectric constant from sample to sample.

The dc field is then reduced to zero and the sample demagnetizes in its own demagnetizing field. The resonant frequency and cavity Q are again measured. Using the change in f'/Q for f'' in the preceding equations, we can calculate μ' and μ'' . While this technique has been used successfully to measure cases of $\mu'' < 10^{-4}$, there is one precaution that must be taken. We have neglected the skin losses in the waveguide by using the change in (f'/Q) from high to zero field for f' . In doing this, we have assumed that the skin losses are unchanged from high to zero field and hence could be ignored. In fact, this is not true, since μ' and therefore resonant frequency change, the skin depth and losses also change. Furthermore, the rate of energy loss into the waveguide walls adjacent to the material depend directly on the dielectric constant and permeability of the adjacent material. This also causes a change in Q from high to zero field. Finally, the relative energy stored in the two parts of the cavity changes as μ' changes and causes a further change in Q . All these changes can be calculated in straightforward, although tedious, manner since the field patterns can be obtained exactly throughout the cavity.

The error in μ'' is given by $(\partial \log Q / \partial \log \omega - 1) \Delta\mu' / 2Q$ where $\Delta\mu'$ is the change in μ' from high to zero field and $\partial \log Q / \partial \log \omega$ is the logarithmic

change in Q with frequency as μ' is varied. For a TE_{102} cavity made of 1.37×0.62 in. copper waveguide 2.435 in. long whose resonant frequency is 5.5 GHz, the calculated values of the factor $(\partial \log Q / \partial \log \omega - 1) / 2Q$ are given below for various thicknesses of ferrite slab with an $\epsilon = 15$.

Thickness	$(\partial \log Q / \partial \log \omega - 1) / 2Q$
0.20	-0.3×10^{-4}
0.040	0.2×10^{-4}
0.060	0.7×10^{-4}
0.080	0.6×10^{-4}
0.100	2.7×10^{-4}
0.120	3.8×10^{-4}

Since $\Delta\mu'$ is typically 0.01 to 0.1 for very low loss materials with $\omega_M / \omega \ll 1$ the error in μ'' will generally be insignificant. However, as the slab thickness increases and more of it is in the region where the electric field is not zero, its large dielectric constant causes substantial changes in the stored energy and wall loss. Thus this factor can be seen to increase rapidly. Some care must be taken not to use an excessively large sample unless μ'' is small enough to require it and $\Delta\mu'$ is small enough to allow it.

We have made preliminary measurement on several materials at frequencies from 5.5 to 16.5 GHz. These include G-113, TT1-390, MMF-10, G-800, G-1004, and a Raytheon yttrium iron aluminum garnet (YFA) with a magnetization of $4\pi M_s = 300$ gauss. The results are summarized in Fig. 30. Some of the data can be refined further. Many more points are needed on several of these samples to completely evaluate their frequency dependence. The most extensive data shown is for G-113 covering the range from 5.5 to 13 GHz. The results obtained at 16.5 GHz were too small to be considered meaningful for this material. In this case the correction described above for the change in cavity wall loss with frequency overwhelms the material loss.

We have shown earlier in this report that for ω_M/ω not close to 1.0 $\kappa'' \ll \kappa'$ and μ'' is not a strong function of $4\pi M$. We can, therefore, characterize the transverse loss as a function of ω_M/ω by the single value given in Fig. 30. We see that for any given ω_M/ω the loss of G-113 is less than that of the magnesium manganese ferrites which in turn is less than that of the substituted garnets.

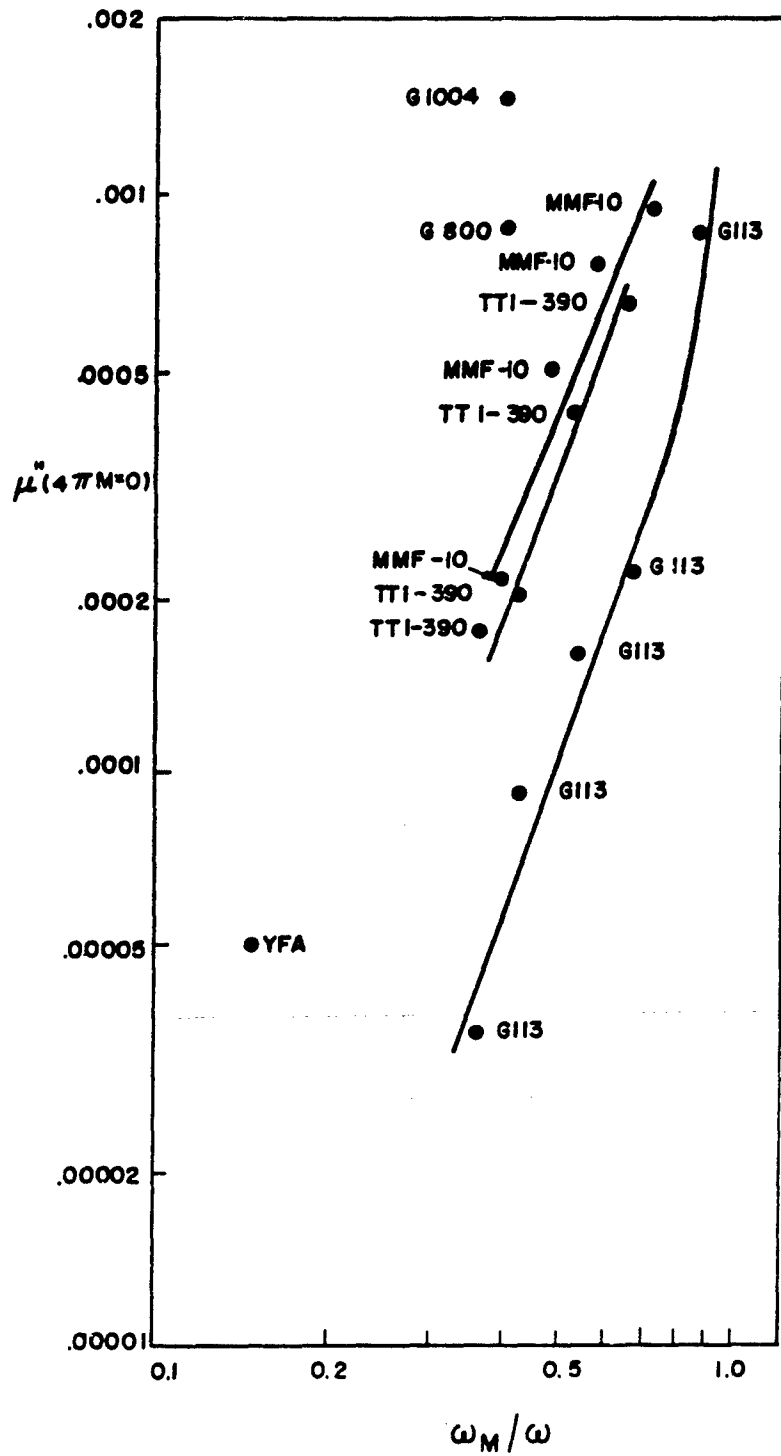


Fig. 30 μ'' vs ω_M/ω at $4\pi M = 0$ for Low Loss Materials

III. THE HIGH POWER PROPERTIES OF PARTIALLY MAGNETIZED MATERIALS

A. Introduction

Considerable interest in microwave devices incorporating partially magnetized magnetic materials has developed in recent years. To obtain acceptable high power performance, it is necessary that concepts exist which can be used during the design to optimize peak power performance. However, the polycrystalline materials of importance in device design usually possess a complex domain structure when partially magnetized or demagnetized, and the characterization of the high power properties is extremely complicated. Virtually no systematic study of the high power properties of such systems has been reported. Experimental work to date has used small spherical samples magnetized to saturation either parallel or perpendicular to the direction of the linearly polarized microwave field. Furthermore, the theoretical work concerning the spinwave instability processes which determine high power performance has limited applicability. The Suhl theory¹⁴ of instability processes applies only to samples of ellipsoidal shape, magnetized to saturation along an axis of rotational symmetry, and, for a circularly polarized microwave field, perpendicular to this axis rotating in the proper sense to excite ferromagnetic resonance. Schlömann's theory of parallel pumping¹⁵ is valid for a linearly polarized microwave field in the direction of saturation for ellipsoidal-shaped samples. In short, the published work concerning high power properties of ferromagnetic insulators, both experimental and theoretical, does not provide an adequate basis for optimizing peak power performance of devices incorporating partially magnetized materials.

The general objective of this investigation was to initiate a program to understand the parameters which determine the high power properties of such systems, both experimentally and theoretically. The approach taken in this initial study is based on the original Polder-Smit⁴ concept that, for partially magnetized systems, the local internal fields are determined by

domain distributions and domain shapes, in much the same way that they are determined by the sample shape for saturated materials. Consequently, two specific related objectives have been followed: 1) To characterize the peak power properties of saturated materials as a function of sample shape and microwave field configuration; 2) To relate the conclusions for saturated systems to results for partially magnetized samples on the basis of domain shape considerations. The problem has been approached essentially from a microscopic point of view where the partially magnetized system is viewed as a collection of domains, each of which behaves as a saturated sample with a shape defined by the domain geometry. By reducing the partially magnetized sample to a collection of saturated sample-like regions, the problem has been reduced to tractable form and can be treated on the basis of theoretical considerations for saturated systems. This approach has proved quite successful.

It is important to indicate what types of high power measurements are likely to yield useful and pertinent information concerning peak power limitations for partially magnetized and saturated materials of interest. The peak power handling capability of microwave magnetic materials is determined by the magnitude of the microwave susceptibility at high power levels. Prior to this work, three phenomena had undergone extensive experimental investigation: saturation of the main resonance, subsidiary absorption, and parallel pump absorption. For each of these phenomena, the nonlinear coupling which exists between the normal modes of the magnetic system (spinwaves) leads to a parametric excitation of certain modes when the microwave field amplitude exceeds a critical threshold value. The possibility of such excitations must be taken into account in device design. The saturation effect consists of a decrease in the susceptibility for materials biased near ferromagnetic resonance. This saturation causes a decrease in the isolating ability of a material used in a resonance isolator if the critical power is exceeded. Subsidiary absorption corresponds to an increase in the susceptibility for materials biased well below ferromagnetic resonance, and leads to an increase in insertion loss at high power

for a phase-shifting device using the material. Parallel pump absorption is similar to subsidiary absorption, but occurs for the microwave field parallel to the static biasing field.

In considering these and related phenomena, their relative order of importance depends on the specific application and the particular high-power requirements of the device. In order to minimize the insertion loss for phase-shifting devices using partially magnetized materials, the materials are usually chosen with a magnetization sufficiently low that the local internal fields are much less than required for ferromagnetic resonance at the frequency of operation. Insofar as no part of the material in the resonant device is biased near resonance, saturation of the resonance need not be considered in characterizing the high-power properties of such materials. The relevant phenomena of importance for partially magnetized magnetic materials are related to subsidiary absorption and parallel pumping absorption, which do occur at fields less than required for resonance. Both are associated with so-called first-order spinwave instability processes. In the actual devices, moreover, more complicated microwave field configurations may exist, and first-order instability processes for such configurations must also be considered. The experimental approach, therefore, has been to examine the instability threshold for samples biased far below resonance and to interpret the results in terms of first-order instability processes.

The investigation can be conveniently divided into three parts concerned with 1) the characterization of peak power properties as a function of static field, sample shape, microwave field configuration, and state of magnetization; 2) the theoretical description of spinwave instability processes for more general sample shapes and pump configurations than previously reported, and 3) the application of the theory to the various experimental results.

Data were obtained for different sample shapes and pump arrangements which were expected to be directly related to the magnetic environments

for partially magnetized systems: 1) The influence of gross changes in sample shape on the threshold was examined by considering perpendicular pumping for axially magnetized rods, spheres, and normally magnetized disks. The rod data were found to be particularly important, since many partially magnetized systems consist of elongated rod-shaped domains; 2) Parallel and perpendicular pumping in thin disks as a function of field and pump direction were also examined. Thin disks were examined in detail for two reasons. First, many remanent devices incorporate materials with slab geometry, so that the results are likely to be directly applicable to device design. Second, the domain structure for thin disks can be approximated by simple models, such as proposed by Kittel,¹⁶ and the results for partially magnetized disks should be related to the theory for saturated systems according to the above reasoning. Because the actual pump environment for partially magnetized systems is likely to be more complicated than simple parallel or perpendicular pumping, other pump configurations were also investigated; 3) Pumping with a circularly polarized field rotating in the proper sense to excite ferromagnetic resonance and in the opposite sense were examined. Pumping with a linearly polarized microwave field at an angle between zero and 90° to the static field was also considered. The results of these experiments were used in two ways. Data for samples magnetized to saturation were used to determine the influence of sample shape and pump configuration on the threshold. Data for partially magnetized samples were used to establish a connection between domain structure and the threshold fields, guided by the shape information obtained for the saturated samples.

The general theory of first-order instability processes is developed in Appendix I. Specific equations are developed which apply to the experimental situations described above. This theory provides the basis for a quantitative comparison of the various experimental results. The data for saturated systems can be explained in terms of the above theory. The theory is applicable to partially magnetized materials if domain structure is taken into account. Additional results (for oblique pumping in spherical samples as a function of angle between the static and microwave field) are presented in Appendix II, these results are in agreement with the above conclusions.

In the next section, the instrumentation which was developed partly in conjunction with this program is described, and the experimental technique is briefly summarized. A large amount of data was required in the course of the investigation, and an automated system to determine the instability threshold was, therefore, developed. This system is described in the following three sections; the experimental results are presented for each of the above experiments and discussed in terms of theory. In each of these presentations, the emphasis is on shape and pump configuration effects for saturated systems and, where possible, the relation to domain shape effects on h_{crit} for partially magnetized systems.

B. Experimental Technique and Instrumentation

Although experimental techniques for determining the instability threshold in ferromagnetic insulators are well known,¹⁷ several aspects of the present technique and the instrumentation developed partly in conjunction with this program depart significantly from previous procedures. The departures consist primarily in 1) automating the instrumentation used to determine the threshold amplitude, and 2) introducing sample alignment procedures for nonspherical samples. The first was considered necessary because of the large amount of data required in the present program. The second was required because of the emphasis of peak-power properties as a function of sample shape, and was particularly important for samples with slab geometry. Both of these will be considered in detail below. In discussing the automation procedure, we will briefly review the basic considerations concerning microwave susceptibility, cavity fields, and microwave power which are necessary in applying microwave measurement techniques to the understanding of physical phenomena.

The basic procedure for determining the first-order instability threshold, h_{crit} , is to measure the imaginary part of the diagonal component of the effective or external susceptibility tensor, which is conventionally denoted as χ_e'' , as a function of the applied microwave field amplitude, h , at the sample position. Using standard cavity perturbation techniques reviewed in Ref. 17, χ_e'' can be calculated to be

$$\chi_e'' = \frac{2gV_c}{V_c} \frac{1}{Q} \frac{\Gamma_s - \Gamma_o}{1 - \Gamma_s} \quad (17)$$

where V_c and V_s are the cavity and sample volumes, respectively, Γ_s and Γ_o are reflection coefficients for the cavity with and without the magnetic specimen, and g is a geometric factor related to energy storage in the cavity given by

$$g = \frac{1}{8} \left[1 + \frac{d^2}{n^2 a^2} \right] \quad (18)$$

for a TE_{10n} rectangular cavity where d is the cavity length, a is the cavity width, and n is the mode index corresponding to the number of half-wavelengths along the length of the cavity. At low microwave power levels, the susceptibility χ_e'' is independent of the microwave field amplitude h and Γ_s is constant, for fixed static field. As the microwave power level is increased to the point where h at the sample position exceeds the threshold value for the excitation of spinwave instabilities, χ_e'' increases sharply. Experimentally, this phenomenon is evidenced by an increase in the reflection coefficient Γ_s for the cavity containing the sample. The standard experimental procedure is to measure Γ_s as a function of the microwave field amplitude h , calculate χ_e'' from Eqs. (17) and (18), display χ_e'' vs h graphically, and determine h_{crit} as the break in the curve which separates the constant χ_e'' region from the increasing χ_e'' region. Such a procedure is extremely time-consuming, because considerable data are required to determine a single value of h_{crit} . Values of h_{crit} as a function of a number of parameters (such as sample shape, sample orientation, microwave field configuration, and static field) require extensive data. A complete point-by-point characterization of high-power properties would be impractical. A semiautomatic instrumentation system has, therefore, been developed to simplify the above procedure considerably. The system allows curves of $\log \Gamma_s$ to be plotted as a function of h^2 . Values of h_{crit} can be easily and rapidly determined from the curves generated.

The system is designed around a standard reflection-cavity microwave spectrometer;¹⁷ the microwave instrumentation is indicated schematically in Fig. 31. The basic system consists of a 2J51 magnetron source operated in a pulsed mode, which feeds a TE_{102} rectangular reflection cavity through a series of high-power attenuators and a high-power isolator. A peak power of 1 kW incident upon the cavity could be obtained. Directional couplers sample the incident power into reference arm A and the reflected power into cavity arm B. A commercial self-balancing microwave power meter with a temperature-compensated thermistor mount was used to monitor the average power level in the reference arm and to provide a voltage output proportional to this power for the x-axis of the x-y recorder. A second directional coupler in the reference arm feeds the crystal detector through one side of the microwave switch. The detector monitors the reflected power in the cavity arm through the other side of the switch. Attenuators are provided in both the reference and cavity arms to adjust the signal levels, and to facilitate point-by-point measurements when the automatic feature is not desired. The electronic circuits provide appropriate pulses to control the magnetron output and to drive the microwave switch. The system output consists of a dc voltage proportional to the logarithm of the cavity reflection coefficient Γ_s . This voltage is applied to the y-axis of the recorder. In operation, the output voltage is constant and independent of the power level, as long as the microwave field amplitude at the sample does not exceed the instability threshold amplitude. In this field region, the recorder trace consists of a horizontal line, as indicated on the left side of the x-y recorder plot shown in Fig. 31. As the field amplitude exceeds some critical value, $\log \Gamma_s$ increases, the recorder curve exhibits a break and then increases with positive slope. The break point corresponds to the instability threshold.

Before considering the electronic instrumentation in more detail, it is necessary to indicate the various functions which such instrumentation must perform in order to obtain the recorder output described above. The sequence and relative timing of the various pulses are indicated in Fig. 32.

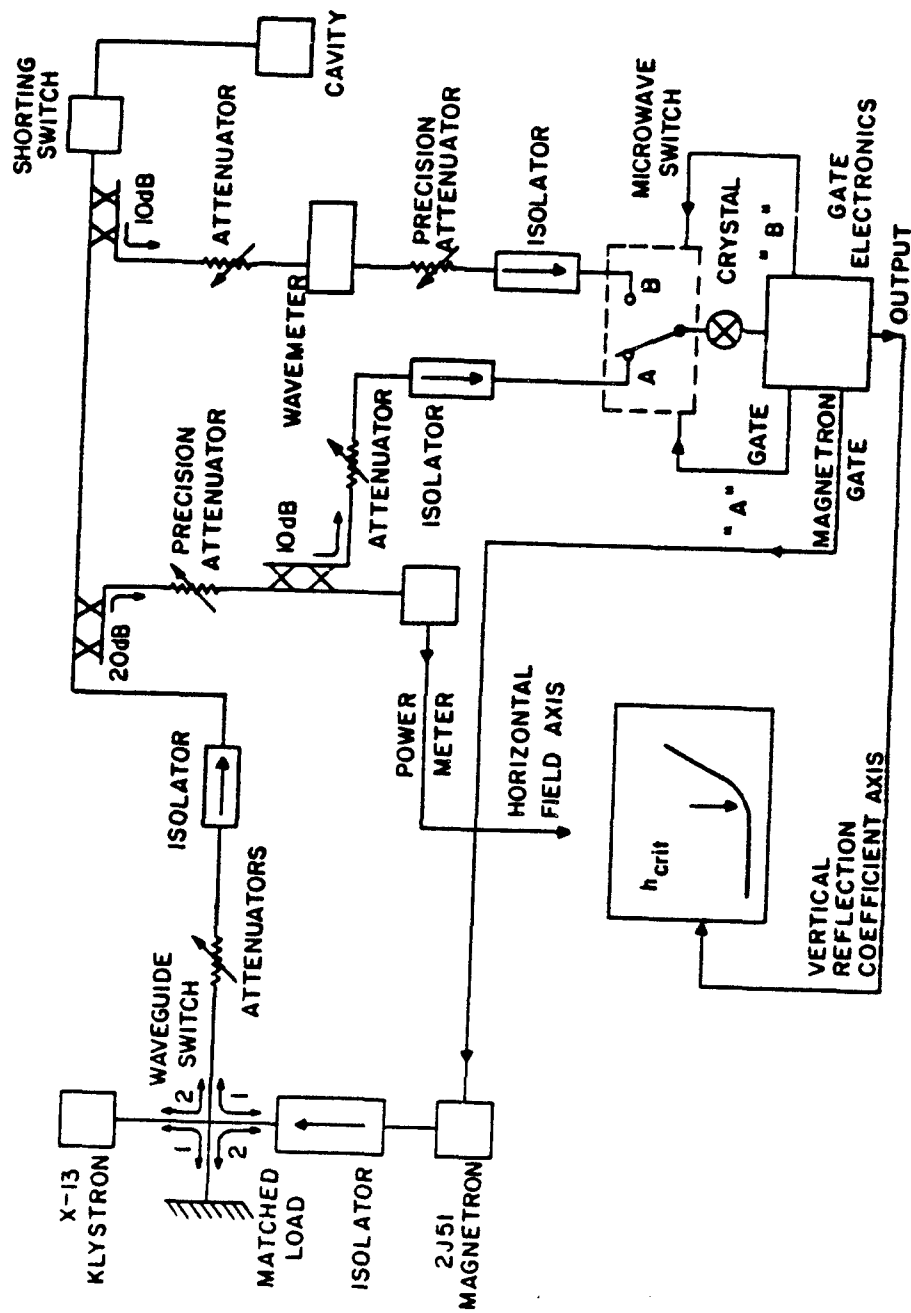


Fig. 31 Block Diagram of the Microwave System and General Instrumentation for the Semiautomatic System for Determining Instability Threshold Fields.

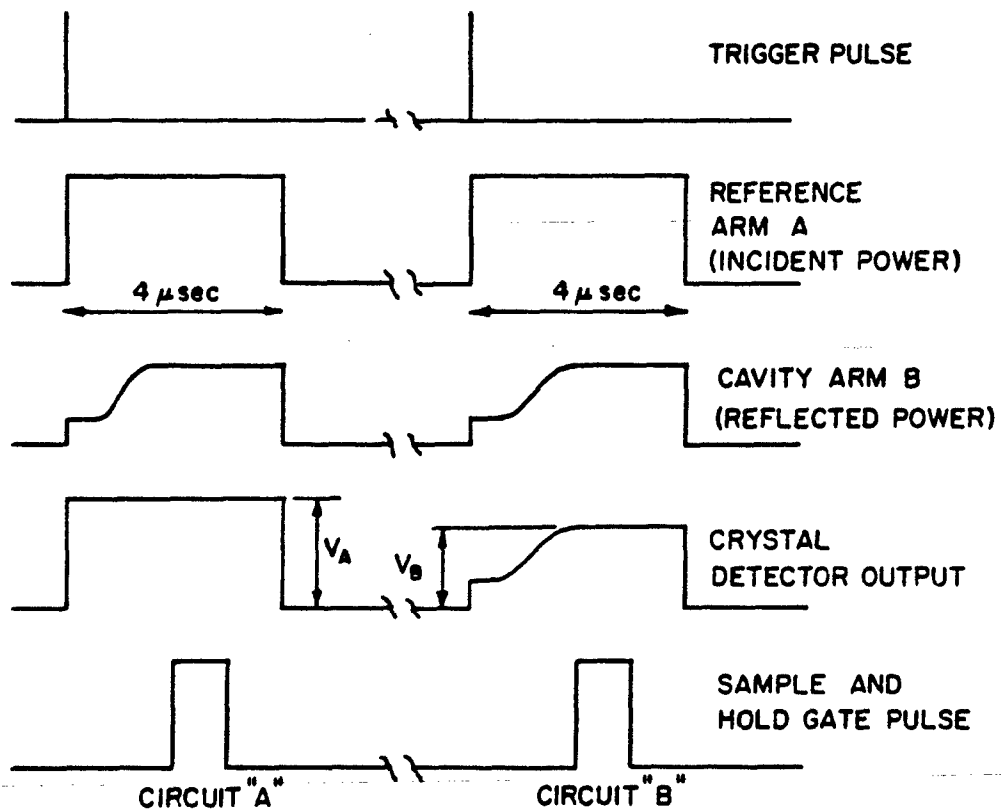


Fig. 32 Schematic Representation of the Relevant Pulse Sequences for Operation of the Semiautomatic System

Each trigger pulse initiates a 4 μ sec magnetron pulse, which is monitored by the reference arm. The reflected power from the cavity is monitored by the cavity arm. The pulse shapes for this reflected arm, shown in Fig. 32, indicate the typical shapes expected when the microwave field amplitude is above threshold. The crystal detector is switched to sample each arm on alternate pulses. As shown in Fig. 32, the detector output will correspond to the incident power on one pulse and then to the reflected power on the next pulse. Information concerning susceptibility can be obtained from the reflection coefficient Γ_s , which is equal to the ratio of the reflected pulse amplitude V_B to the incident pulse amplitude V_A . In order to convert these amplitudes to dc levels, two sample-and-hold circuits, with appropriate gates, as indicated by the bottom pulse train in Fig. 32, must be used to sample the crystal output on alternate pulses. The quantity $\log \Gamma_s$ can then be conveniently obtained by feeding the sample-and-hold circuit outputs through logarithmic converters and then to a differential amplifier. This quantity ($\log \Gamma_s = \log V_B - \log V_A$) should be constant as long as the microwave field amplitude is below the threshold value and should increase as the threshold amplitude is exceeded. A sharper increase could be obtained by converting the voltage output to Γ_s using an anti-logarithmic converter after the differential amplifier, but in this investigation the thresholds were quite sharp without such conversion.

The electronic instrumentation developed to derive the y-axis deflection voltage proportional to $\log \Gamma_s$ is indicated in Fig. 33. A rate generator synchronized to the line frequency is used to provide trigger pulses for the magnetron pulse generator, the pulse generator for the sample-and-hold circuit gate pulse, and a bistable divider. The bistable divider drives an electronic switch which applies the sample-and-hold gate pulse to the "A" and "B" sample and hold circuits on alternate magnetron pulses, respectively. It also drives the microwave switch, so that the crystal detector output applied to the sample-and-hold circuits is derived from reference arm A when the sample-and-hold gate is applied to the "A" circuit, and from the cavity arm B when the gate is applied to the "B" circuit. Both voltages are derived from the same crystal detector

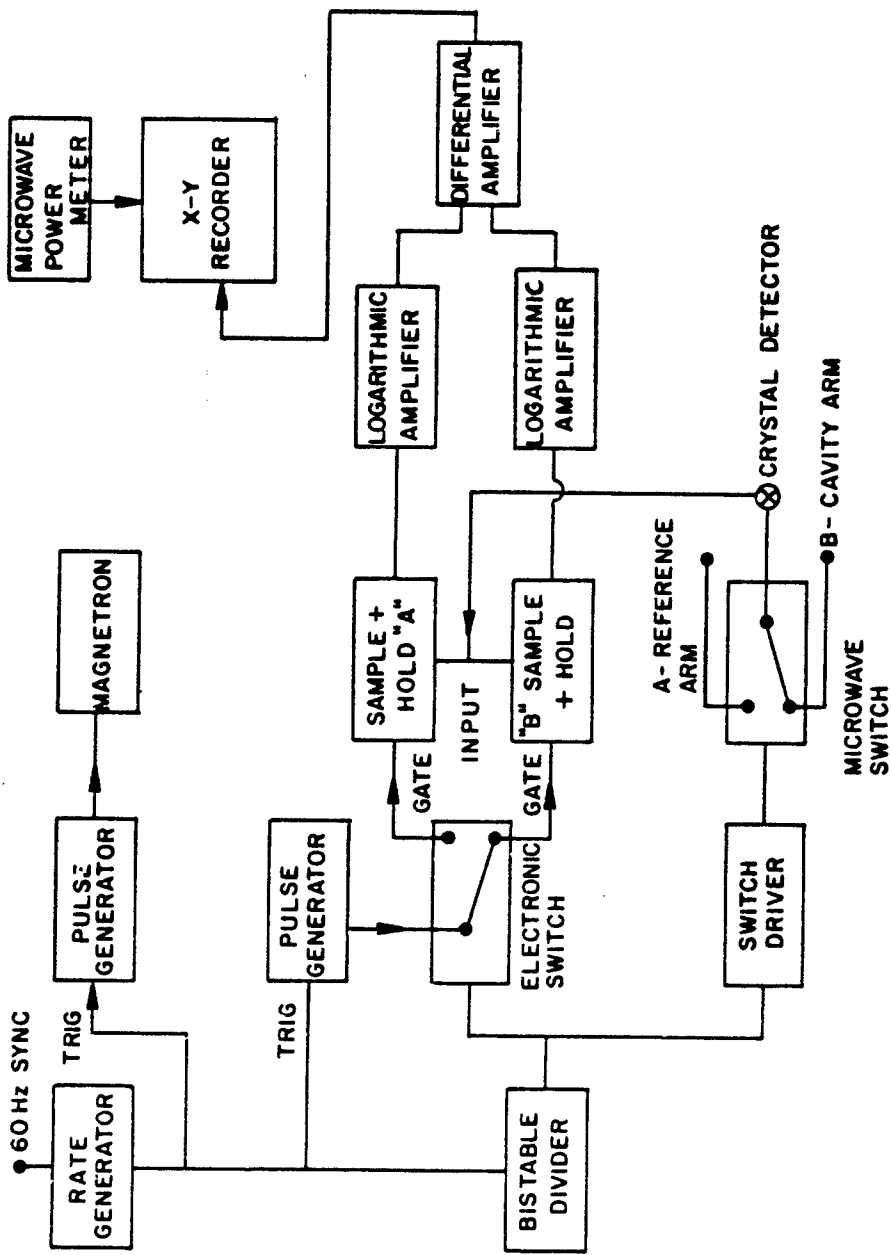


Fig. 33 Block Diagram of the Electronic Instrumentation for Semiautomatic System

output so that the tracking error which would result from using different crystals to monitor power levels in the reference and cavity arms is eliminated.

To determine the critical threshold field from the break point in the experimental curve, the only calibration required is for the horizontal or power axis in terms of the microwave field amplitude in the cavity at the sample position. Calibration of the peak power, P_{inc} , incident on the cavity, in terms of the average power monitored by the power meter in the reference arm can be easily obtained by mounting the thermistor power probe in place of the cavity, noting the conversion factor between this reading and the reference arm power, and determining the magnetron duty cycle. As reviewed in Ref. 17, the microwave field amplitude h_o can be calculated as a function of P_{inc} by considering energy transfer and storage for the cavity and the microwave field distribution inside the cavity. The result is

$$h_o = \frac{8\pi Q_o}{g V_c \omega} (1 - 10^{-\Gamma_o^{db}/20})^{\frac{1}{2}} P_{inc}^{\frac{1}{2}} \quad (19)$$

where Γ_o^{db} is the reflection coefficient of the empty cavity in db. The cavity Q without the sample, Q_o , and Γ_o^{db} are measured separately.

Data were obtained for a particular sample configuration by generating x-y recorder curves of $\log \Gamma_s$ as a function of average incident power with the static magnetic field as a parameter. The static magnetic field was measured using a Hall effect magnetic-field probe calibrated with proton nuclear magnetic resonance. For simplicity, the electromagnetic and Hall probe are not indicated in Fig. 31. Typical data are shown in Fig. 34. A horizontal scale calibration for h_o , obtained in the manner described above, is also indicated in that figure. The instability threshold field amplitude corresponds to the point where each curve breaks upward. Previously, each curve shown in Fig. 34 would have to be obtained from time-consuming point-by-point measurements of Γ_s^{db} as a function of microwave power level. All the above curves could now be obtained in a matter of minutes.

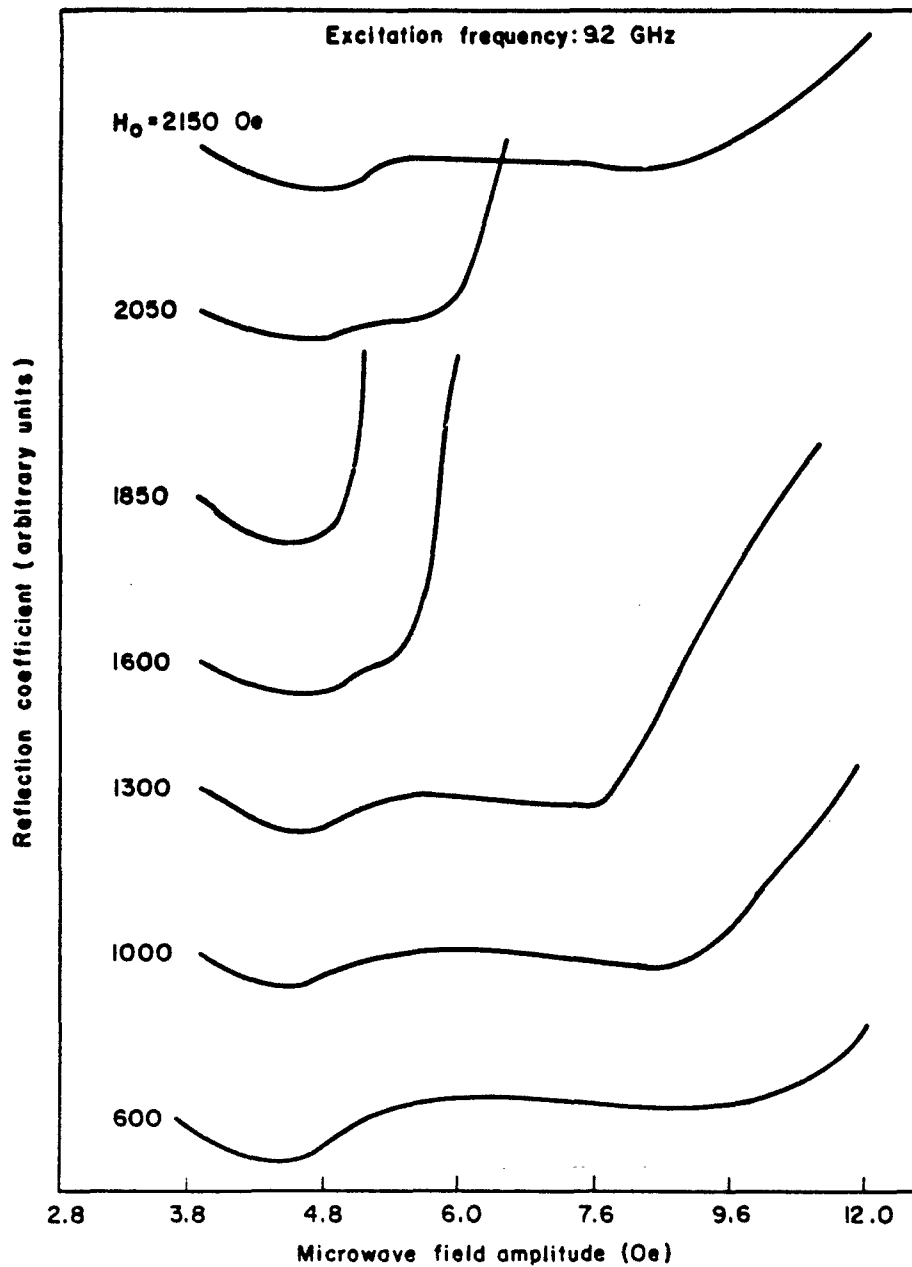


Fig. 34 Sample Recorder Outputs of the Cavity Reflection Coefficient as a Function of Microwave Field Amplitude. At successive static field values, the curves were shifted upward so that the different curves could be displayed conveniently on the same figure.

The second aspect of the experimental technique to be considered is the sample alignment procedure. The results for thin disks are quite sensitive to slab orientation. In order to ensure accurate sample alignment, an apparatus was designed to facilitate accurate sample positioning with respect to the static magnetic field direction. A photograph of this apparatus, installed on the magnet pole face and with the microwave cavity in position, is shown in Fig. 35. The cavity is mounted near the center of a circular lucite plate and connected to the microwave system by a section of flexible waveguide. The plate assembly is mounted in the gap of the electromagnet so that the polarization direction for the microwave magnetic field of the cavity is either parallel or perpendicular to the static field direction, depending on the pump orientation desired. The plate was pivoted at its center and provided with two adjustment screws spaced 90° apart on the edge of the disk for orientation purposes. The cavity plate was held under tension against the adjustment screw support points and center pivot point with rubber bands located near the adjustment screws, as well as on the opposite side of the disk. Sample alignment was usually accomplished at low power with the X-13 klystron microwave source shown in Fig. 31. By minimizing or maximizing the reflected power from the cavity with the sample biased on the low-field side of ferromagnetic resonance, depending on the sample shape and orientation, accurate alignment to $\pm 0.1^\circ$ could be accomplished.

Alignment was extremely critical, particularly for disk-shaped samples. To illustrate this point, data for perpendicular pumping are shown in Fig. 36 for a normally magnetized 0.020 in. thick and 1 cm diam disk of polycrystalline YIG at 9.2 GHz. Data were obtained with the static magnetic field at angle of 0, 5, and 15° to the disk normal. The threshold field h_{crit} is shown as a function of external static field. These data show that orientation has a significant effect of h_{crit} , particularly for the partially magnetized state (corresponding to static fields less than about 1750 G in Fig. 36). At a nominal field of 500 G, h_{crit} is reduced by almost a factor of two by the misalignment. This reduction corresponds to a factor of four reduction in the peak-power limitation for the material.

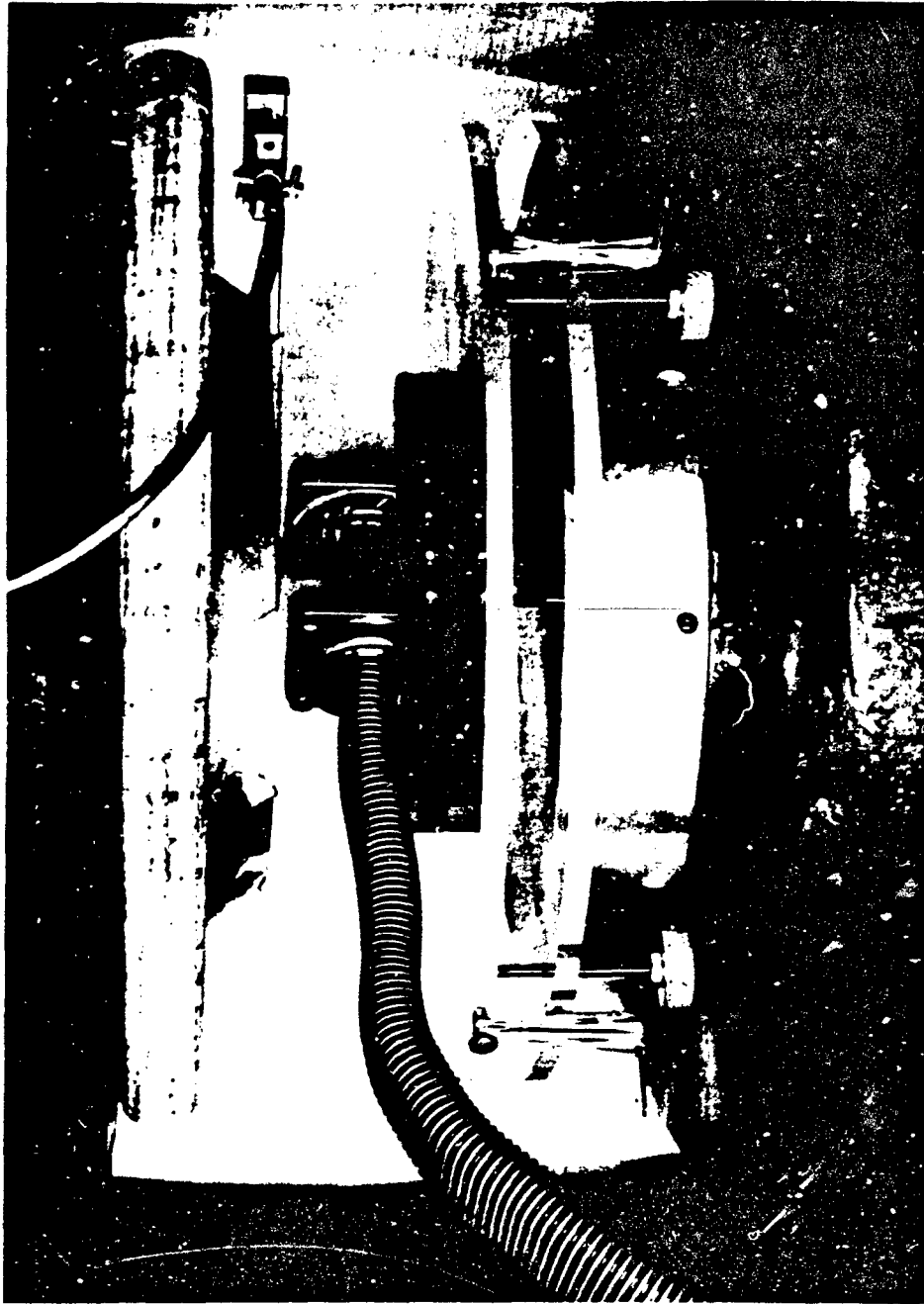


Fig. 35 Photograph of the Alignment Apparatus Utilized in Obtaining Data on Disk-Shaped Samples. The two knurled knobs allow the sample to be adjusted normal (or parallel) to the static field within $\pm 0.1^\circ$.

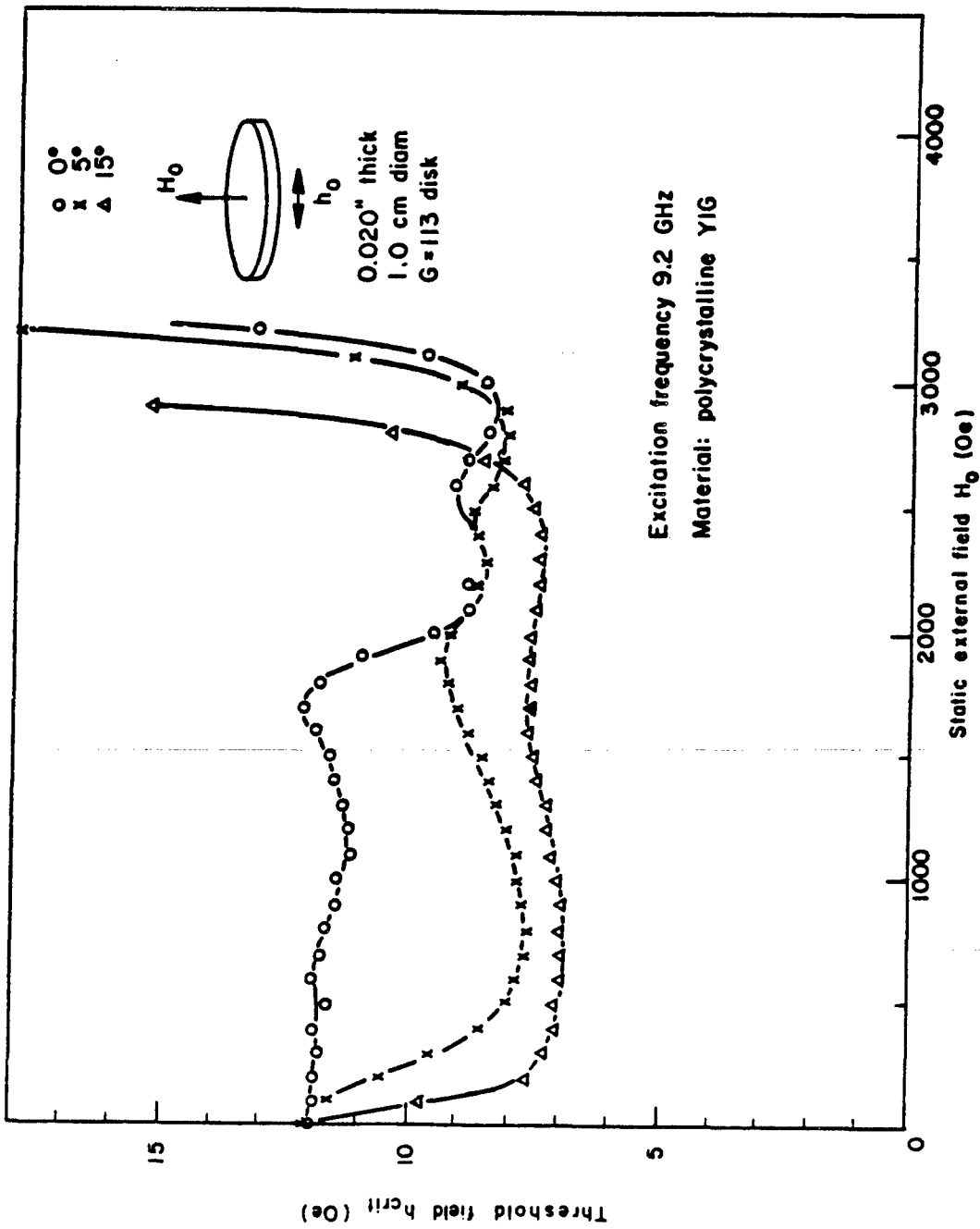


Fig. 36 Threshold Field h_{crit} as a Function of the Static External Field H_0 for Perpendicular Pumping with H_0 Normal to the Disk with the Misalignment Angle Between H_0 and the Disk Normal as a Parameter.

C. Sample Shape and the Perpendicular Pump Threshold

Large changes in sample shape have a profound influence on h_{crit} . In Fig. 37 the threshold field h_{crit} is shown as a function of static external field H_0 for perpendicular pumping in spheres, axially magnetized 40-mil diam rods, and normally magnetized 10-mil thick slabs of polycrystalline YIG. The data were obtained at 9.2 GHz and room temperature. Data are shown both before and after a 1 hr anneal at 1000°C. The threshold for the axially magnetized rod, indicated for unannealed and annealed rods by the open and solid circles respectively, decreases with increasing field, has a minimum of about 5Oe at a static field of about 1300 Oe, and then increases sharply. The results for the spherical samples, indicated for the unannealed and annealed materials by the open and solid triangles respectively, show a slow increase of H_0 less than about 600 Oe, then a decrease to a 5Oe minimum at a static field of 1900 Oe and then a sharp increase. Except for the shift to higher static field and the decrease in h_{crit} below 600 Oe, the experimental curve for the spherical sample is quite similar to that for the axially magnetized rod. The data for the 10-mil thick, normally magnetized slab are, however, quite different. In general, h_{crit} is significantly larger for the slab than for either the sphere or the rod geometry. The threshold increases from 12 Oe at zero external field to a maximum of 15 to 18 Oe at an external field of 1700 Oe, decreases sharply to a local minimum of 9 Oe at about 2300 Oe, exhibits a second local minimum at 2900 Oe, and then increases sharply at higher field. The discussion below will treat the three important features of the data evident from Fig. 37: 1) The influence of geometry on h_{crit} for saturated samples, 2) Behavior of h_{crit} for partially magnetized samples, 3) Annealing effects.

It is well known that the internal magnetic fields, both microwave and static, are influenced by geometry and that the action of these fields on the local magnetization determine, in part, the high-power properties of the material. The increase in field value for the minimum h_{crit} from rod to sphere to slab data is connected with an increase in the demagnetizing

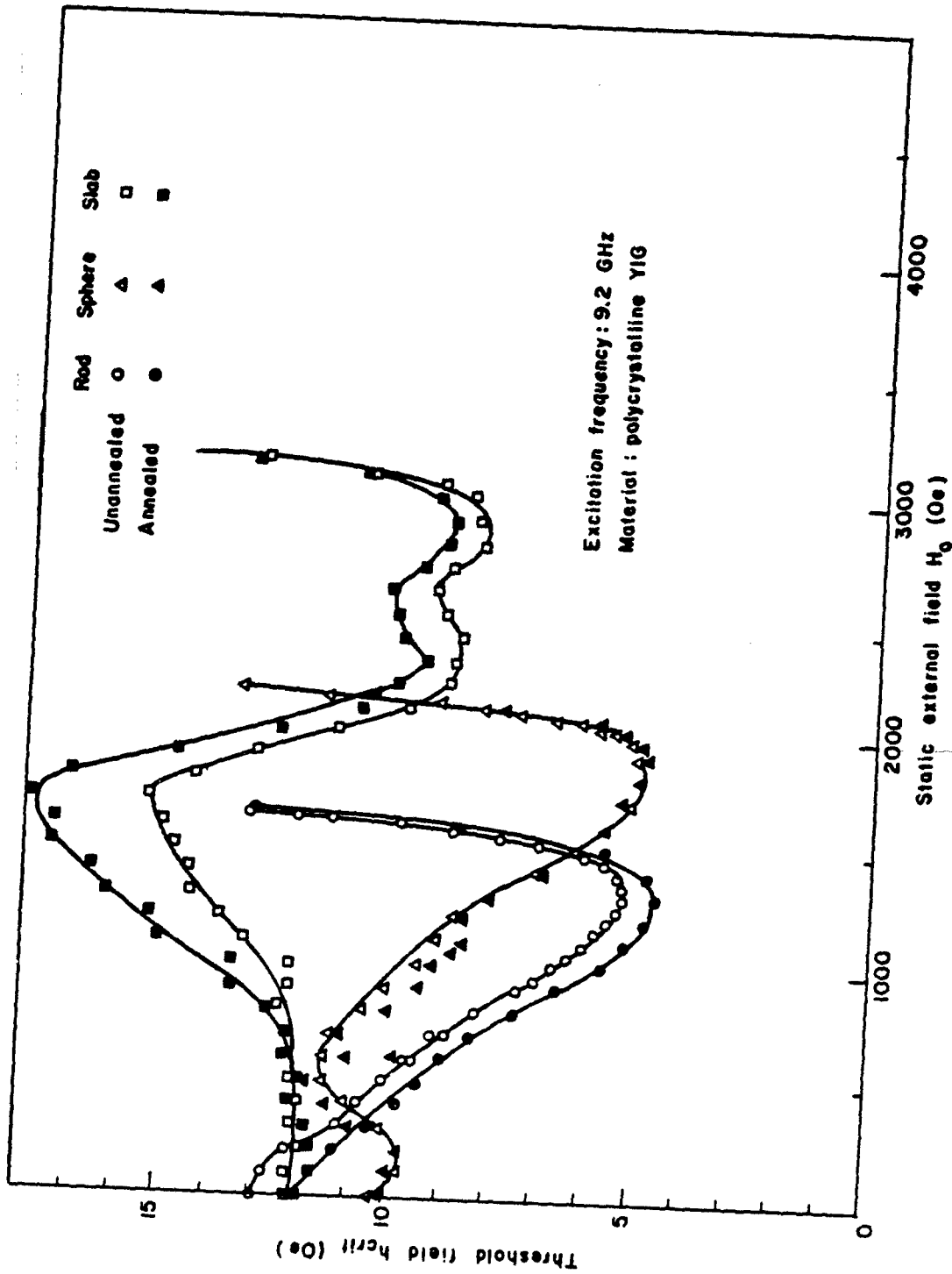


Fig. 37 Threshold Field h_{crit} as a Function of the Static External Field H_0 for Axially Magnetized 40 mil Diam Rods, 1 mm Diam Spheres, and Normally Magnetized 10 mil Thick, 1 cm Diam Disks, Before and After a 1 hr Anneal at 1200°C.

factor N_z in the static field direction, in going from a rod shape ($N_z \approx 0$) to a sphere ($N_z \approx 1/3$) to a slab ($N_z \approx 1$). The corresponding increase in the minimum h_{crit} from 4.6 Oe (rod) to 4.9 Oe (sphere) to 8.5 Oe (slab) is associated with a decrease in the efficiency with which the microwave field can excite the uniform precession mode.

These points can be demonstrated more quantitatively by considering theoretical curves of h_{crit} vs static field H_0 for the sample shapes of interest. The theoretical curves for comparison with the data in Fig. 37 as well as for comparison with the data to follow in the next two sections, were obtained according to the following procedure: 1) Data on spherical samples and the theory given in Appendix I were used to evaluate the spinwave linewidth as a function of spinwave number k and the spinwave angle θ_k , 2) The dependence of ΔH_k on k and θ_k was then incorporated into the theory for the rod and disk configurations and h_{crit} vs H_0 was calculated for these geometries. In other words, sphere data were used as a standard to obtain ΔH_k values which were then utilized to obtain theoretical curves for all other configurations. A comparison of the data for all configurations on the basis of derived $\Delta H_k(k, \theta_k)$ values might seem to be a more consistent approach. Inasmuch as ΔH_k is actually a derived quantity, a direct comparison of threshold field values seemed to be more appropriate.

The $\Delta H_k(k, \theta_k)$ results for polycrystalline YIG were obtained from parallel and perpendicular pumping data summarized in Fig. 38, using the theory given in Appendix I. The results of this determination are shown in Figs. 39a and b, where ΔH_k is shown as a function of k and θ_k for both parallel and perpendicular pumping.

It is important to realize that the portion of the threshold field vs static field curve of primary interest, the portion for static field less than that at the minimum h_{crit} position H_0^{min} , corresponds to $k > 0$, the spinwave linewidth is given by the results in Fig. 39b, which indicate that ΔH_k is essentially an increasing function of k and does not differ appreciably from parallel to perpendicular pumping, even though θ_k is quite different

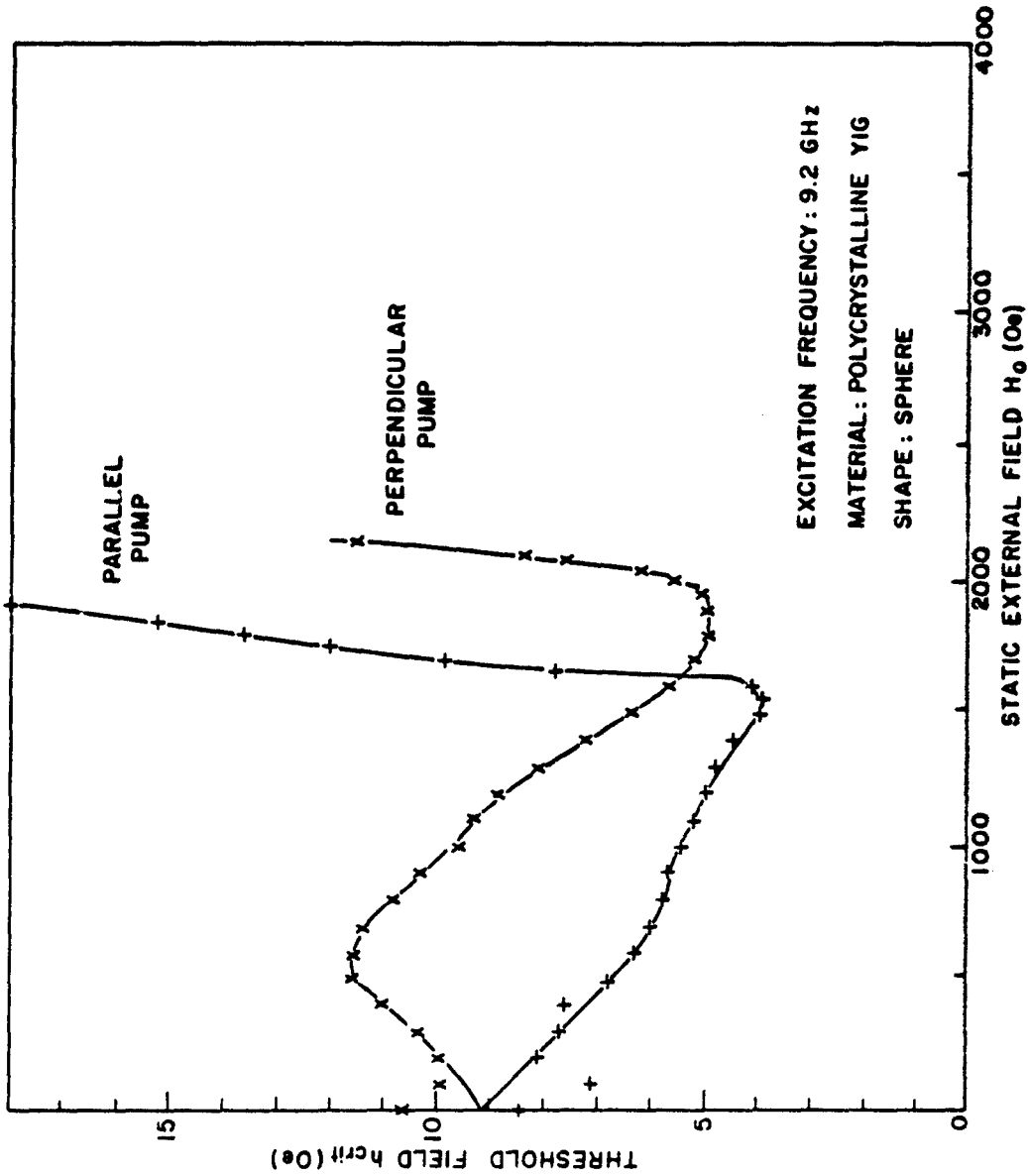


Fig. 38 Threshold Field h_{crit} as a Function of the Static External Field H_0 for the Annealed Spherical Sample of Fig. 7 and Both Parallel and Perpendicular Pump Configurations.

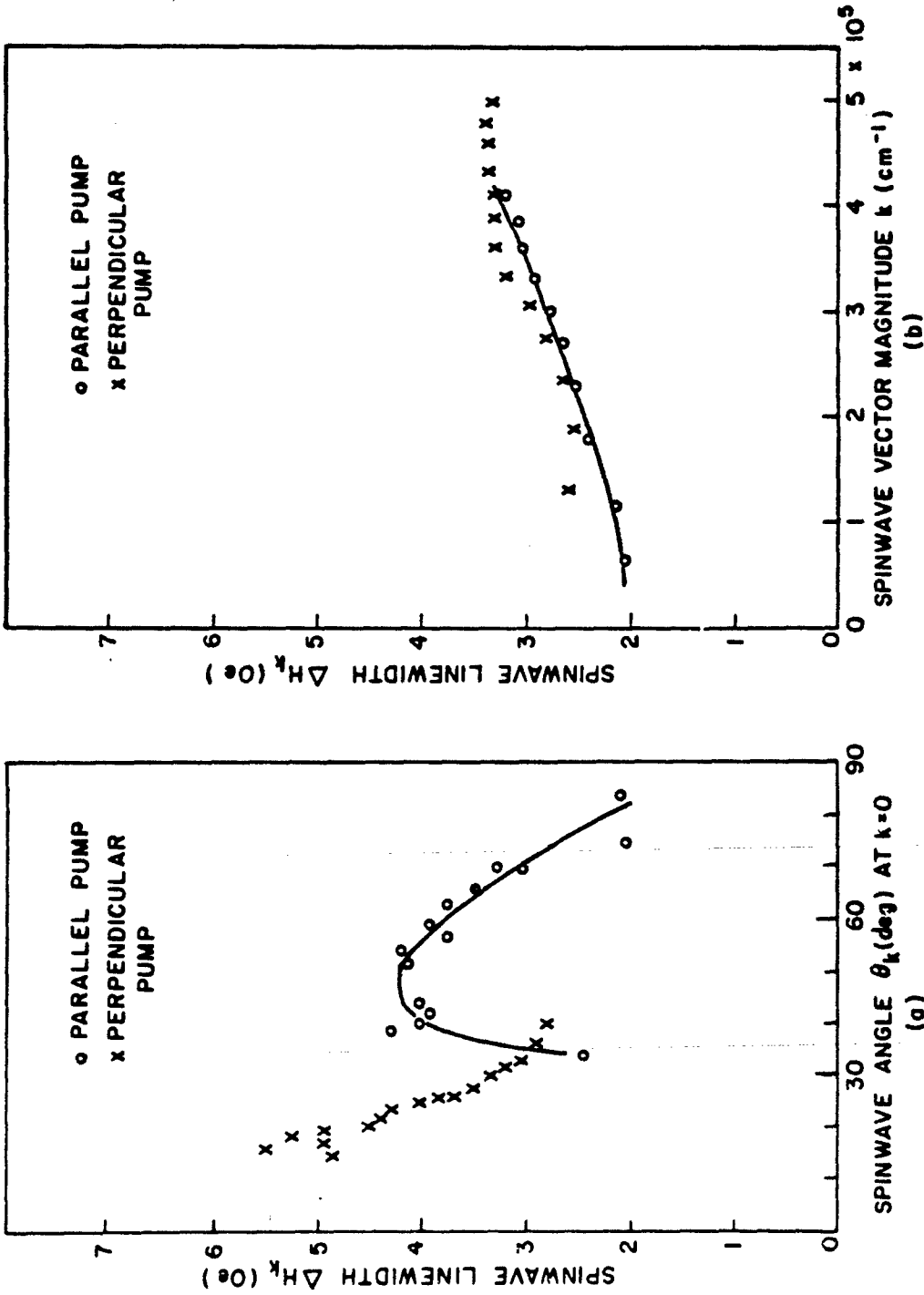


Fig. 39 (a) Spinwave Linewidth ΔH_k as a Function of Spinwave Angle θ_k for Parallel and Perpendicular Pumping and Wavenumber Equal to Zero
 (b) ΔH_k vs k for Parallel Pumping ($\theta_k = \pi/2$) and Perpendicular Pumping ($\theta_k \approx \pi/4$).

for the two configurations. Below the minimum h_{crit} position on the h_{crit} vs H_0 curve, corresponding to $H_0 < H_0^{\text{min, crit}}$, these results can be used to calculate theoretical h_{crit} values for the other field configurations and sample shapes of interest. The situation for $H_0 > H_0^{\text{min}}$ is more complicated. In this field region, the unstable spinwave generally corresponds to $k \approx 0$, and the ΔH_k determinations summarized in Fig. 39a must be used to calculate the theoretical curves. These determinations indicate that ΔH_k is not a single-valued function of θ_k for $k = 0$, but depends on the pump direction. For parallel pumping, ΔH_k has a maximum at $\theta_k \approx 50^\circ$. For perpendicular pumping ΔH_k increases with decreasing θ_k . The spinwave linewidth ΔH_k is generally considered to be a measure of the spinwave relaxation rate, a material parameter, and not expected to be a function of geometry. Although this expectation is fulfilled for $k > 0$ (Fig. 39b), it does not appear to be satisfied for $k = 0$, perhaps because the theory is not strictly applicable for $k = 0$. Even though the results are approximately correct, the ΔH_k do not correspond to spinwave ($\omega/2, k = 0, \theta_k$) but to magnetostatic mode excitations.¹⁸ The coupling to these modes should be strongly influenced by the microwave field direction. Such considerations are beyond the scope of this report and are not directly related to the present study. For the sake of comparison, the ΔH_k vs θ_k results shown in Fig. 39a will be used to calculate theoretical h_{crit} values for $H_0 > H_0^{\text{min}}$ using the ΔH_k determinations for parallel pumping when parallel-pump curves are to be calculated and for perpendicular pumping when perpendicular-pump curves are to be calculated. The meaning of theoretical curves for $H_0 > H_0^{\text{min}}$, however, is to be interpreted in light of the above considerations.

Using this procedure, ΔH_k determinations from the sphere data of Fig. 38 have been used to calculate theoretical threshold curves for perpendicular pumping with linearly polarized excitation in axially magnetized rods and normally magnetized slabs. In Fig. 40 the data for the annealed materials are shown again for comparison with theory. No theoretical curve is shown for the sphere, because those data were used to evaluate ΔH_k . The rod data are in close agreement with the calculated

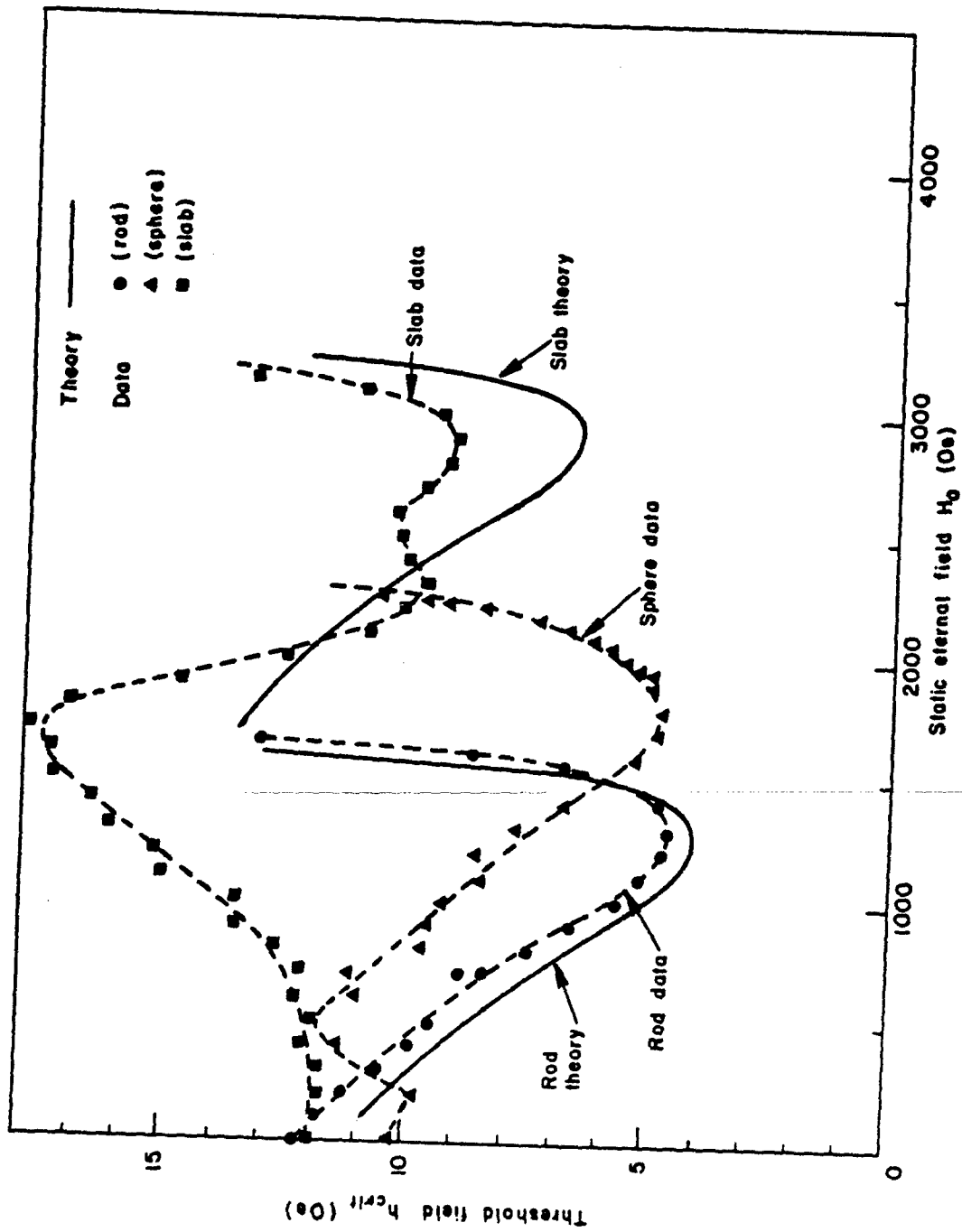


Fig. 40 Threshold Field h_{crit} as a Function of the Static External Field H_0 as in Fig. 7 for the Annealed Rod, Sphere, and Disk Samples, for Comparison with Theoretical Curves Obtained as Explained in the Text.

curve, which was obtained with no adjustable parameters. The difference is < 1 Oe and is probably related to the effect of annealing on the threshold. From Fig. 37, it is clear that annealing serves to reduce h_{crit} for the rod and further annealing might reduce the threshold still further and improve the agreement with the theory. The comparison between the data and theory for the 10-mil thick, 1-cm diam disk are also shown in Fig. 40. The calculated curve does not extend below 1700 Oe since the sample is not saturated at lower field, and the theory is not directly applicable. The agreement is not as good as it is for the rod geometry. The theoretical minimum is lower than the experimental minimum, and the calculated curve does not exhibit the double minimum indicated by the data.

The general increase in the minimum h_{crit} value in progressing from the rod to the sphere to the disk data is associated with the efficiency with which the microwave field pumps the uniform precession amplitude. For samples with rotational symmetry about the static field direction, the uniform precession amplitude due to the Larmor component of the pump field is given by

$$a_0 = \frac{h_0 e^{i\omega t}}{2(\omega_0 - \omega)}$$

where

$$\omega_0 = \gamma [H_0 + (N_t - N_z) 4\pi M_s] \quad (20)$$

is the natural precession frequency for the uniform precession mode. In the above expression, N_z and N_t are axial and transverse demagnetizing factors, respectively, h_0 is the microwave field amplitude, and $4\pi M_s$ is the saturation induction. In progressing from the rod with $N_z \approx N_t \approx 1/3$, to the disk with $N_z \approx 1$ and $N_t \approx 0$, the uniform mode amplitude decreases ($N_t - N_z$ decreases from $\frac{1}{2}$ to -1). In effect, the efficiency with which the microwave field pumps the uniform mode decreases and results in an increase in the h_{crit} required for instability to occur.

The differences between the slab data and the theory are probably associated with magnetostatic mode resonances which are excited in the disk because the pump field is not entirely uniform over the sample. Similar to the uniform precession, these modes are also coupled to the spinwave modes and can lead to instability. For a normally magnetized slab, magnetostatic mode resonances occur at static field less than that required for ferromagnetic resonance. It is suggested that the dip in h_{crit} near $H_0 = 2300 \text{ Oe}$ for the disk data in Figs. 37 is due to magnetostatic mode interactions. The strong coupling between the external microwave field and the various magnetostatic resonances is presumably accompanied by a decrease in coupling to the uniform mode. This decrease may be partially responsible for the large h_{crit} values, in contrast to the theory, near $H_0 = H_0^{\text{min}}$.

The increase in h_{crit} with H_0 at field strengths insufficient to saturate the material is clearly evident for the sphere data for $H_0 < 600 \text{ Oe}$ and for the slab data for $H_0 < 1700 \text{ Oe}$. The rod is saturated for $H_0 \approx 0$, so that no corresponding region is evident from the rod data. This behavior of h_{crit} below saturation can be qualitatively understood by considering the parallel and perpendicular pumping data shown in Fig. 38 for spherical samples. As H_0 is reduced below 600 Oe the sample demagnetizes, and the magnetization direction in individual domains is no longer constrained to lie in the applied field direction. This demagnetization results in a reduction in the h_{crit} for perpendicular pumping and an increase in h_{crit} for parallel pumping. The thresholds for the two configurations approach a common value in the limit $H_0 = 0$, corresponding to an isotropically demagnetized material. The break in each of the two curves near $H_0 = 600 \text{ Oe}$ is indicative of the onset of demagnetization processes. The demagnetization is not completely isotropic so there are deviations from the expected convergence at low values of static field as indicated by the data for $H_0 < 200 \text{ Oe}$. The transition between parallel and perpendicular pumping for both saturated and partially magnetized samples is considered further in Appendix II, in conjunction with the oblique pumping study.

As shown in Fig. 37, the relatively short 1 hr anneal at 1000°C had a significant effect on h_{crit} , particularly for the slab data. The rod exhibited a small decrease in h_{crit} after annealing. The results for the sphere are virtually identical before and after the anneal. For the normally magnetized slab, h_{crit} increased after annealing. In all cases, the general shapes of the h_{crit} vs H_0 curves were preserved after annealing. The fact that annealing has a relatively large effect only on the results for the slab indicates that the phenomenon is associated with surface damage or surface strain. Consequently, surface damage during grinding should have the largest effect on the magnetic properties for thin slabs. It should be noticed that the sign of the change upon annealing is not the same for the two sample shapes where the effect is noticeable. Annealing decreases h_{crit} for the axially magnetized rod and increases h_{crit} for the slab. This annealing characteristic may be associated with the specific nature of the surface strain interaction with the magnetization. In the case of the rod, the static field and magnetization are parallel to the sample surface, while for the slab, they are normal to the sample surface.

D. Parallel and Perpendicular Pumping in Thin Disks

In this study of the influence of sample shape on the instability threshold, one possibility for obtaining additional information is to apply the static field in different directions with respect to the sample principal axes. (Rods and disks may be considered to be limiting cases of ellipsoids of revolution.) In spherical samples, however, all directions are equivalent. For rods and disks, on the other hand, parallel and perpendicular pumping can be accomplished for a number of different field arrangements relative to the sample axes. Obtaining data for different field arrangements is equivalent to interchanging the various sample shape demagnetizing factors and, as such, represents a useful technique to further study the effect of sample shape on h_{crit} . The present work was performed on thin 1 cm diam disks for different field orientations as a function of disk thickness and annealing history.

Five different field arrangements are possible if the experiment is restricted to parallel or perpendicular pumping. These arrangements are indicated schematically in Fig. 41. The two top diagrams correspond to parallel pumping with the static external field H_0 parallel to the linearly polarized microwave field h_0 . In one case, both fields are directed normal to the disk. In the other, the fields are parallel to the flat surfaces of the disk (in-plane). The three bottom diagrams correspond to perpendicular pumping. For a normally magnetized disk, only an in-plane microwave field can be used for perpendicular pumping. For an in-plane magnetized disk, h_0 may be normal to the disk or in-plane and still be perpendicular to the static field. A condensed notation will be used in the following discussion to designate the specific configuration under consideration. The symbol $(\perp, \perp, \parallel)$ will indicate $H_0 \perp$ disk, $h_0 \perp$ disk, and $H_0 \parallel h_0$, corresponding to the columnar listing under the upper left diagram. Other configurations are designated in a similar manner.

Data for these five configurations obtained on unannealed 1 cm diam disks are shown in Figs. 42 to 46. The threshold field h_{crit} is displayed as a function of static external field with the disk thickness as a parameter. Experimental results were actually obtained for 10-mil increments in thickness. Data are shown for 20-mil increments in order to simplify the presentation. First consider the results for parallel pumping shown in Figs. 42 and 43. The data for normally magnetized slabs shown in Fig. 42 evidence a decrease in h_{crit} with increasing field, a sharp minimum near 25 Oe and a rapid increase at higher field. The threshold for this configuration also exhibits a strong thickness dependence and h_{crit} is decreased by approximately 1 Oe for each 10-mil increase in thickness. There is no significant change in the field dependence of h_{crit} as the sample demagnetizes for $H_0 < 1700$ Oe. The results shown in Fig. 43 for the other parallel pumping configuration $(\parallel, \parallel, \parallel)$ corresponding to H_0 parallel to the disk plane, h parallel to the disk plane, and H_0 parallel to h_0 are quite different. For this configuration, the minimum h_{crit} occurs for $H_0 = 1100$ Oe and the increase in h_{crit} at higher field is not as sharp as for H_0 normal to the

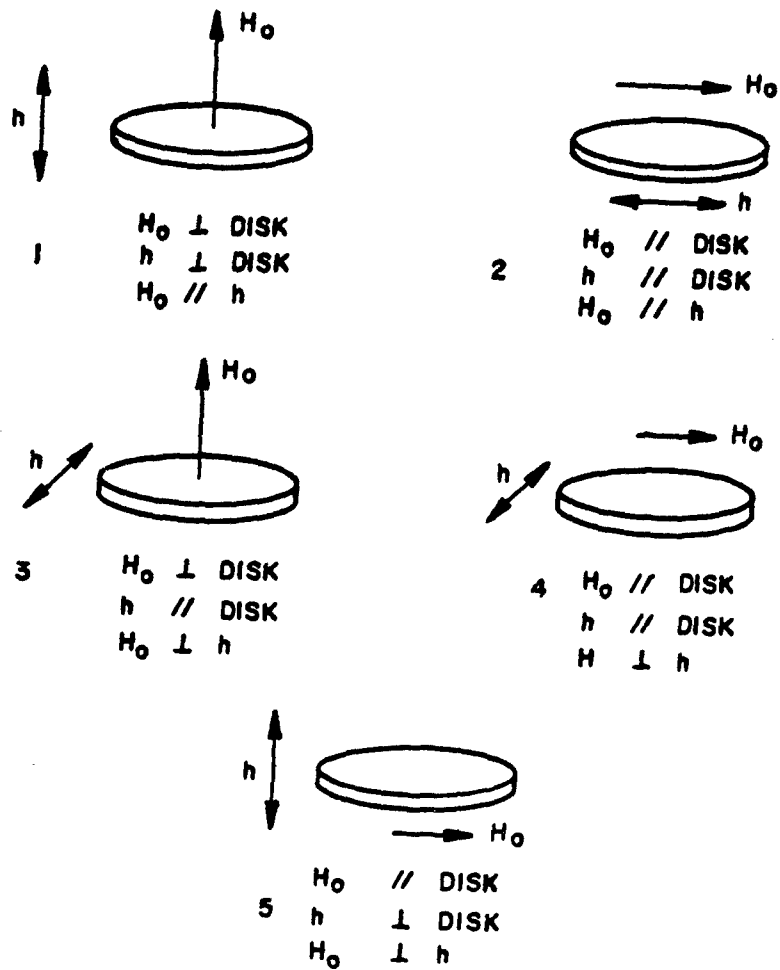


Fig. 41 Summary of the Various Pump Configurations Examined for the Disk-Shaped Samples

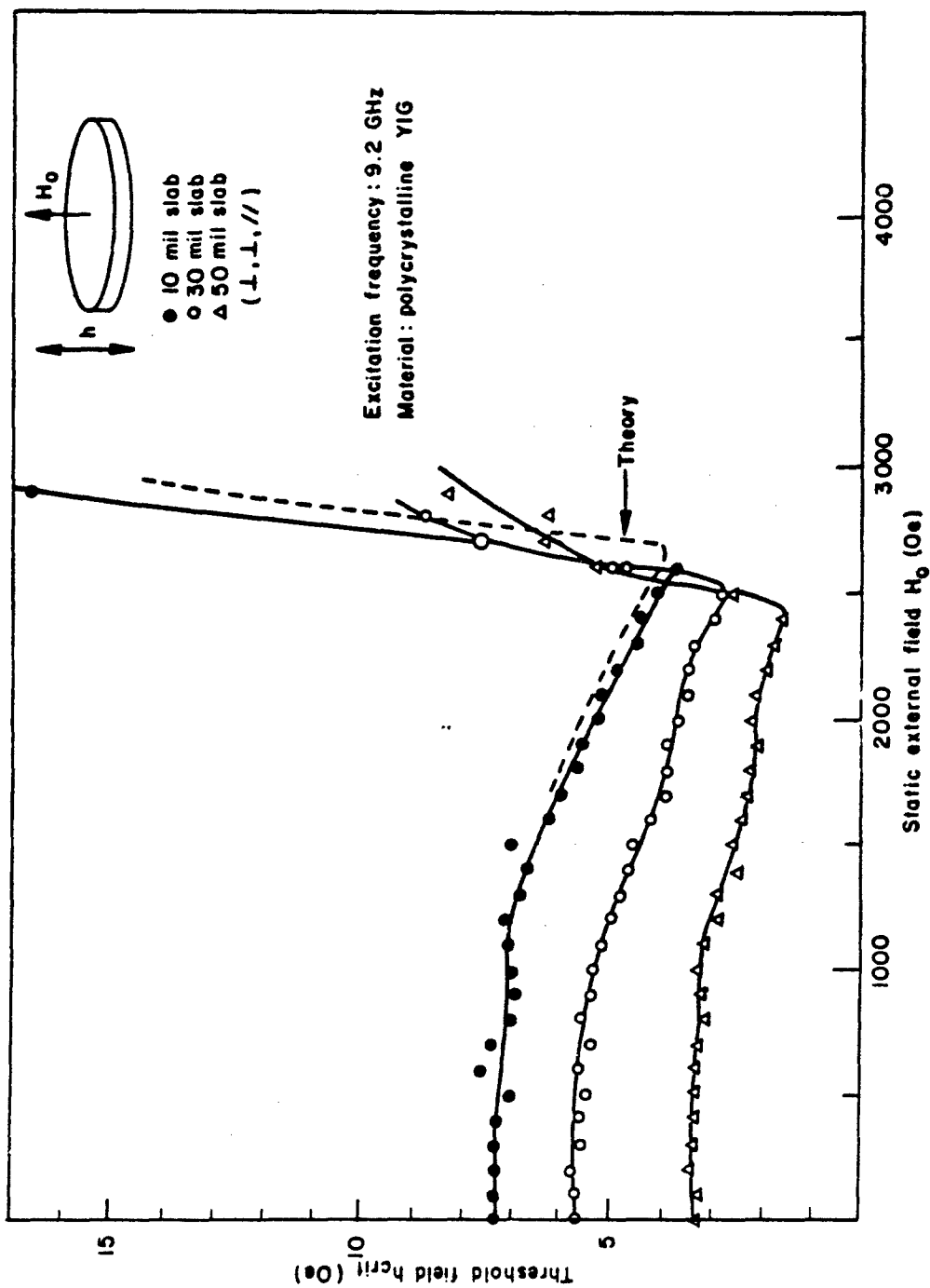


Fig. 42 Threshold Field h_{crit} as a Function of the Static External Field H_0 for the (I, I, //) Configuration. Data for 10-, 30-, and 50-mil thick disks are shown.

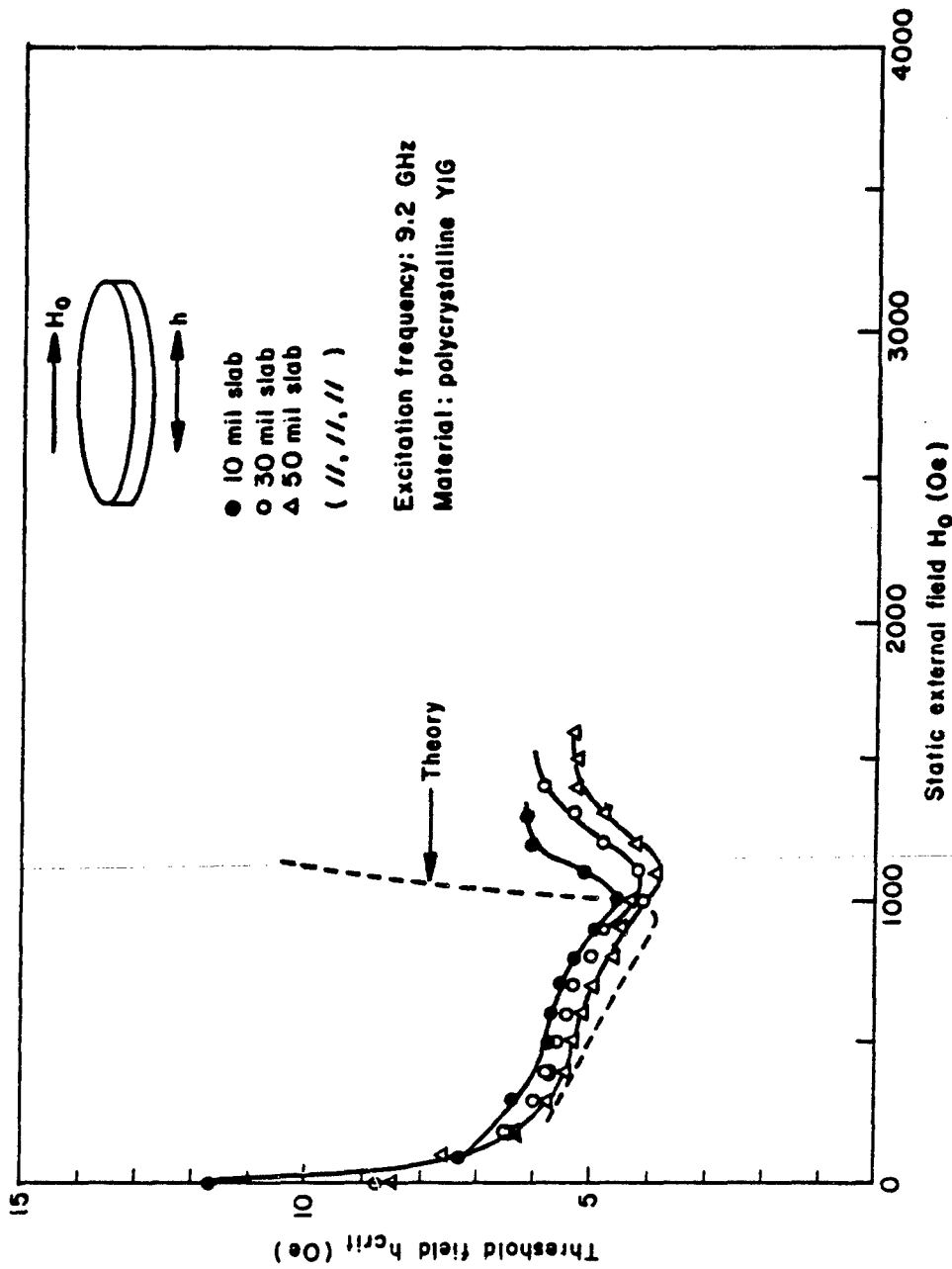


Fig. 43 Threshold Field h_{crit} as a Function of the Static External Field H_0 for the (//, //, //) Configuration. Data for 10-, 30-, and 50-mil thick disks are shown. A single theoretical curve is indicated.

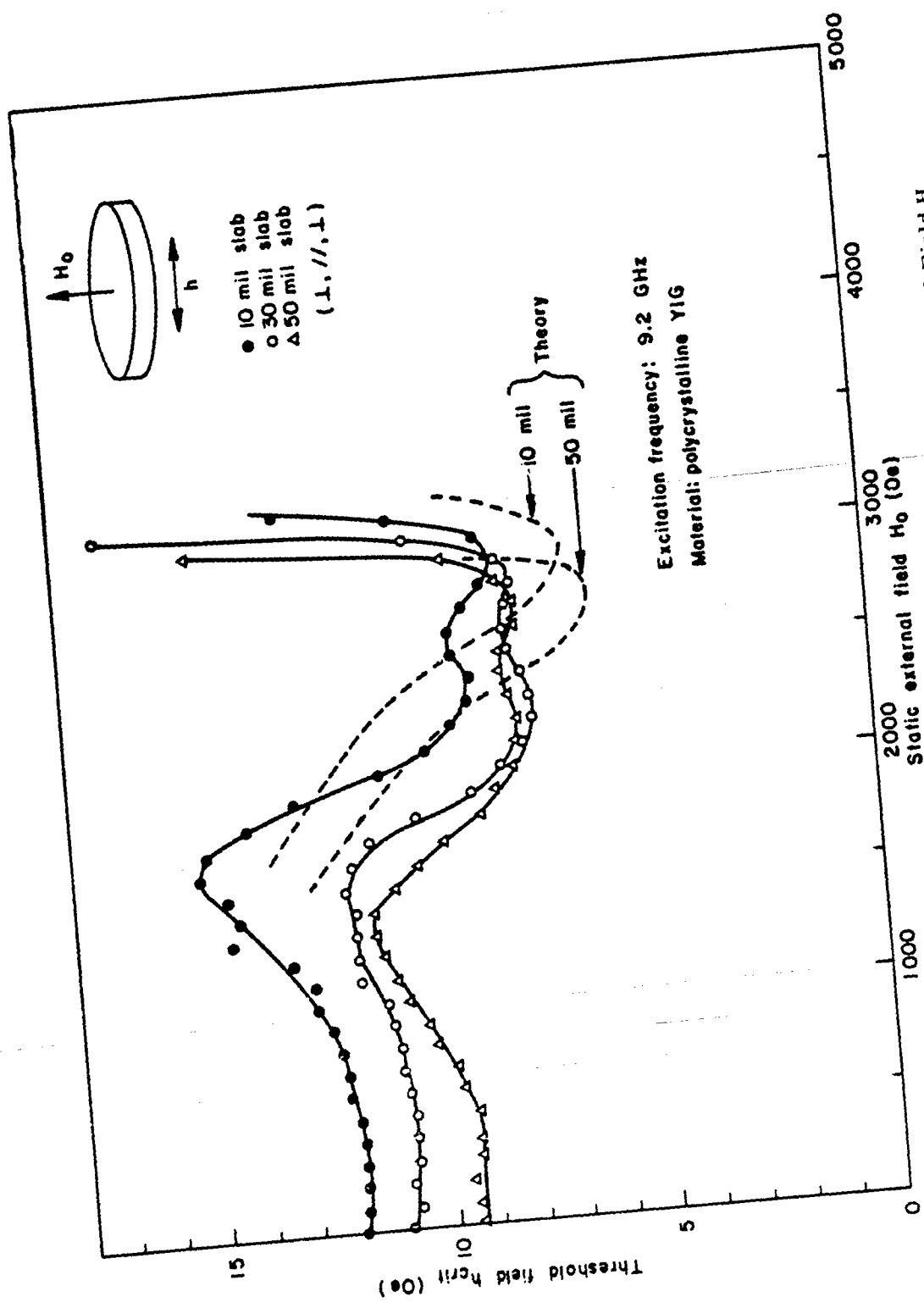


Fig. 44 Threshold Field h_{crit} as a Function of the Static External Field H_0 for the (1, //, 1) Configuration. Data for 10-, 30-, and 50-mil thick disks are shown. Theoretical curves for 10- and 50-mil disks are indicated.

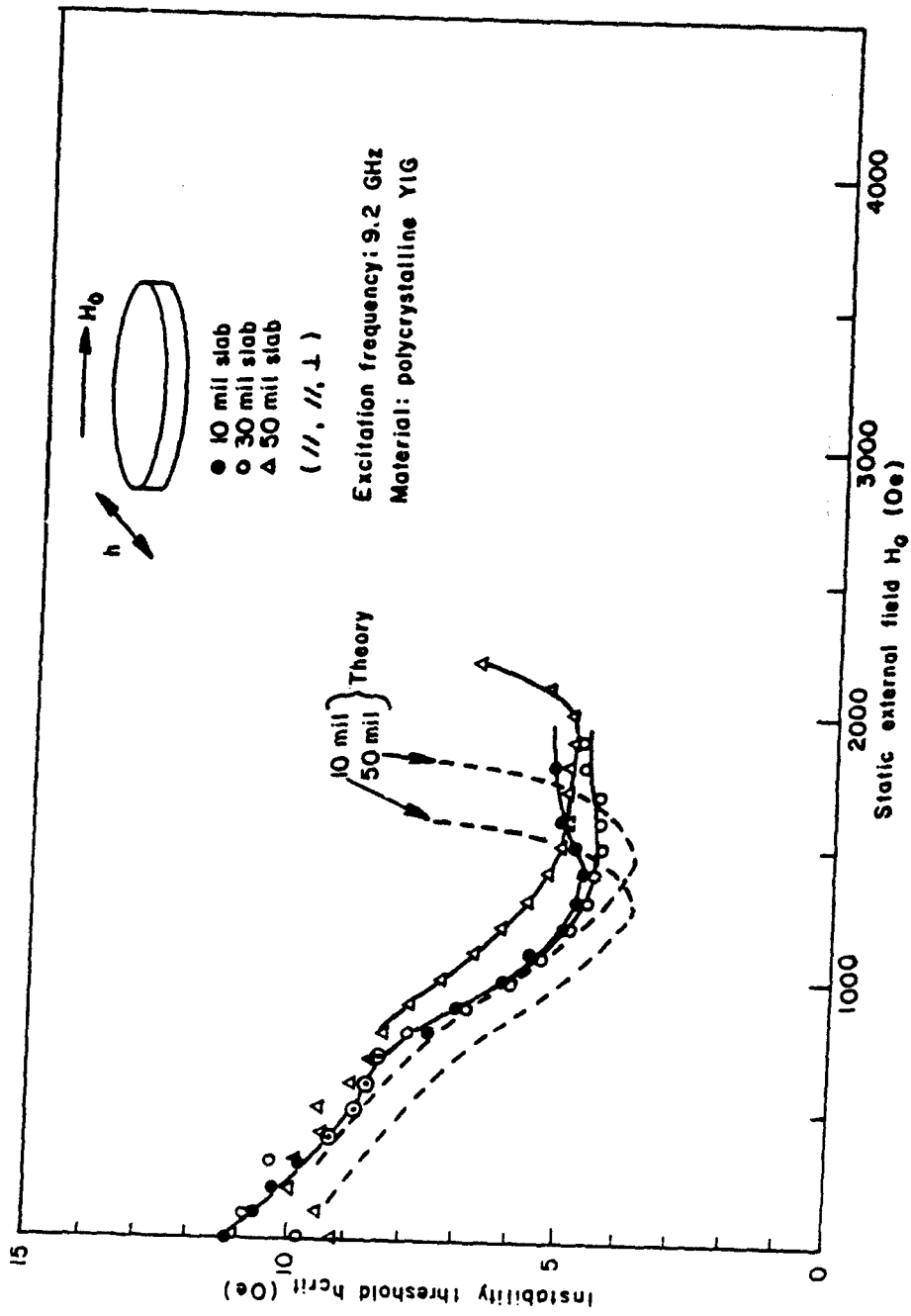


Fig. 45 Threshold field h_{crit} as a function of the Static External Field H_0 for the (//, //, ⊥) Configuration. Data for 10-, 30-, and 50-mil thick disks are shown. Theoretical curves for 10- and 50-mil disks are indicated.

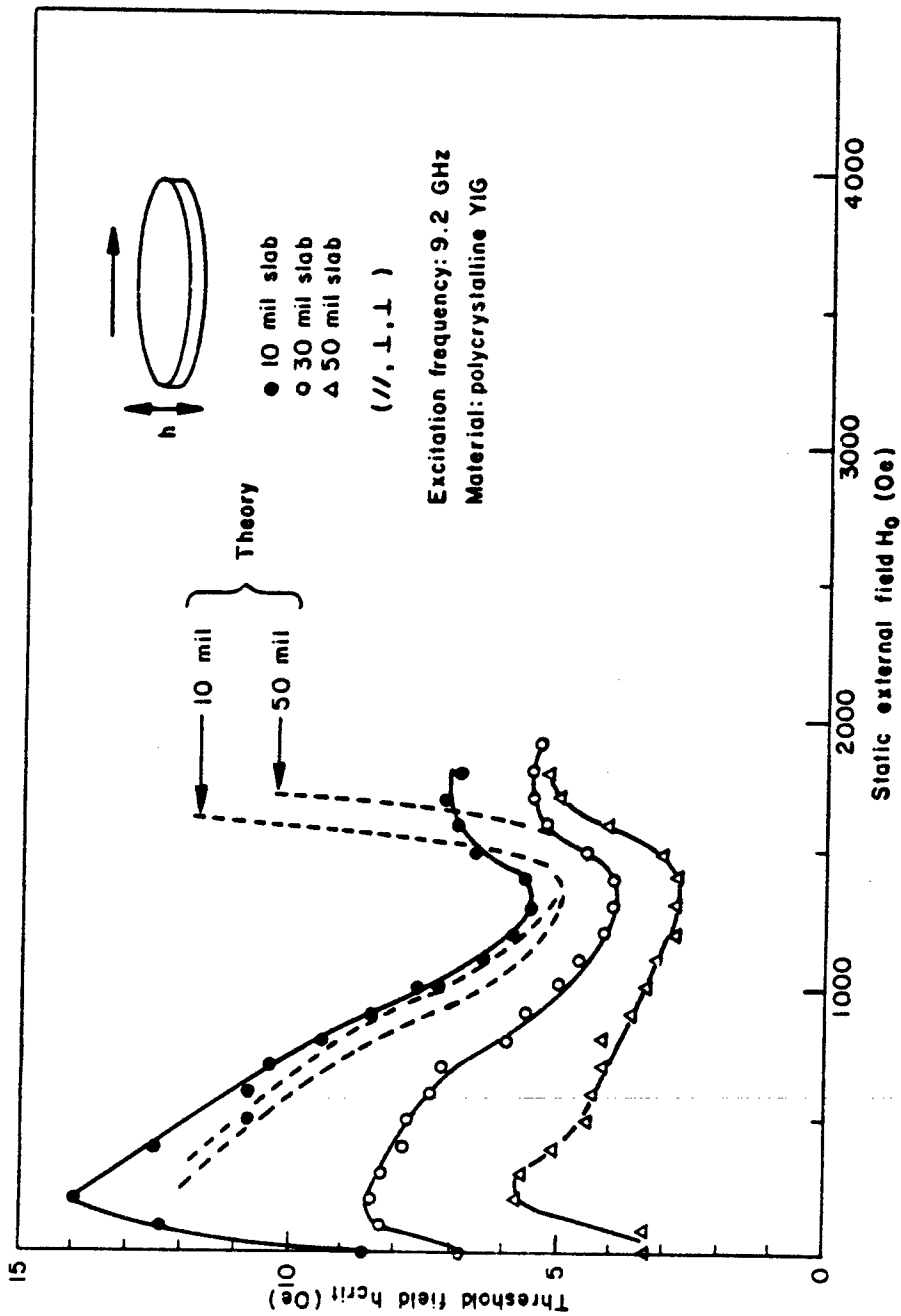


Fig. 46 Threshold Field h_{crit} as a Function of the Static External Field H_0 for the (//, \perp , \perp) Configuration. Data for 10-, 30-, and 50-mil thick disks are shown. Theoretical curves for 10- and 50-mil disks are indicated.

disk. The data exhibit no strong thickness dependence. Furthermore, the h_{crit} values increase sharply as H_0 is reduced below 200 Oe and the samples demagnetize.

Consider the results for the three perpendicular pumping configurations. In Fig. 44 the instability threshold h_{crit} as a function of static field is shown for the $(\perp, \parallel, \perp)$ configuration, with thickness as a parameter. Similar data for the 10-mil disk were shown in Sec. C. The threshold exhibits a broad double minimum and increases sharply at high field. In addition, h_{crit} appears to be a decreasing function of thickness for H_0 below the high-field minimum and an increasing function of thickness above the minimum. As H_0 is reduced below 1700 Oe, demagnetization results in an abrupt decrease in h_{crit} which was discussed in conjunction with Fig. 37. In Fig. 45 data are shown for the $(\parallel, \parallel, \perp)$ pumping configuration. The data exhibit only a broad minimum near 1500 Oe and a small increase at higher field. The threshold for this configuration is not a strong function of sample thickness. Upon demagnetization, furthermore, there is no large change in h_{crit} as found for the $(\parallel, \parallel, \parallel)$ configuration (Fig. 43). For perpendicular pumping with an in-plane static field and an out-of-plane microwave field configuration $(\parallel, \perp, \perp)$ as shown in Fig. 46, h_{crit} has a minimum near 1400 Oe, increases moderately at higher field, and exhibits a strong thickness dependence. As the sample demagnetizes, moreover, h_{crit} decreases sharply, as shown by the experimental points for $H_0 < 200$ Oe. For this $(\parallel, \perp, \perp)$ configuration the change in h_{crit} upon demagnetization is a sensitive function of disk thickness. In Fig. 47, data corresponding to $H_0 < 200$ Oe are shown for different thickness slabs to demonstrate the nature of this dependence. The sharp decrease in h_{crit} begins near $H_0 = 50$ Oe for the 10-mil disk. For the 50-mil thickness, the decrease begins at 120 Oe. Due to the increase in the disk in-plane demagnetizing factor with thickness, thicker disks begin to demagnetize at a larger field than do the thinner disks. Consequently, the field region over which the decrease in h_{crit} occurs broadens with increasing thickness.

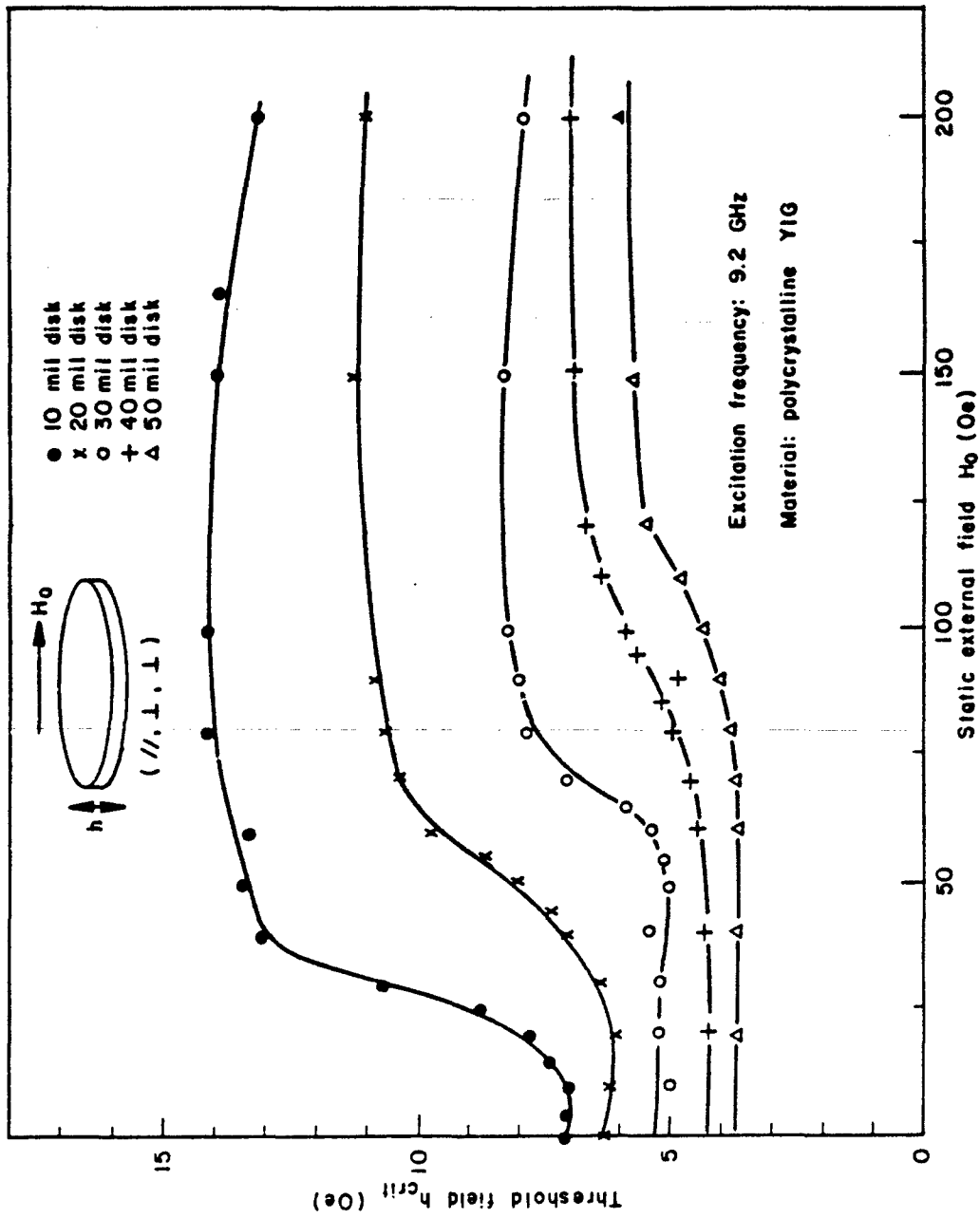


Fig. 47 Threshold field h_{crit} as a function of the Static External Field H_0 for the (//, \perp , \perp) Configuration with Static Field $H_0 < 200$ Oe. Data for 10-, 20-, 30-, 40-, and 50-mil thick disks are shown.

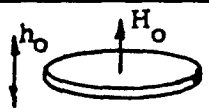
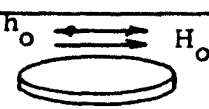
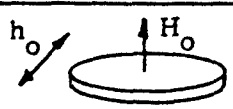
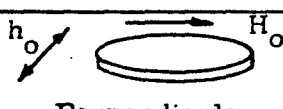

For the particular slab configuration shown in Figs. 37 and 44 (1, ||, 1), annealing increased h_{crit} significantly, particularly in the field region corresponding to a partially magnetized material. Data before and after anneal have also been obtained for the other four field configurations. The only other configuration where annealing had a large effect was perpendicular pumping with the microwave field normal to the plane of the slab, the (||, 1, 1) configuration. Threshold data for two 10-mil disks, one annealed and one unannealed, are shown in Fig. 48. The instability threshold decreases by about 1 Oe after the 1 hr anneal at 1200°C. Thicker disks exhibited smaller decreases, consistent with the earlier conclusions that annealing effects are related to surface damage, and should decrease as the surface-to-volume ratio is decreased. Annealing did influence h_{crit} for the remaining configurations but the change was quite small, on the order of a few tenths of an oersted.

The general characteristics of the results shown in Figs. 42 to 46 are summarized in Table I. The following generalizations can be made: 1) The thickness dependence is significant only when the microwave field is directed normal to the plane of the disk, 2) The minimum h_{crit} position is generally larger for normally magnetized disks than for in-plane magnetized disks, 3) The increase in h_{crit} at high field is sharp only for the normally magnetized disks and h_{crit} increases slowly for in-plane magnetized disks, 4) Large changes in h_{crit} upon demagnetization occur only for disks initially saturated parallel to the disk plane.

In comparing any of the above results with theoretical considerations, dielectric loading effects in the microwave cavity must be taken into account. The two configurations for which the data exhibit a large thickness dependence, the (1, 1, ||) and (||, 1, 1) configurations, the disks are positioned in the TE_{102} microwave cavity with the microwave cavity normal to the disk plane. For these two configurations, portions of the sample are in a region of strong electric field directed parallel to the disk plane and it is expected that dielectric loading might significantly influence the microwave

TABLE I

Summary of Experimental Results for Parallel and Perpendicular Pumping in Thin,
1 cm diam Discs of Polycrystalline YIG at 9.2 GHz

Configuration	Nature of Thickness Dependence	Minimum h_{crit} Position	Nature of High Field Increase	Change in h_{crit} upon Demagnetization
 Parallel Pump (I, I, II)	Large Decrease	2500 Oe	Sharp Increase	No Change
 Parallel Pump (II, II, II)	Small Decrease	1100 Oe	Moderate Increase	Large Increase
 Perpendicular (I, II, I)	Moderate Decrease	2500 Oe (broad)	Sharp Increase	No Change
 Perpendicular (II, II, I)	Negligible	1500 Oe (broad)	Moderate Increase	No Change
 Perpendicular (II, I, II)	Large Decrease	1400 Oe	Moderate Increase	Large Decrease

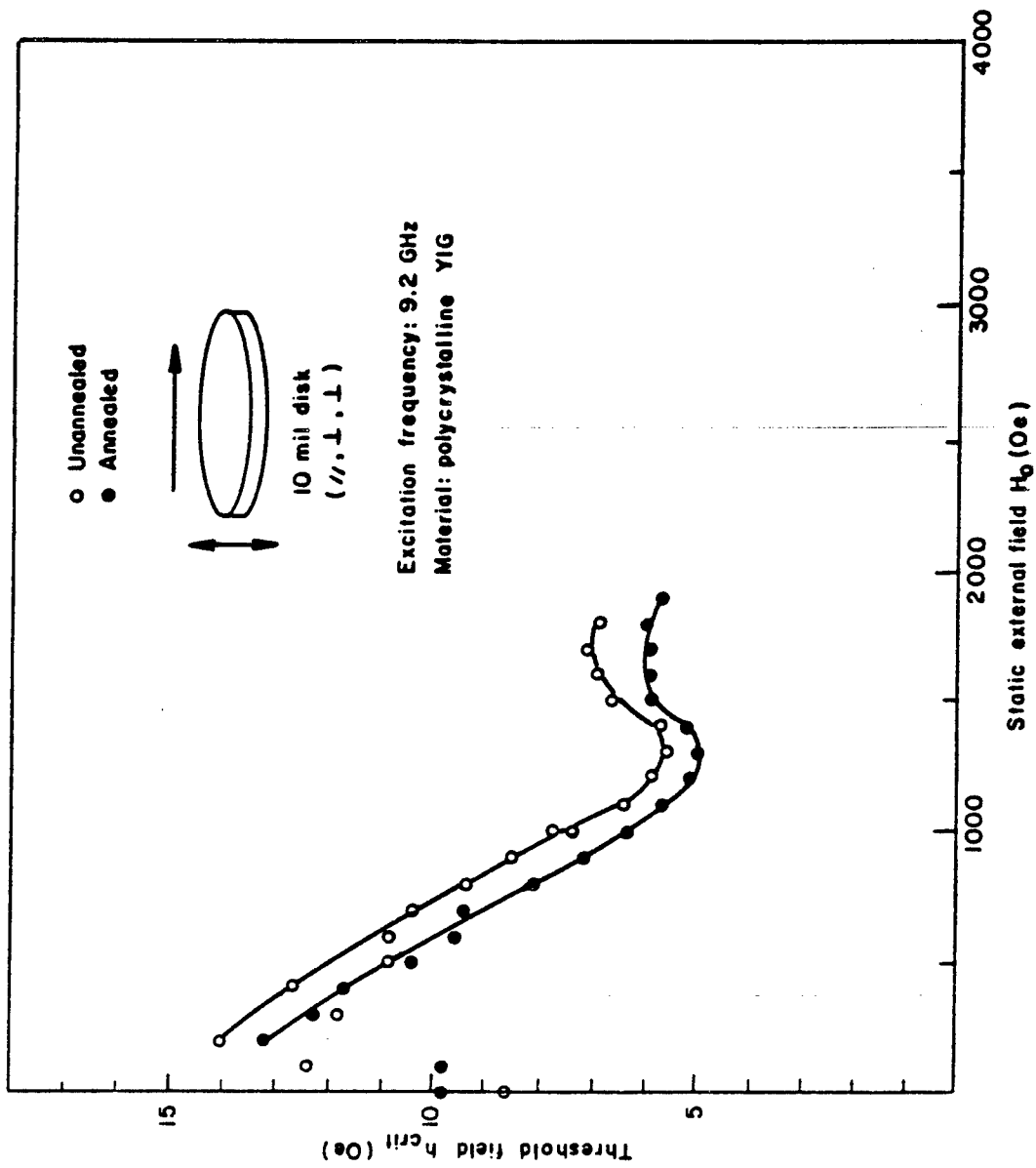


Fig. 48 Threshold Field h_{crit} as a Function of the Static External Field H_0 for a 10-Mil Disk and the (//, ⊥, ⊥) Configuration. Data before and after a 1 hr anneal at 1200°C are shown.

field calibration in terms of the incident power for the cavity. In order to check this possibility, data were obtained for all the configurations discussed above with a 10-mil YIG disk in contact with dielectric disks comparable to YIG in dielectric properties. It was found that thick dielectric disks had the same effect in reducing the apparent h_{crit} for the $(\perp, \perp, \parallel)$ and $(\parallel, \perp, \perp)$ configurations that thick magnetic disks did. For the $(\parallel, \parallel, \parallel)$ and $(\parallel, \parallel, \perp)$ configurations, where the electric field is essentially zero over the sample, the dielectric disks had no effect on the results. For the $(\perp, \parallel, \perp)$ configuration, where the electric field is normal to the disk plane, a small decrease was noted for thick dielectric slabs. On the basis of these results, it appears that dielectric loading of the cavity by the large disk samples is responsible for most of apparent h_{crit} thickness dependence for the $(\perp, \perp, \parallel)$ and $(\parallel, \perp, \perp)$ configurations.

Theoretical curves for comparison with the data were calculated according to the procedure described in Sec. C and are shown as dashed lines in Figs. 42 to 46 for the configurations discussed above. Consider the comparison for the two parallel pumping configurations $(\perp, \perp, \parallel)$ and $(\parallel, \parallel, \perp)$, in Figs. 42 and 43. In each figure only one theoretical curve is plotted. For parallel pumping, the coupling which leads to instability is directly between the microwave pump field and the spinwave which goes unstable. This coupling is independent of disk thickness. Therefore h_{crit} is not expected to be thickness dependent, except for a small shift of the curve to higher field with increasing thickness because of the reduced demagnetizing factor normal to the disk. For the $(\perp, \perp, \parallel)$ configuration and the data in Fig. 42, the observed thickness dependence is due to dielectric loading as discussed above, since the microwave field is normal to the disk. For the thinnest disk, where such loading effects are less important, the agreement is quite good. For the other parallel pump configuration $(\parallel, \parallel, \perp)$, the theoretical curve is the same as in Fig. 42, except it is shifted to lower field by $4\pi M$ to account for the decrease in the internal demagnetizing field. At fields below the minimum h_{crit} position H_0^{min} , the theoretical curve agrees quite well with the data. Above this minimum, however, the experimental h_{crit} does not increase as rapidly as the theoretical curve. The

slow rise in h_{crit} at $H_0 > H_0^{\text{min}}$ is a common feature of the threshold for all the in-plane magnetized disk configurations. It may be explained as one or both of the following: 1) Magnetostatic mode resonances which occur at fields above the uniform resonance position for disks magnetized in their plane, 2) Incorrect estimates of ΔH_k vs θ_k for $k = 0$. It is important to realize that this portion of the curves is not amenable to meaningful theoretical interpretation because the theory is not strictly applicable for $k = 0$, as discussed in Sec. C.

Now consider the disk results for perpendicular pumping summarized in Figs. 44 - 46. In these figures, theoretical curves are also indicated by dotted lines. For perpendicular pumping, however, h_{crit} depends on the uniform precession amplitude which is influenced by the sample shape. Therefore, the threshold field should exhibit a dependence on disk thickness which is related to the efficiency with which the microwave field excites the uniform precession. First consider the data for the normally magnetized disk configuration (1, 1, 1) in Fig. 44. Two theoretical curves are shown. The upper curve was evaluated for 10-mil slab thickness and the lower curve for 50-mil slab thickness. The results for the 10-mil slab were discussed in Sec. C. The theoretical thickness can be understood by considering the uniform precession amplitude dependence on sample shape. When the sample does not possess rotational symmetry about the static field direction as was the case for the data in Sec. C, the uniform precession amplitude is given by

$$a_0 = \frac{h_0(\omega + Y)}{XY - \omega^2} e^{i\omega t} \quad (21)$$

if the contribution of the anti-Larmor component of the linearly polarized microwave field is neglected. The uniform precession amplitude is discussed in detail in Appendix I. In Eq. (21),

$$X = \gamma [H_0 + (N_x - N_z) 4\pi M_s] \quad (22a)$$

and

$$Y = \gamma [H_0 + (N_y - N_z) 4\pi M_s] \quad (22b)$$

where N_x and N_y are the two transverse demagnetizing factors, N_z is the demagnetizing factor in the static field direction, and the microwave field is in the x-direction. For the (1, ||, 1) configuration, Fig. 44, with the y-direction in the plane of the disk and the x-direction normal to the disk, N_x increases and N_z decreases with increasing thickness so that Y and α_0 also increase. With increasing thickness, therefore, the efficiency with which the microwave field pumps the uniform precession increases and the threshold field decreases. The two theoretical curves in Fig. 44 express the above considerations quantitatively. The shift of the h_{crit} minimum to lower field is due to the reduction in the static internal field as N_z decreases. The experimental h_{crit} decreases with thickness for $H_0 < H_0^{min}$ and the minimum h_{crit} position shifts to lower field with increasing thickness, in agreement with theory. Other features of the (1, ||, 1) data were discussed in Sec. C.

The data in Fig. 45 for the (||, ||, 1) configuration (H_0 and h_0 both parallel to the disk plane) indicate that for this configuration, h_{crit} is an increasing function of thickness. The theoretical h_{crit} also increases with thickness. For this configuration, the y-direction is normal to the disk and, consequently, N_y , Y , and α_0 decrease with increasing thickness, so that h_{crit} is expected to increase. As mentioned above, the increase in h_{crit} at static fields above the minimum is not as rapid as expected theoretically. Below the minimum, however, the agreement between the theory and the data is quite good. Finally consider the results for the (||, 1, 1) configuration shown in Fig. 46 where H_0 is parallel to the disk plane and h_0 is normal to the disk. For this configuration, the data for the 10-mil slab are in good agreement with the theory except for the slow increase for $H_0 > H_0^{min}$. The data, however, exhibit a strong decrease in h_{crit} with increasing thickness which is related to dielectric loading since h_0 is normal to the disk plane. No strong dependence is expected theoretically. The y-direction is in the plane of the disk (normal to H_0 and h_0) and H_0 is also in the disk plane. N_y and N_z are equal and

$$\omega + Y = \omega + \gamma H_0 \quad (23)$$

is independent of thickness.

In general, the agreement between the theory and data for all these configurations is quite good, when the theory is applicable. As pointed out, dielectric loading, magnetostatic mode resonances, and the possible errors introduced by applying the theory for $H_0 > H_0^{\min}$ modify the experimental results for some configurations.

The above discussion has been concerned exclusively with the results, experimental and theoretical, for saturated systems. It has been shown that threshold field data for a large variety of situations can be explained on the basis of spinwave instability theory. In order to apply any of these results to partially magnetized systems, however, it is necessary to establish a connection between domain structure and the threshold fields. Such a connection is the subject of the remainder of this section. In the absence of any quantitative description of the domain structure, the treatment will be primarily qualitative. The discussion will be based in part on the oblique pumping presented in Appendix II and primarily on the experimental results for thin disks. In that appendix, it is shown that the data for partially magnetized spherical samples can be explained if for the transverse demagnetizing factor N_t it is assumed that $1/3 < N_t < 1/2$ rather than taking $N_t = 1/3$ as is the case for saturated spherical samples. On the basis of this observation, it may be assumed that the demagnetization is accomplished by the formation of elongated domains which satisfy $1/3 < N_t < 1/2$, and that the shape of these domains influence h_{crit} in much the same way that sample shape does for saturated samples.

Domain structure considerations may also be invoked to account for the threshold field behavior below saturation for the thin-disk results summarized in Figs. 42 to 46. First consider the results in Fig. 42 for parallel pumping with H_0 normal to the plane of the disk, the (1, 1, ||) configuration. The disk begins to demagnetize for $H_0 \approx 4\pi M_s$ or approximately

1750 Oe. At higher field, the magnetization is oriented normal to the disk and parallel to the microwave field by the static field H_0 . For $H_0 \leq 1750$ Oe, the internal field is essentially zero and domains form as demagnetization processes act to minimize the free energy of the sample. As is evident from Fig. 12, h_{crit} for the (1, 1, ||) configuration does not exhibit any sharp changes during demagnetization, but increases gradually to approximately 7 Oe at $H_0 = 0$ (for the 10-mil disk), generally following the curve for the data above saturation. This smooth dependence indicates that the magnetization direction with respect to the microwave field polarization direction does not undergo any major reorientation upon demagnetization. It may be concluded, therefore, that in the partially magnetized or demagnetized material the domains are aligned in directions which are approximately parallel to the disk normal. Such a model has been proposed by Kittel.¹⁶ For thick slabs, interior domains are expected to be aligned along the normal direction and small closure domains are expected to form at the sample surface with magnetization directions parallel to the slab plane. These closure surface domains represent only a small part of the sample volume and do not appreciably influence h_{crit} . Admittedly, this model is a gross oversimplification for polycrystalline YIG material which is cut into thin disks by mechanical means, and which clearly has considerable surface damage and interior defects. Nevertheless, such a model provides an approximate working basis for a consistent interpretation of the results.

For parallel pumping with H_0 parallel to the film plane, the data in Fig. 43 follow the theory for saturated samples down to $H_0 = 200$ Oe. At lower fields the sample presumably demagnetizes with interior domains oriented along the disk normal. At $H_0 = 0$, therefore, the sample consists of elongated domains with the microwave field perpendicular to the domain axis. In terms of shape, this configuration is similar to perpendicular pumping in an axially magnetized rod with $H_0 \approx 0$. The rod data in Fig. 37 indicates that the h_{crit} for this situation should be about 12 Oe, a value which agrees quite well with the disk value of $h_{crit} = 11.8$ Oe at $H_0 = 0$ in Fig. 43. Thus, the simple domain model assumed above is consistent with both sets of parallel pumping data.

This simple domain model is also applicable to the perpendicular pumping configurations for the disk samples. The data for H_0 perpendicular to the disk plane in Fig. 44 indicate that h_{crit} increases to about 15 Oe for the saturated disk at $H_0 = 1800$ Oe where the internal field is essentially zero, and then decreases to 12 Oe at $H_0 = 0$. The value at $H_0 = 1800$ Oe is consistent with the theory for the saturated disk. The situation at $H_0 = 0$ is much the same as discussed above. The sample consists of elongated domains oriented along the disk normal, the pump configuration corresponds to perpendicular pumping in an axially magnetized rod, and h_{crit} is approximately equal to 12 Oe (10-mil disk). A comparable situation exists for perpendicular pumping where both H_0 and h_0 are parallel to the disk plane, as shown in Fig. 45. The threshold is about 11 Oe at $H_0 = 0$ for the 10-mil disk. The results for H_0 parallel and h_0 normal to the disk plane, shown in Fig. 46, indicate that h_{crit} conforms to theory for $H_0 > 200$ Oe, and decreases sharply to about 8.5 Oe at $H_0 = 0$ for the 10-mil slab. According to the model, $H_0 = 0$ corresponds to parallel pumping with domains oriented normal to the disk and h_{crit} should be equal to the value at $H_0 = 0$ for the (1, 1, ||) configurations. This value is 8.3 Oe, so that the agreement here is quite satisfactory.

The above discussion clearly demonstrates the influence of domain structure on the threshold fields for partially magnetized magnetic materials. A qualitative connection was evident from the oblique pumping results for spherical samples in Appendix II. A more quantitative connection is evident from the results for parallel and perpendicular pumping in disks. A simple domain model for the demagnetized disks is found to provide a consistent explanation of the experimental results below saturation.

E. Larmor and Anti-Larmor Pumping in Rod Samples

The previous two sections have been concerned with the influence of sample shape and orientation on the high-power thresholds for parallel or perpendicular pumping. For all the data reported above, linearly polarized microwave excitation was used. Because of the complex domain structure

associated with most partially magnetized systems, the actual pumping environment is likely to be more complicated. In order to obtain some insight into the effect on the threshold of changes in the pump configuration, two experiments have been performed: 1) The oblique pumping study of Appendix II, 2) Perpendicular pumping with circularly polarized microwave fields rotating in a Larmor sense, the proper sense to excite ferromagnetic resonance, and in an anti-Larmor sense, the opposite sense. This section is concerned with the Larmor and anti-Larmor pumping results. Instability threshold data were obtained for axially magnetized, partially magnetized, and demagnetized 10-mil diam rods of polycrystalline YIG material as a function of external field, average magnetization, and polarization sense for the circularly polarized microwave field normal to the rod axis. The results were obtained at 5.5 GHz and room temperature.

The transition between Larmor and anti-Larmor pumping was accomplished by exciting the sample with one sense of circularly polarized drive and varying the static axial field from a large positive value to a large negative value. The effective sense of polarization changes when the field direction changes, because this changes the natural precession sense. The situation is complicated by the presence of magnetic hysteresis. By traversing the hysteresis loop in both directions, i. e., from a large positive field to a large negative field and then back again, data can be obtained for both Larmor and anti-Larmor pumping and for the two average magnetization values which correspond to a given field. In Fig. 49, the threshold field, relative to the minimum value near zero external field, is shown as a function of external field from -20 to +100 Oe. The data show that for $H_0 > 0$ the threshold is considerably lower than for $H_0 < 0$. A Larmor rotating pump field is much more efficient in exciting the uniform precession and should lead to a lower instability threshold. The data for $H_0 > 0$ and a low threshold therefore correspond to Larmor pumping and the results for $H_0 < 0$ to anti-Larmor pumping. Hysteresis is also evident in the data. Values of h_{crit} measured with increasing H_0 are different from those obtained with decreasing H_0 . Additional data are shown in Fig. 50, with an expanded horizontal scale in order to exhibit more

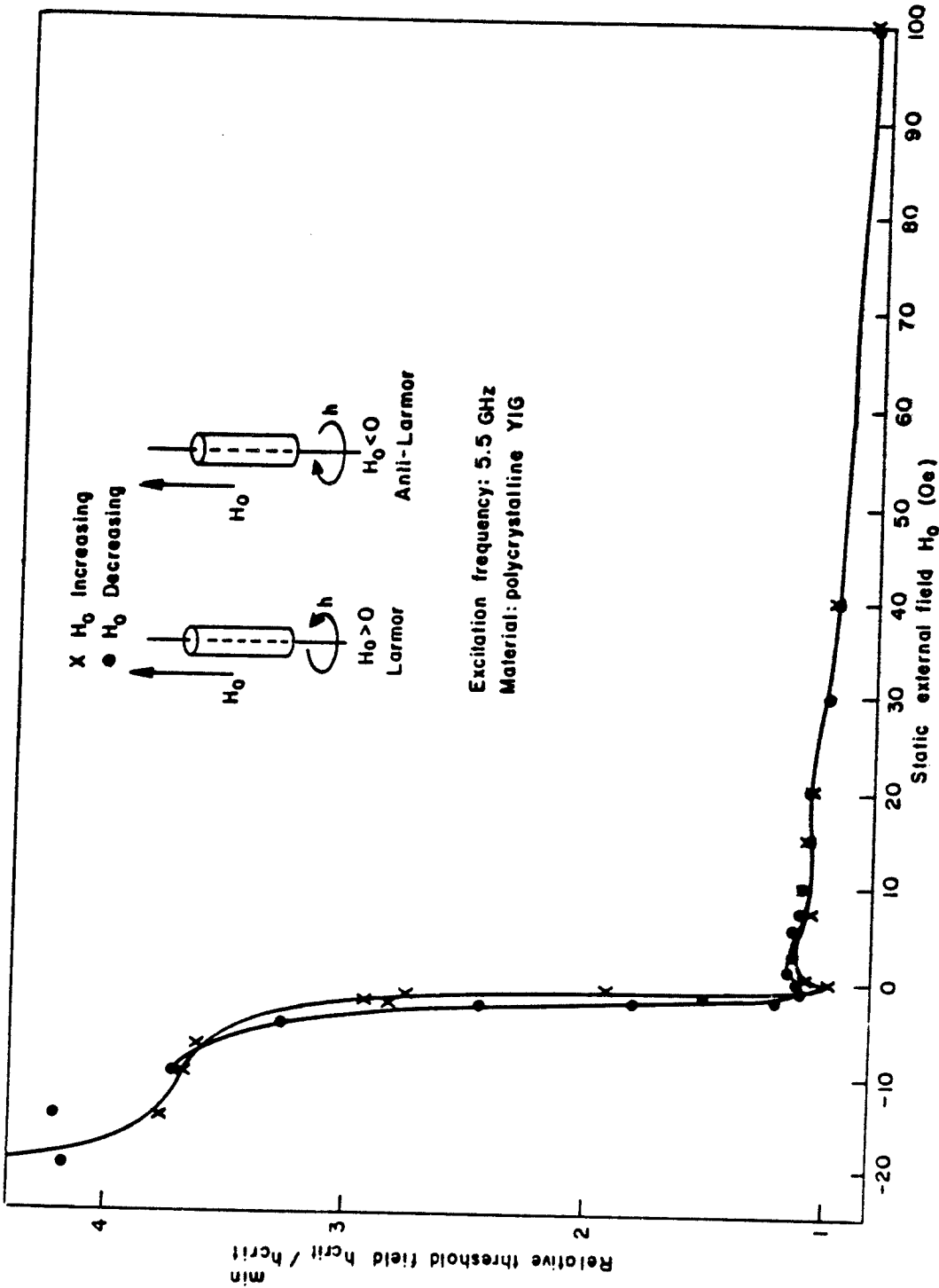


Fig. 49 The Threshold Field, Relative to the Value at $H_0 = 0$ with H_0 Increasing, as a Function of Static External Field for 75-Mil Diam Rods and Circularly Polarized Perpendicular Pump Excitation.

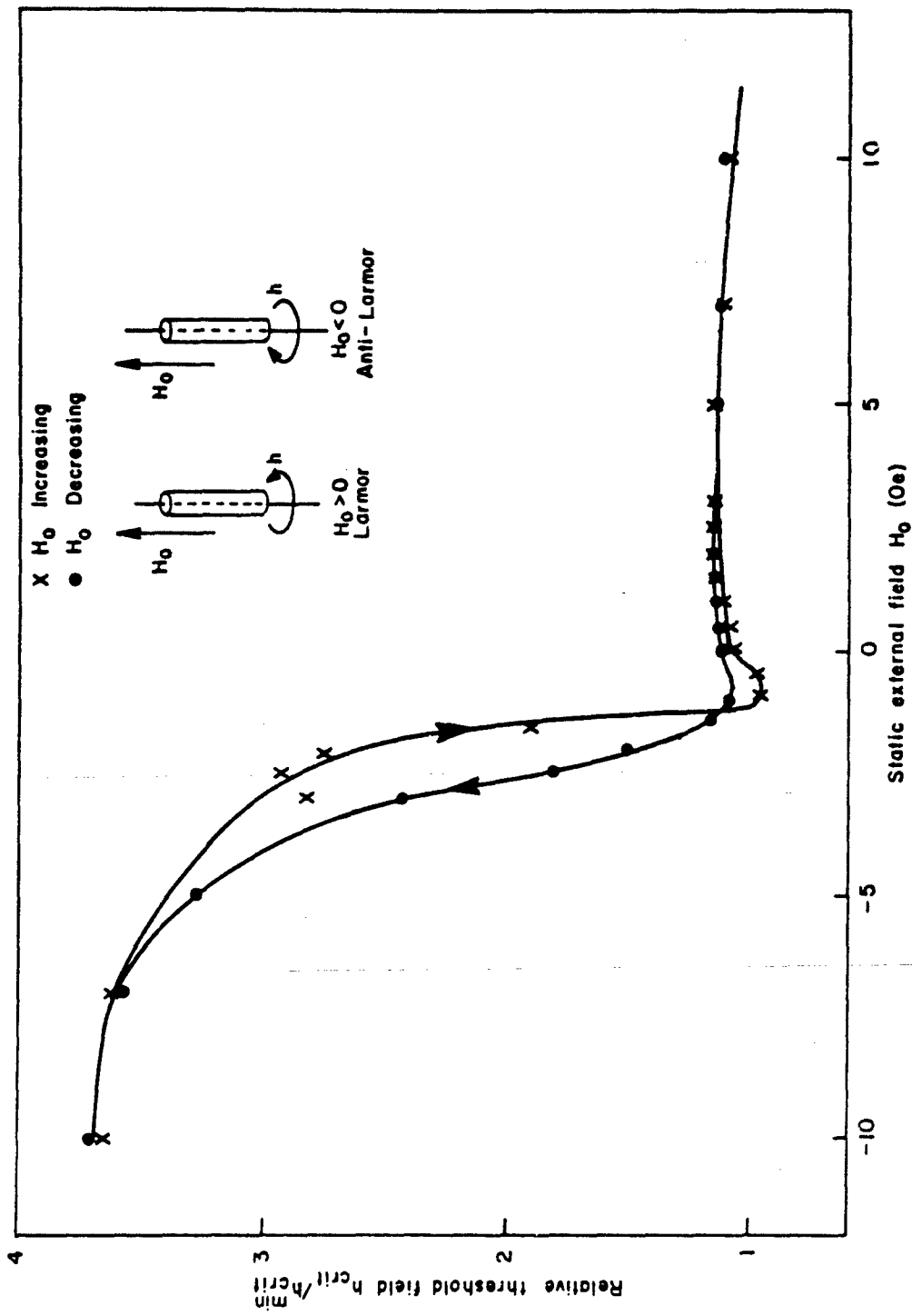


Fig. 50 The Threshold Field, Relative to the Value at $H_0 = 0$ with H_0 Increasing, as a Function of Static External Field Circularly Polarized Perpendicular Pump Excitation. The horizontal scale is expanded from that shown in Fig. 49.

clearly the nature of the hysteresis in h_{crit} . For these data H_0 was cycled between +100 and -30 Oe. For negative H_0 corresponding to anti-Larmor pumping, the threshold field is much larger for increasing H_0 than for decreasing H_0 . For positive H_0 and Larmor pumping, on the other hand, the threshold is larger for increasing H_0 than for decreasing H_0 . This hysteresis in h_{crit} is due to the different domain distributions which are possible for the same static field.

The applicability of the theory to these pump configurations can be determined by comparing the ratio of the threshold for a large negative static field (anti-Larmor threshold) to the threshold for a large positive field (Larmor threshold) with the theoretical value, choosing the static field values so that the material is magnetized to near saturation. Theoretical values were obtained from the theory presented in Appendix. I. From Fig. 49, the ratio between h_{crit} at -20 and +100 Oe is equal to 4.7. The theoretical ratio is equal to 14.0 when measured values of the average $4\pi M$ at each field are used in the theory. At -20 Oe, $4\pi M$ is -1594 G and at +100 Oe, $4\pi M$ is near the saturation value of 1750 G. The agreement is poor. The large discrepancy which does exist is probably due to the non-saturated condition of the rod at $H_0 = -20$ Oe. The partial misalignment of domains gives rise to stray fields, which lead to Larmor coupling even for a microwave field rotating in an anti-Larmor sense. The -20 Oe value was the largest attainable static field in the reverse direction for the electromagnet. Data at higher static fields should result in improved agreement.

IV. SUMMARY AND CONCLUSIONS

Measurements of μ' , κ' , μ_z' , μ'' , κ'' , and μ_z'' have been made on several materials. We have found that Rado's theory on the permeability of partially magnetized ferrites gives approximately the correct value for κ' . Some deviations were observed, however, the most significant of these being that for some materials κ' is not a unique function of $4\pi M$ but depends on the hysteresis history of the sample. Rado's theory does not give the correct results for μ_z' and μ' . We have shown how the rf demagnetizing fields from poles on grain and domain boundaries produce terms which Rado ignored in his theory and which contribute primarily to μ' and μ_z' . Empirical formulae for μ' and μ_z' which fit our data have been presented. The results of the measurement of μ'' , κ'' , and μ_z'' vs $4\pi M$ for various values of ω_M/ω have been presented in the figures. At values of ω_M/ω close to 1.0 their dependence on $4\pi M$ is substantial. At values of $\omega_M/\omega \leq 0.8$ this dependence is small. Furthermore, κ'' is then much less than μ'' . In this region we feel a single loss parameter, μ'' at $4\pi M = 0$, is adequate to characterize the material. The results of measurements of this single parameter on several very low-loss materials at various frequencies in this region were presented.

The investigation of high-power phenomena has accomplished the following objectives: 1) A general theory has been developed for first-order instability threshold fields in ellipsoidal samples magnetized to saturation along a principal axis and with an arbitrary microwave field configuration, 2) The effect of sample shape and pump configuration on threshold for saturated systems has been characterized and explained in terms of the theory, 3) A connection has been observed between the domain structure and the threshold fields for partially magnetized systems which indicates that domain shape plays the same role in determining the threshold for multidomain systems that sample shape plays for saturated systems.

The experimental data were obtained by using a semiautomated instrumentation system which enables h_{crit} determinations to be made

accurately and quickly, thereby facilitating the accumulation of a large amount of data as a function of sample shape, pump configuration, static field, and magnetization state. Perpendicular pump data for axially magnetized rods, spheres, and normally magnetized slabs indicate that gross changes in sample shape have a large influence on h_{crit} and that annealing also changes h_{crit} for samples with large surface-area-to-volume ratios. For the normally magnetized disks, the presence of magnetostatic mode resonances in the resonance spectra modifies the threshold field from the theoretical value. Apart from modifications due to annealing and magnetostatic mode phenomena, the data are consistent with theory and indicate that the theory is applicable for a variety of sample shapes. Parallel and perpendicular pump data for disk-shaped samples have been obtained which are also consistent with theory. For configurations with the microwave field normal to the disk, dielectric loading in the microwave cavity must be taken into account. Additional results for perpendicular pumping in rod-shaped samples with circularly polarized excitation indicate that the threshold is much higher for anti-Larmor than for Larmor pumping, and the increase is slightly less than expected theoretically.

The results for partially magnetized samples in the configurations summarized above indicate that the theory is applicable to these multi-domain systems, if domain shape is taken into account. The data for spherical samples are consistent with theory, if the samples are assumed to demagnetize by the formation of elongated domains along the static-field direction. Similarly, the disk data can be explained if a domain structure consisting of rod-shaped domains normal to the disk plane are assumed. Although such domain models represent a gross oversimplification of the demagnetization processes involved, they are qualitatively correct. The consistent correlations between the data and the theory, which are made possible by these models, provide convincing evidence that domain shape for partially magnetized samples and sample shape for saturated systems are directly applicable to partially magnetized materials, if reasonable assumptions concerning the domain structure can be made. On this basis, predictions of peak power capability for materials and geometries relevant to remanent devices should be possible.

V. REFERENCES

1. W. J. Ince and E. Stern, IEEE Trans. MTT-15, 87 (1967).
2. R. C. LeCraw and E. G. Spencer, IRE Convention Record, Part V, 66 (1956).
3. T. Kohane and E. Schlömann, J. Appl. Phys. 39, 720 (1968).
4. D. Polder and J. Smit, Rev. Mod. Phys. 25, 89 (1953).
5. G. Rado, Phys. Rev. 89, 529 (1953), IRE Trans. AD-4, 512 (1956).
6. R. F. Soohoo, IRE Convention Record, Part V, 84 (1956).
7. J. L. Allen, "The Analysis of Dielectric Loaded Ferrite Phase Shifters Including the Effects of Losses," Ph. D. Thesis, Georgia Institute of Technology (1966).
8. F. Sandy and J. J. Green, J. Appl. Phys. 38, 1413 (1967).
9. H. E. Bussey and L. A. Steinert, IRE Trans. MTT-6, 73 (1958).
10. R. C. LeCraw and E. G. Spencer, J. Appl. Phys. 28, 399 (1957).
11. T. Kohane and E. Schlömann, J. Appl. Phys. 37, 1073 (1966).
12. E. Schlömann, J. Appl. Phys. 38, 5035 (1967).
13. R. I. Joseph and E. Schlömann, J. Appl. Phys. 38, 1915 (1967).
14. H. Suhl, J. Phys. Chem. Solids 1, 209 (1957).
15. See E. Schlömann, J. J. Green, and U. Milano, J. Appl. Phys. 31, 380S (1960).
16. C. Kittel, Phys. Rev. 70, 965 (1940).
17. T. Kohane, SCP and Solid State Technology 7, 46 (1964).
18. E. Schlömann and R. I. Joseph, J. Appl. Phys. 32, 165S (1961).

APPENDIX I

THEORY FOR THE FIRST-ORDER SPIN-WAVE INSTABILITY THRESHOLD IN FERROMAGNETIC INSULATORS OF ELLIPSOIDAL SHAPE WITH AN ARBITRARY PUMPING CONFIGURATION*

Carl E. Patton
Raytheon Research Division
Waltham, Massachusetts 02154

ABSTRACT

The spin-wave instability theory of nonlinear effects in ferromagnetic insulators developed by Suhl for perpendicular pumping and by Schlömann for parallel pumping has been extended to include pumping with an arbitrary microwave configuration. The theory is applicable to samples of ellipsoidal shape, magnetized to saturation along one principal axis, but not necessarily an axis of rotational symmetry as in the Suhl theory. The theory, in its present form, is quite versatile and applicable to a large variety of situations which are not accessible on the basis of the earlier calculations.

Equations are developed specifically for first-order processes. Several examples are considered to demonstrate the versatility of the theory:

- 1) Perpendicular pumping with a linearly polarized microwave field;
- 2) Oblique pumping with a linearly polarized field at an angle between zero and 90° to the static field;
- 3) Perpendicular pumping with a circularly polarized field rotating in the anti-Larmor sense.

INTRODUCTION

Although the spin-wave instability theory of nonlinear effects in ferromagnetic insulators developed by Suhl¹ and Schlömann et al.² is quite general in concept, the specific calculations were done only for restricted pumping configurations and sample shapes. Pumping configurations were restricted to linearly polarized microwave fields along the static field direction (parallel pumping) or circularly polarized fields perpendicular to the static field direction with the proper sense of rotation to excite ferromagnetic resonance (perpendicular pumping). The results are applicable only to samples of ellipsoidal shape magnetized to saturation along a principal axis. For perpendicular pumping the saturation direction must also be an axis of rotational symmetry. The theory has been extended to include: 1) Samples of ellipsoidal shape magnetized to saturation by an applied static field H_0 along a principal axis, not necessarily an axis of rotational symmetry; 2) An arbitrary configuration for the microwave field. A general expression for the first-order instability threshold field as a function of spin-wave propagation direction, static field, sample shape, and pumping configuration is obtained. Results are presented for several interesting special cases, primarily to illustrate the versatility of the theory in evaluating the instability thresholds for given situations. Three cases are considered: 1) Perpendicular pumping with a linearly polarized microwave excitation; 2) Perpendicular pumping with a circularly polarized microwave field rotating in the anti-Larmor sense (opposite to that required for ferromagnetic resonance), and 3) Pumping with a linearly polarized microwave field at an arbitrary angle to the saturation direction. Similar results for these special cases and an infinite magnetic medium have been reported by Kitaev, et al.³ The special case of oblique pumping has also been examined by Stern⁴ and Green et al.⁵ The present specific results, however, are obtained from a general extension of the original Schlömann-Suhl theory and are easily applicable to more complicated instability calculations.

SPIN-WAVE EQUATION OF MOTION

The equation of motion for the spin-wave amplitude a_k , first obtained by Suhl¹ and discussed by Schlömann,⁶ forms the basis of the present extension of the theory to the general case. The general approach and much of the mathematics closely follow the discussion in Ref. 6. Consider the undamped equation of motion for the magnetization $\underline{M}(\underline{r})$ in terms of a unit vector $\underline{a}(\underline{r}) = \underline{M}(\underline{r})/M$:

$$\frac{d\underline{a}(\underline{r})}{dt} = -\gamma \underline{a}(\underline{r}) \times \underline{H}(\underline{r}) \quad (1)$$

where γ is the gyromagnetic ratio, assumed positive for electrons, $4\pi M$ is the saturation induction, and $\underline{H}(\underline{r})$ is the total internal magnetic field. This internal field consists of four parts, the static external field \underline{H}_0 , the external microwave field \underline{h}_0 , an effective field due to exchange $\underline{H}_{ex}(\underline{r})$, and an effective field due to dipolar interactions $\underline{H}_{dip}(\underline{r})$. All fields except $\underline{H}(\underline{r})$ are assumed to vary as $e^{i\omega t}$ where ω is the angular excitation frequency. By expanding the $\underline{a}(\underline{r})$ in a Fourier series

$$\underline{a}(\underline{r}) = \sum_{\underline{k}} \underline{a}_{\underline{k}} e^{i\underline{k} \cdot \underline{r}} \quad (2)$$

assuming that \underline{H}_0 and \underline{h}_0 are uniform over the sample volume, selecting the coordinate axes to be along the principal axes of the saturated ellipsoidal sample with \underline{H}_0 in the z-direction, and assuming that $M_z \approx M$ is satisfied, the equation of motion for $\underline{a}_{\underline{k}}$ can be obtained. The vector \underline{k} is the propagation constant or wave vector for the spin wave, and the $\underline{a}_{\underline{k}}$ are spin-wave amplitudes defined according to Eq. (2). Following Schlömann,⁶ the external fields may be expressed in terms of internal fields,

$$H = H_0 - 4\pi M N_z \quad (3a)$$

and

$$h_{x,y} = h_0^{x,y} - 4\pi M N_{x,y} a_0^{x,y} \quad (3b)$$

where $4\pi M$ is the saturation induction and $N_{x,y,z}$ are the sample demagnetizing factors. The result can be expressed conveniently in terms of complex variables

$$a_k = a_k^x + i a_k^y \quad ,$$

$$k_T = k_x + i k_y \quad , \quad (4a)$$

and

$$h = h_x + i h_y \quad , \quad (4b)$$

The equation of motion is

$$\begin{aligned} a_k = i\gamma \{ [H + h_0^z + 4\pi M N_z (1 - a_0^z)] a_k - a_k^z h \\ + D \sum_{k'} (k')^2 (a_{k'} a_{k-k'}^z - a_{k'}^z a_{k-k'}) \\ + 4\pi M \sum_{k' \neq 0} (\underline{k}' \cdot \underline{a}_{k'}) (k'_T a_{k-k'}^z - k'_z a_{k-k'}) / (k')^2 \} \quad , \quad (5) \end{aligned}$$

with

$$a_k^z = \delta_{k0} - \frac{1}{Z} \sum_{k'} a_{k'} a_{k-k'}^* \quad , \quad (6)$$

where D is a phenomenological exchange parameter defined by $\underline{H}_{ex}(\underline{r}) = DV^2 a(\underline{r})$ and δ_{k0} is the Kronecker delta function. Equation (5) with $h_0^z = 0$ or $h = 0$ provides the basis for the calculation of perpendicular or parallel pumped instabilities, respectively. The inclusion of both h and h_0^z in the equation of motion for a_k provides the basis for the present extension of the theory to include an arbitrary pumping configuration.

In a conventional low power microwave experiment, only the uniform mode is excited to a large amplitude and the $a_{k'}$, other than for $\underline{k} = 0$, are

negligibly excited. In calculating the instability threshold, therefore, only terms to first-order in the a_k with $k \neq 0$ need be considered. Including only terms linear in the a_k , the equation of motion for a_k with $k \neq 0$ becomes

$$a_k = i [(A_k + C_k) a_k + (B_k e^{2i\phi_k} + D_k) a_{-k}^*] + i \gamma h_0^z a_k \quad (7)$$

where

$$A_k = \gamma H + \gamma D k^2 + \frac{1}{2} \omega_m \sin^2 \theta_k \quad (8a)$$

$$B_k = \frac{1}{2} \omega_m \sin^2 \theta_k \quad (8b)$$

$$C_k = -\frac{1}{2} \omega_m \cos \theta_k \sin \theta_k (e^{-i\phi_k} a_0 + e^{i\phi_k} a_0^*) + \frac{1}{4} \omega_m [2N_z + (3 \cos^2 \theta_k - 1)] |a_0|^2 + \frac{1}{2} \gamma h a_0^* \quad (8c)$$

and

$$D_k = \frac{1}{2} \gamma D k^2 a_0^2 - \omega_m \cos \theta_k \sin \theta_k e^{i\phi_k} a_0 + \frac{1}{4} \omega_m (2 \cos^2 \theta_k a_0^2 - \sin^2 \theta_k e^{2i\phi_k} |a_0|^2) + \frac{1}{2} \gamma h a_0 \quad (8d)$$

in which ω_m is equal to $\gamma 4\pi M$, θ_k is the angle between the spin-wave wave vector \underline{k} and the saturation direction, and ϕ_k is the angle between the projection of \underline{k} on the x-y plane perpendicular to the saturation direction and the x-axis. The A_k and B_k terms are linear in the a_k including $k = 0$ terms, the C_k and D_k terms are linear in the a_k for $k \neq 0$ terms only and include a_0 terms to first or second order, and the h_0^z term results from the microwave field component along the direction of the static external field H_0 . The uniform precession amplitude a_0 is nonzero only for a nonzero microwave field component perpendicular to H_0 . If h_0^x and h_0^y are zero, a_0 is zero, and the C_k and D_k terms vanish. Equation (7) then leads to the instability threshold for parallel pumping calculated by Schlömann.^{2,6} If h_0^z is zero Eq. (7) is the same as obtained in Suhl's perpendicular pumping theory.¹

In the absence of any microwave excitation, only the A_k and B_k are nonzero and the equation of motion can be diagonalized by a linear Holstein-Primakoff transformation

$$b_k = \lambda_k a_k + \mu_k a_{-k}^* \quad , \quad (9)$$

with

$$\lambda_k = \cosh (\psi_k/2) \quad , \quad (10a)$$

and

$$\mu_k = \sinh (\psi_k/2) e^{2i\phi_k} \quad , \quad (10b)$$

where

$$\cosh \psi_k = A_k/\omega_k \quad , \quad (11a)$$

$$\sinh \psi_k = B_k/\omega_k \quad , \quad (11b)$$

and

$$\begin{aligned} \omega_k &= (A_k^2 - B_k^2)^{\frac{1}{2}} \\ &= [(\gamma H + \gamma Dk^2) (\gamma H + \gamma Dk^2 + \omega_m \sin^2 \theta_k)]^{\frac{1}{2}} \quad . \end{aligned} \quad (11c)$$

Expressed in terms of the b_k , the equation of motion becomes

$$\begin{aligned} \dot{b}_k &= i \{ \omega_k b_k + (F_k + \gamma h_0^2 A_k/\omega_k) b_k \\ &\quad + (G_k - \gamma h_0^2 B_k e^{2i\phi_k/\omega_k}) b_k^* \} \quad . \end{aligned} \quad (12)$$

The F_k and G_k have been calculated in Ref. 6, and are given by

$$F_k = C_k \lambda_k^2 + C_k^* |\mu_k|^2 + D_k \lambda_k \mu_k^* - D_k^* \lambda_k \mu_k \quad , \quad (13)$$

and

$$G_k = D_k \lambda_k^2 + D_k^* \mu_k^2 - (C_k + C_k^*) \lambda_k \mu_k$$

$$= \frac{e^{2i\phi_k}}{2\omega_k} [D_k (A_k + \omega_k) e^{-2i\phi_k} + D_k^* (A_k - \omega_k) e^{2i\phi_k} - (C_k + C_k^*) B_k] \quad (14)$$

The equation of motion given by Eq. (12) contains a contribution due to the transverse components of \underline{h}_0 in the F_k and G_k terms, and a contribution due to the parallel component of \underline{h}_0 in the h_0^z terms.

GENERAL FIRST-ORDER INSTABILITY THRESHOLD

On the basis of Eqs. (12) and (14), the threshold fields for first-order and second-order instabilities can be calculated in a straightforward manner as described in Ref. 6. The $F_k + \gamma h_0^z A_k / \omega_k$ term in Eq. (12) leads only to a slight modulation and shift of the spin-wave frequency. The $G_k - \gamma h_0^z B_k \exp(2i\phi_k) / \omega_k$ coupling term leads to an unstable growth of the b_k with time for sufficiently high microwave power levels. For convenience, let

$$\tilde{G}_k = G_k - \gamma h_0^z B_k e^{2i\phi_k} / \omega_k \quad (15)$$

consider an equation of motion of the form

$$b_k = i(\omega_k b_k + \tilde{G}_k b_{-k}^*) \quad (16)$$

and introduce energy dissipation by replacing ω_k by $\Omega_k = \omega_k + i\eta_k$ where η_k is the relaxation rate for the b_k . This relaxation rate is related to the spin-wave linewidth ΔH_k by $\Delta H_k = 2\eta_k / \gamma$. The \tilde{G}_k can be expressed as

$$\tilde{G}_k = \sum_{n=-2}^{n=+2} \tilde{G}_k^{(n)} e^{in\omega t} \quad (17)$$

and the first-order instability can be evaluated by considering only the $n = 1$ term of Eq. (17), that part of \tilde{G}_k which varies as $e^{i\omega t}$. Similarly, the second order instability is obtained by considering the $n = 2$ term although this case will not be examined here. Considering the $n = 1$ term only, the equation of motion becomes

$$b_k = i \{ \Omega_k b_k + \tilde{G}_k^{(1)} e^{i\omega t} b_{-k}^* \} \quad (18)$$

It is convenient to rewrite this equation in terms of a new variable $b_{k0}(t)$ defined by

$$b_k = b_{k0}(t) e^{i\omega t/2} \quad (19)$$

and examine the conditions under which a stationary solution for the b_{k0} is permitted. By combining the differential equations for b_{k0} and b_{-k0}^* which result from Eq. (18) and (19), one obtains a second order differential equation,

$$\left\{ \frac{d^2}{dt^2} + 2\eta_k \frac{d}{dt} + \left[(\omega_k - \omega/2)^2 + \eta_k^2 - |G_k^{(1)}|^2 \right] \right\} b_{k0} = 0 \quad (20)$$

which has a solution $b_{k0} \propto \exp(\kappa t)$ where

$$\kappa = \eta_k \pm \left[|G_k^{(1)}|^2 - (\omega_k - \omega/2)^2 \right]^{1/2} \quad (21)$$

The stationary solution corresponds to $\kappa = 0$. The smallest value of $|\tilde{G}_k^{(1)}|$ for which this solution is permitted occurs when the spin-wave frequency ω_k is equal to one-half the excitation frequency ω . The quantity $|\tilde{G}_k^{(1)}|$ is proportional to the microwave field amplitude h_0 and the condition $|\tilde{G}_k^{(1)}| = \eta_k$ which corresponds to $\kappa = 0$ for $\omega_k = \omega/2$ determines the instability threshold amplitude for the state $(\omega/2, k)$. Larger amplitudes result in a positive κ and an exponential increase in b_{k0} with time.

The problem therefore reduces to the extraction of $\tilde{C}_k^{(1)}$ from Eqs. (8), (14), (15), and (17). In order to obtain $\tilde{C}_k^{(1)}$ it is necessary to consider the explicit time dependence of \underline{h}_0 and the resultant uniform precession amplitude a_0 . Let \underline{h}_0 be given by

$$h_0^x = h_0 a_x \cos(\omega t + \delta_x) \quad , \quad (22a)$$

$$h_0^y = h_0 a_y \cos(\omega t + \delta_y) \quad , \quad (22b)$$

and

$$h_0^z = h_0 a_z \cos(\omega t) \quad . \quad (22c)$$

Equations (22a-22c) provide an adequate basis for describing most experimentally attainable drive configurations. For example, setting δ_x and δ_y to zero and requiring that $a_x^2 + a_y^2 + a_z^2$ equal unity corresponds to linearly polarized excitation making an angle $\psi = \cos^{-1} a_z$ with respect to the z-direction and an angle $\phi = \cos^{-1} a_x$ with respect to the x-direction. With the abbreviations

$$X = \gamma(H + 4\pi M N_x) \quad , \quad (23a)$$

and

$$Y = \gamma(H + 4\pi M N_y) \quad , \quad (23b)$$

the complex uniform precession amplitude a_0 can be calculated from Eqs. (1), (2), (4), (22), and (23) to be

$$a_0 = \frac{\gamma h_0}{Z} (q_L e^{i\omega t} + q_A e^{-i\omega t}) \quad , \quad (24)$$

where

$$q_L = \frac{(\omega+Y) a_x e^{i\delta_x} + i(\omega+X) a_y e^{i\delta_y}}{XY - \omega^2}$$

and

$$q_A = - \frac{(\omega-Y) a_x e^{-i\delta_x} + i(\omega-X) a_y e^{-i\delta_y}}{XY - \omega^2}$$

Damping of the uniform precession may be taken into account by replacing X and Y by $\Omega_{ox} = X + i\eta_0$ and $\Omega_{oy} = Y + i\eta_0$, respectively. The relaxation rate η_0 is related to the uniform precession resonance linewidth ΔH by $\Delta H = 2\eta_0/\gamma$. Such a procedure is reasonable when only a Larmor rotating pump field is considered, as in the Suhl theory. For anti-Larmor pumping, the introduction of damping in this way results in a physically unreasonable negative energy absorption by the magnetic system. The origin of this inconsistency rests in the Bloch-Bloembergen formulation of relaxation for the uniform precession⁷ which is equivalent to the above procedure. In this formulation, the magnetization relaxes toward the direction of the static field, not the instantaneous internal field, and results in a negative energy absorption for anti-Larmor pumping. If damping is taken into account by means of a Landau-Lifshitz⁸ or Gilbert⁹ form for the relaxation, the inconsistency is eliminated. For sufficiently narrow linewidth materials, such fine points do not significantly alter the results. For first-order processes considered here, damping may be neglected completely for narrow linewidth materials without significantly modifying the results. For second-order processes, the above procedure is adequate for Larmor pumping and damping can be neglected in considering anti-Larmor pumping.

The contributions to $\tilde{G}_k^{(1)}$ are determined only by the explicit time dependences of h_0^z and G_k . From Eqs. (15) and (22), the h_0^z contribution is simply $-(\omega_m/\omega) (\gamma h_0/2) \sin^2 \theta_k a_z \exp(2i\phi_k)$. The G_k contribution is determined by Eqs. (8), (14), (22), and (24). The A_k and B_k have no explicit time dependence. The only terms in C_k , D_k , and their complex conjugates which vary as $e^{i\omega t}$ are those which contain a_0 or a_0^* to first order and do not contain h_0 explicitly. After collecting all terms in \tilde{G}_k which vary as $e^{i\omega t}$ the result is

$$\tilde{G}_k^{(1)} = -\frac{\omega_m}{\omega} \frac{\gamma h_0}{2} e^{2i\phi_k} \left[\sin \theta_k \cos \theta_k \left\{ q_L [f(\theta_k) + \omega/2] e^{-i\phi_k} + q_A^* [f(\theta_k) - \omega/2] e^{i\phi_k} \right\} + \sin^2 \theta_k a_z \right] \quad (25)$$

In the above

$$f(\theta_k) = \frac{1}{2} [(\omega_m^2 \sin^4 \theta_k + \omega^2)^{\frac{1}{2}} - \omega_m \sin^2 \theta_k] \quad (26)$$

and $f(\theta_k)$ is equal to $\gamma H + \gamma D k^2$ in the dispersion relation of Eq. (11c). The instability threshold field amplitude for spin-wave state ($\omega_k = \omega/2$, θ_k, ϕ_k) is simply the value of h_0 for which $|G_k^{(1)}| = \gamma \Delta H_k / 2$ is satisfied. Let W be defined by

$$\tilde{G}_k^{(1)} = -\frac{\omega_m}{\omega} \frac{\gamma h_0}{2} e^{2i\phi_k} W \quad (27)$$

and

$$W = \sin \theta_k \cos \theta_k \{ q_L [f(\theta_k) + \omega/2] e^{-i\phi_k} + q_A^* [f(\theta_k) - \omega/2] e^{i\phi_k} + \sin^2 \theta_k a_z \} \quad (28)$$

The threshold h_c is given by

$$h_c = \frac{\omega}{\omega_m} \frac{\Delta H_k}{|W|} \quad (29)$$

First-order processes are restricted to external field values for which spin waves with $\omega_k = \omega/2$ are allowed. From Eq. (11c), this condition is equivalent to the requirement $\omega/2 > \gamma H$. As γH approaches $\omega/2$, θ_k approaches zero and the $\sin \theta_k$ factor in W causes h_c to diverge.

The experimentally observed threshold for a first-order instability should correspond to the minimum value of h_c with respect to k for a given sample geometry, microwave field configuration, and applied static field. This theoretical minimum can be obtained by minimizing $|W|^{-1}$ with respect to θ_k and ϕ_k subject to the condition that the value of k at the minimum be real. This condition is equivalent to the requirement

$$f(\theta_k) - \gamma H \geq 0 \quad (30)$$

Let $\theta_k^{(min)}$ and $\phi_k^{(min)}$ be the values of θ_k and ϕ_k which minimize $|W|^{-1}$. If $\theta_k^{(min)}$ does not satisfy the inequality of Eq. (30), the $\theta_k^{(min)}$ which actually corresponds to the instability threshold is given by the θ_k solution to $f(\theta_k) - \gamma H = 0$ and \underline{k} is zero.

$$h_{crit} = \frac{\omega}{\omega_m} \frac{\Delta H_k}{|W(\theta_k^{(min)}, \phi_k^{(min)})|} \quad (31)$$

is the expected first-order instability threshold field for a given sample geometry, microwave field configuration, and static field.

In the above analysis, a first-order spin-wave instability threshold expression has been obtained for 1) samples of ellipsoidal shape magnetized to saturation along a major axis and 2) an arbitrary microwave pumping field configuration. No assumptions were made concerning sample symmetry, other than the ellipsoidal shape, or microwave field geometry, except that all fields were assumed uniform over the sample volume. Insofar as most of the analysis is quite similar to that previously reported by Suhl¹ and Schlömann,⁶ it is important to briefly summarize the specific differences between this and the earlier calculations which make possible the extension of the theory to more complicated situations. The first difference is the inclusion of both a parallel component h_o^z and transverse components, h_o^x and h_o^y , of the external microwave field in the initial equation of motion given by Eq. (5). By considering only terms to first order in the α_k due to both parallel and transverse field components in the equation of motion and applying a linear Holstein-Primakoff transformation to these terms, the coupling coefficient in the equation of motion which leads to instability, expressed in \tilde{G}_k of Eq. (16), is obtained for a general microwave field configuration. The second difference rests in the expression for the uniform precession amplitude α_o which was used to evaluate the coupling coefficient associated with the transverse components of \underline{h}_o . By utilizing the general expression for α_o given by Eq. (24), which is valid for an arbitrary transverse microwave field polarization and different transverse

demagnetizing factors, the requirements on sample symmetry and the transverse pump polarization are eliminated. These two changes concerning \underline{h}_0 and \underline{a}_0 constitute the major differences between the present calculation and the earlier theories. For simplicity, the discussion has been limited to first-order instability processes. Second-order processes and the steady state behavior above threshold have not been considered explicitly. From the general expression for \tilde{G}_k of Eq. (15), the threshold for second-order processes with $\omega_k = \omega$ and $n = 2$ can be easily evaluated in a manner analogous to that presented here. From the general equation of motion of Eq. (5), moreover, steady state behavior can be calculated by including higher order terms in the working equation of motion. The theory is quite general and applicable to a large variety of situations. Several simple applications of the theory for first-order processes will be considered in the next section.

DISCUSSION FOR SPECIAL CASES

The above refinements in the theory result in several modifications of the earlier predictions and extend the applicability of the theory to more general geometries and microwave field configurations. Although the result expressed by Eqs. (24), (26), (28), and (31) are quite general, the minimization procedure is most easily accomplished using numerical techniques. It is more illustrative to consider several special cases for which the equations simplify considerably, but which still demonstrate the new or modified results of the extended theory. Three specific situations will be considered.

- 1) Perpendicular pumping with linearly polarized microwave excitation;
- 2) Perpendicular pumping with circularly polarized drive rotating in the anti-Larmor sense;
- 3) Oblique pumping with linearly polarized drive.

In case (1), the contribution of the anti-Larmor rotating component of the linearly polarized pump field to h_{crit} will be demonstrated and the effect of sample geometry on the threshold will also be considered. In case (2), the threshold for anti-Larmor pumping will be calculated and compared with h_{crit} for Larmor pumping. In case (3), the dependence of h_{crit} on the

angle between the polarization axis for a linear polarized pump field and the static field direction will be demonstrated. In all three cases, the η_0 contributions to q_L and q_A will be neglected for simplicity. As long as the difference between the applied field H_0 and the field for resonance at the excitation frequency ω is large compared to the uniform precession resonance linewidth, the η_0 terms do not contribute significantly to the uniform precession amplitude a_0 . For first-order instability processes, the internal field must be less than $\omega/2\gamma$ and the above condition is usually satisfied. In all cases, the dependence of ΔH_k on \underline{k} will be neglected in the minimization procedure.

Case (1). For perpendicular pumping with a linearly polarized microwave field in the x-direction, δ_x , a_y , and a_z in Eq. (22) are zero, a_x is equal to unity, and the uniform precession amplitude is given by Eq. (24) with

$$q_L = \frac{Y + \omega}{XY - \omega^2} \quad (32a)$$

and

$$q_A = \frac{Y - \omega}{XY \omega^2} \quad (32b)$$

With q_L and q_A from Eqs. (32a, b), W in Eq. (28) simplifies to

$$W = \frac{\sin \theta_k \cos \theta_k}{\omega^2 - XY} \left\{ (Y + \omega) [f(\theta_k) + \omega/2] e^{-i\phi_k} + (Y - \omega) [f(\theta_k) - \omega/2] e^{i\phi_k} \right\} \quad (33)$$

The ϕ_k spin-wave angle determines the relative phases of the two complex terms in the curly brackets of Eq. (33). Therefore, the magnitude of W is maximized and the threshold h_c is minimized for $\phi_k = \phi_k^{(\min)}$ such that the phases of these two terms are equal.

$$|W(\theta_k, \phi_k^{(\min)})| = \frac{\sin \theta_k \cos \theta_k}{|\omega^2 - XY|} \left\{ (\omega + Y) [\omega/2 + f(\theta_k)] + |\omega - Y| [\omega/2 - f(\theta_k)] \right\} \quad (34)$$

The minimization of $|W(\theta_k, \phi_k^{(\min)})|^{-1}$ and h_c with respect to θ_k determines the threshold as discussed above and h_{crit} is given by

$$h_{\text{crit}} = \frac{\omega}{\omega_m} \frac{\Delta H_k |\omega^2 - XY|}{\sin \theta_k^{(\min)} \cos \theta_k^{(\min)}} \quad (35)$$

$$\{ (\omega + Y) [\omega/2 - f(\theta_k^{(\min)})] \} + \{ \omega - Y [\omega/2 - f(\theta_k^{(\min)})] \}^{-1}$$

The value for $\theta_k^{(\min)}$ is a complicated function of the sample shape, frequency, magnetization, and applied field. The value of $\phi_k^{(\min)}$, however, is determined only by the relative signs of the real terms in Eq. (33). With $f(\theta_k)$ as defined by Eq. (26), the expression $[f(\theta_k) - \omega/2]$ is always negative. If $(Y - \omega)$ is also negative, Eq. (34) corresponds to $\phi_k^{(\min)} = 0$ or $\phi_k^{(\min)} = \pi$. If $(Y - \omega)$ is positive, $\phi_k^{(\min)}$ is $\pm \pi/2$. For first-order processes, the static internal field H is constrained by the requirement $H < \omega/2\gamma$. The static internal field value below which $\phi_k^{(\min)}$ is 0 or π and above which $\phi_k^{(\min)}$ is $\pm \pi/2$ is determined by

$$Y - \omega = \gamma H + \gamma 4\pi M N_y - \omega = 0 \quad (36)$$

This ϕ_k transition field is less than $\omega/2\gamma$ only if the N_y demagnetizing factor is greater than $\omega/2\omega_m$. For yttrium iron garnet at 9.2 GHz, this condition reduces to $N_y > 0.94$. The instability can occur for $\theta_k^{(\min)} = \pm \pi/2$ only for very thin slabs magnetized in their plane and with the linearly polarized field also in the plane of the slab, perpendicular to the saturation direction. For most situations, therefore, instability occurs for spin waves with ϕ_k equal to zero or π .

Equation (35) represents the instability threshold field expected for transverse pumping in a saturated ferromagnetic ellipsoid with a linearly polarized microwave field along a principal axis in the x-direction and the static field along a principal axis in the z-direction. The $(\omega + Y)$ and $(\omega - Y)$

terms in the denominator of Eq. (34) may be viewed as due to the Larmor and anti-Larmor components of the linearly polarized field respectively. Previously, the usual procedure for obtaining h_{crit} for a linearly polarized transverse pump field has been to apply the Suhl theory to the Larmor rotating component of the field and neglect the anti-Larmor component. Such a procedure would result in Eq. (34) with the second term in the curly brackets omitted. The present result shows, however, that this anti-Larmor term has a noticeable effect on the threshold expression. First, the anti-Larmor term decreases h_{crit} from the Suhl prediction. Second, when this term is included the static field dependence of the denominator cannot be separated from the θ_k dependence so that for $\underline{k} \neq 0$, $\theta_k^{(\text{min})}$ is a function of static field. In the Suhl theory, $\theta_k^{(\text{min})}$ is independent of static field for $\underline{k} \neq 0$ and only a function of ω/ω_m . Finally, h_{crit} is not independent of the ϕ_k spin-wave angle. In order to illustrate these effects, specific results for spherical samples are shown in Fig. 1. Normalized curves of $h_{\text{crit}}/\Delta H_k$ are shown as a function of applied field H_0 normalized to (ω/γ) with ω_m/ω as a parameter. The solid curves correspond to h_{crit} when the anti-Larmor contribution is included and the dotted curves were calculated neglecting this contribution. The two effects pointed out above are apparent from these curves. 1) For a linear pump field, h_{crit} is reduced somewhat from the value predicted by neglecting the anti-Larmor component of the drive and applying the Suhl theory, particularly at low field. 2) For static field less than that for the minimum threshold, $h_{\text{crit}}/\Delta H_k$ is not a linear function of applied field H_0 as expected from the Suhl theory.

In order to demonstrate the consequences of the relaxation of the rotational symmetry requirement in the theory, curves of $h_{\text{crit}}/\Delta H_k$ as a function of $H_0/(\omega/\gamma)$ for perpendicular pumping with linearly polarized microwave drive were also calculated for samples with planar geometry magnetized in their plane. These results are shown in Fig. 2. Two cases were considered: 1) \underline{h}_0 parallel to the plane of the slab; 2) \underline{h}_0 perpendicular

to the plane of the slab. In-plane demagnetizing factors of zero and an out-of-plane demagnetizing factor of unity were assumed. For \underline{h}_0 perpendicular to the plane of the slab, the threshold amplitude is significantly higher than for \underline{h}_0 in the plane. This result can be explained by considering the effect of geometry on the uniform precession amplitude a_0 , which is the important parameter in determining the threshold for perpendicular pumping. For a parallel \underline{h}_0 , Y is given by $Y = \gamma H + \omega_m$. For a normal \underline{h}_0 , $Y = \gamma H$ is satisfied. From Eq. (32a), then, it can be seen that q_L is larger for \underline{h}_0 parallel to the plane of the slab than for \underline{h}_0 normal to the slab. Consequently, a normal \underline{h}_0 is less efficient in pumping the uniform precession than an in-plane \underline{h}_0 and the h_{crit} for a microwave field perpendicular to the slab is higher. Such differences are not accessible when rotational symmetry is assumed because all transverse directions are then equivalent.

Case (2). The instability threshold for perpendicular pumping with a circularly polarized microwave field rotating in an anti-Larmor sense can be obtained by omitting the $(\omega + Y)$ term in Eq. (33) and multiplying the expression by two. The factor of two compensates for the factor of one-half between the amplitude of a linearly polarized field and the amplitude of its Larmor or anti-Larmor rotating components. For comparison, the instability threshold for Larmor pumping may be evaluated by setting the $(\omega - Y)$ term in Eq. (33) to zero, as in the Suhl theory, and including the factor of two. Theoretical curves for both cases are shown in Fig. 3. The upper set of curves correspond to anti-Larmor pumping and the lower set of curves to Larmor pumping. The curves were calculated for spherical samples. The results in Fig. 3 illustrate two important points concerning anti-Larmor pumping. 1) The threshold is significantly higher than for Larmor pumping. (Note that the h_{crit} axis is logarithmic.) 2) The threshold does not, in general, exhibit the usual minimum which is characteristic of Larmor pumping, although the anti-Larmor curve does exhibit a small, local minimum for large ω_m/ω .

Case (3). Finally, consider oblique pumping with a linearly polarized microwave field making an angle Ψ with the direction of the static external field and polarized in the x-z plane. This field corresponds to $a_y = 0$, $\delta_x = 0$, $a_x = \sin \Psi$, and $a_z = \cos \Psi$. Also assume, for simplicity, that the static field is along an axis of rotational symmetry so that X and Y are both equal to the natural uniform precession frequency ω_0 . With these assumptions,

$$q_L = \frac{\sin \Psi}{\omega_0 - \omega} \quad (37a)$$

and

$$q_A = \frac{\sin \Psi}{\omega_0 + \omega} \quad (37b)$$

For this situation, W in Eq. (28) simplifies to

$$W = \sin \theta_k \cos \theta_k \left\{ \frac{\sin \Psi [f(\theta_k) + \omega/2]}{\omega_0 - \omega} e^{-i\phi_k} + \frac{\sin \Psi [f(\theta_k) - \omega/2]}{\omega_0 + \omega} e^{i\phi_k} \right\} + \sin^2 \theta_k a_z \quad (38)$$

As pointed out previously, $f(\theta_k) - \omega/2$ is negative. For first-order processes, moreover, the sample is biased below ferromagnetic resonance so that ω_0 is less than ω . The coefficients of the $e^{\pm i\phi_k}$ terms in the curly brackets of Eq. (38) are both negative. Phases are matched for all terms only for $\theta_k = \pi$ so that $|W|$ is maximized and h_c minimized with respect to ϕ_k at $\phi_k^{(\min)} = \pi$. This result is strictly valid only if the damping of the uniform precession is neglected. If ω_0 is assigned an imaginary part η_0 corresponding to the uniform precession relaxation rate as described in the last section, the phases of the terms in the curly brackets of Eq. (38) are modified. The change is small for small damping.

If the uniform precession damping is neglected, $\phi_k^{(\min)}$ is exactly π and $|W|$ is given by

$$|W(\theta_k, \phi_k^{(\min)})| =$$

$$\sin \theta_k \left\{ \frac{\cos \theta_k \sin \psi}{\omega^2 - \omega_0^2} [2\omega_0 f(\theta_k) + \omega^2] + \cos \psi \sin \theta_k \right\} . \quad (39)$$

The threshold h_{crit} is then obtained by minimizing $|W|^{-1}$ with respect to θ_k as discussed above. In Fig. 4, normalized curves of $h_{\text{crit}}/\Delta H_k$ as a function of $H_0/(\omega/\gamma)$ are shown with ψ as a parameter. Spherical samples and $\omega_m/\omega = 0.54$ corresponding to yttrium iron garnet at 9.2 GHz were assumed. The curve for $\psi = 0^\circ$ corresponds to parallel pumping and the $\psi = 90^\circ$ curve corresponds to perpendicular pumping. The curves illustrate the dependence of $h_{\text{crit}}/\Delta H_k$ on pumping angle. Actual h_{crit} curves would be slightly modified because of the k dependence of ΔH_k which influences $\theta_k^{(\min)}$. At low field, $h_{\text{crit}}/\Delta H_k$ increases with ψ and is most sensitive to angles near $\psi = 90^\circ$. At high field, $h_{\text{crit}}/\Delta H_k$ decreases with ψ and is most sensitive to angle near $\psi = 0^\circ$. The threshold field minimum moves to higher static field with increasing ψ .

SUMMARY AND CONCLUSION

Spin-wave instability theory has been extended to include pumping with an arbitrary microwave field configuration and ellipsoidal samples magnetized along a principal axis which is not necessarily an axis of rotational symmetry. The calculations have been carried out explicitly for the first-order instability threshold. Several special cases have been considered to demonstrate the versatility of the theory in analyzing situations previously inaccessible on the basis of the original theoretical treatment. Sample geometry and the pump configuration have a strong influence on the instability threshold amplitude.

ACKNOWLEDGEMENTS

The author is indebted to E. Schlömann for helpful discussions concerning spin-wave instability theory in general and concerning uniform precession damping in particular, and to Mrs. B. Matsinger for assistance with the numerical calculations.

REFERENCES

1. H. Suhl, *J. Phys. Chem. Solids* 1, 209 (1957).
2. See E. Schlömann, J. J. Green, and U. Milano, *J. Appl. Phys.* 31, 386 S (1960).
3. L. V. Kitaev, A. A. Goncharova, and G. I. Katamaran, *Sov. Phys. Solid State* 9, 246 (1967). Translation from Russian.
4. E. Stern, G-MTT International Microwave Symposium, Boston, 1967, *IEEE Cat. No. 17C66*, p. 103.
5. J. J. Green, E. Stern, and C. E. Patton, to be published.
6. E. Schlömann, Raytheon Tech. Rept. R-48 (1959).
7. N. Bloembergen, *Proc. IRE* 44, 1259 (1956).
8. L. Landau and E. Lifshitz, *Physik Z. Sowjetunion* 8, 153 (1935).
9. T. L. Gilbert, *Phys. Rev.* 100, 1243 (1955).

* This work was supported by the Advanced Research Projects Agency of the Department of Defense and was monitored by Rome Air Development Center under Contract No. F 30602-68-C-0005.

FIGURE CAPTIONS

- Fig. 1** First-order spin-wave instability threshold field h_{crit} normalized to the spin-wave linewidth ΔH_k as a function of the static external field H_0 normalized to ω/γ , the angular excitation frequency divided by the gyromagnetic ratio. Curves were obtained for spherical samples and a linearly polarized microwave excitation, with ω_m/ω ($\omega_m = \gamma 4\pi M$ is the saturation induction) as a parameter. The dotted curves neglect the contribution of the anti-Larmor component of the microwave field to h_{crit} .
- Fig. 2** Normalized first-order spin-wave instability threshold field h_{crit} as a function of the normalized static external field H_0 . Curves are shown for thin disk shaped samples with an in-plane demagnetizing factor of zero and linearly polarized microwave excitation parallel to ($h_0 \parallel$) or perpendicular to ($h_0 \perp$) the slab plane. The slab was assumed to be magnetized to saturation in its plane and perpendicular to the microwave field direction. Sets of curves are shown for $\omega_m/\omega = 1/2$ and $\omega_m/\omega = 1$.
- Fig. 3** Normalized first-order spin-wave instability threshold field h_{crit} as a function of the normalized static external field H_0 . Curves were calculated for spherical samples and a circularly polarized microwave excitation perpendicular to the static field direction, with ω_m/ω as a parameter. Results are shown for a Larmor excitation, rotating in the proper sense to excite ferromagnetic resonance, and an anti-Larmor excitation, rotating in the opposite sense.
- Fig. 4** Normalized first-order spin-wave instability threshold field h_{crit} as a function of the normalized static external field h_0 . Curves were calculated for spherical samples and a linearly polarized microwave field at angles of 0° , 30° , 60° , and 90° to the static field direction. The values indicated correspond to $\omega_m/\omega = 0.54$ which is appropriate for yttrium iron garnet at 9.2 GHz.

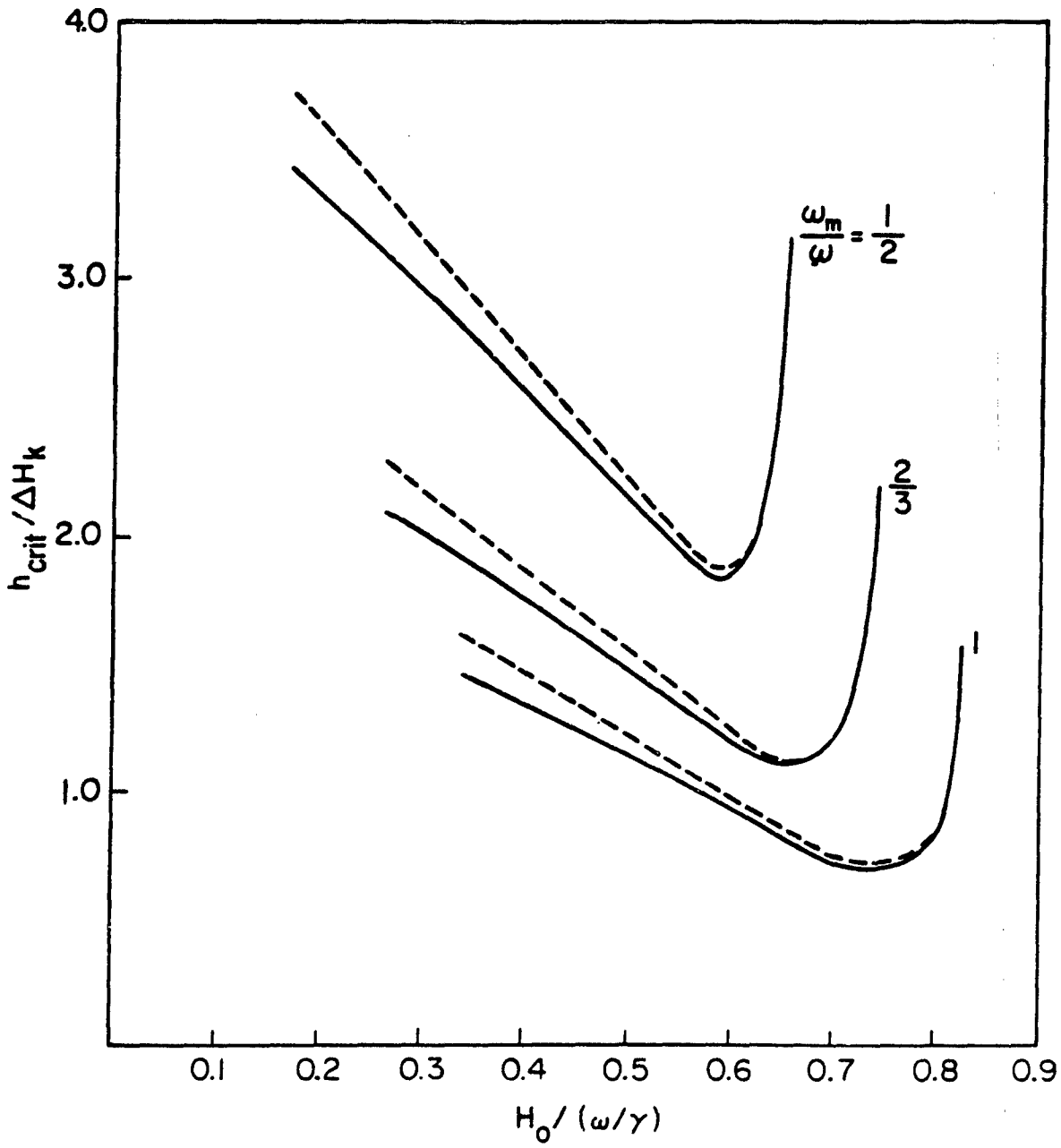


FIGURE 1

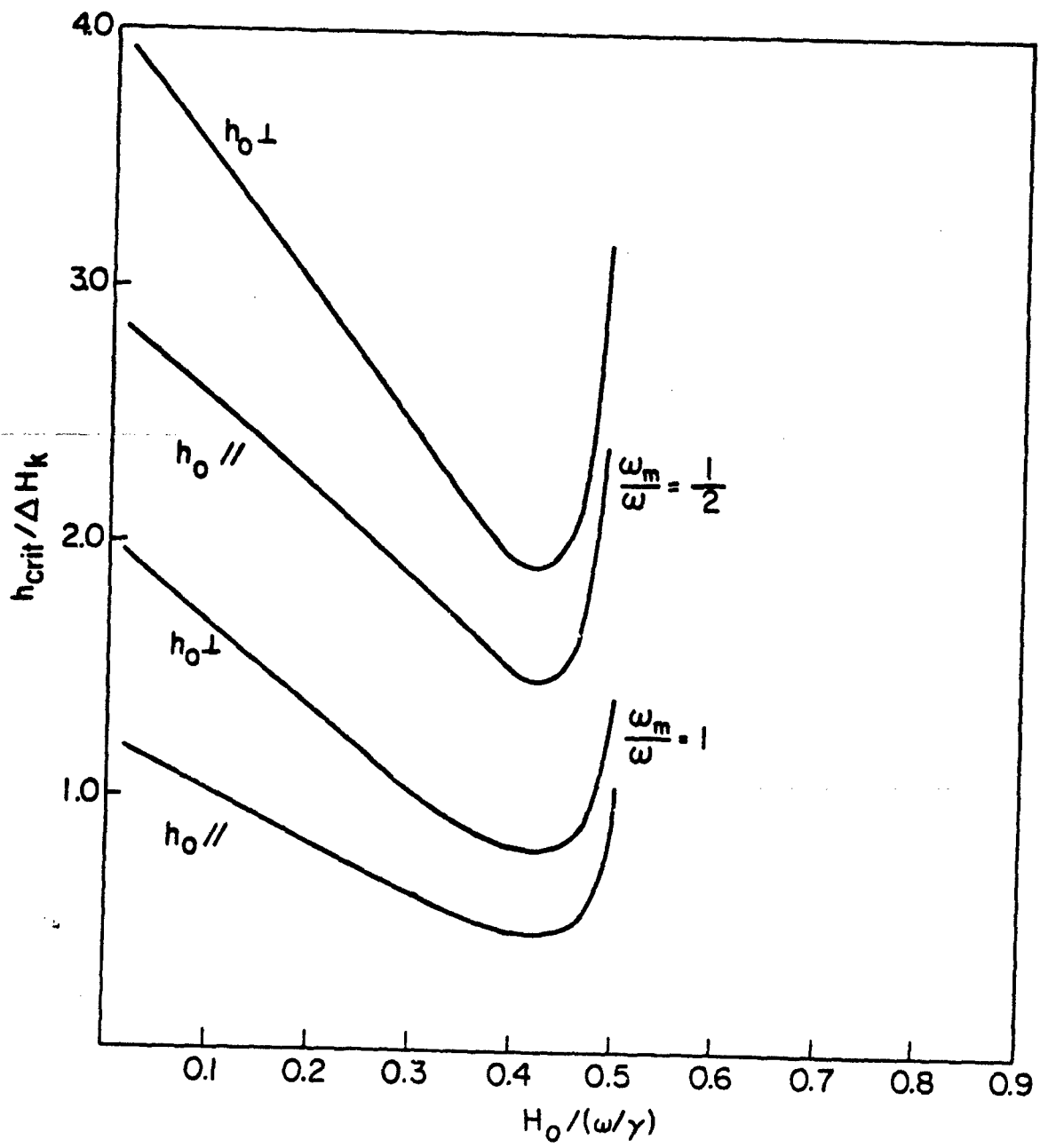


FIGURE 2

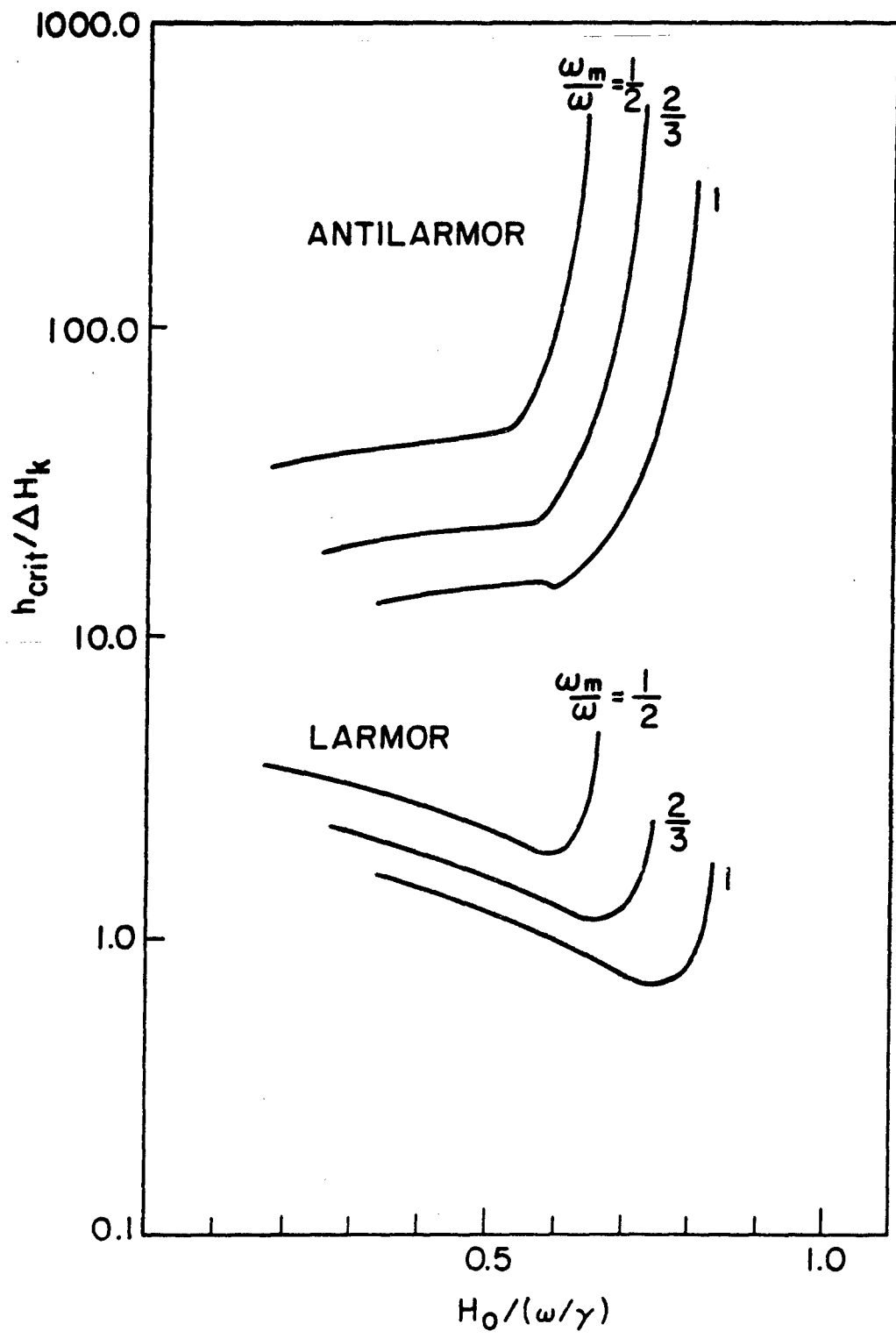


FIGURE 3

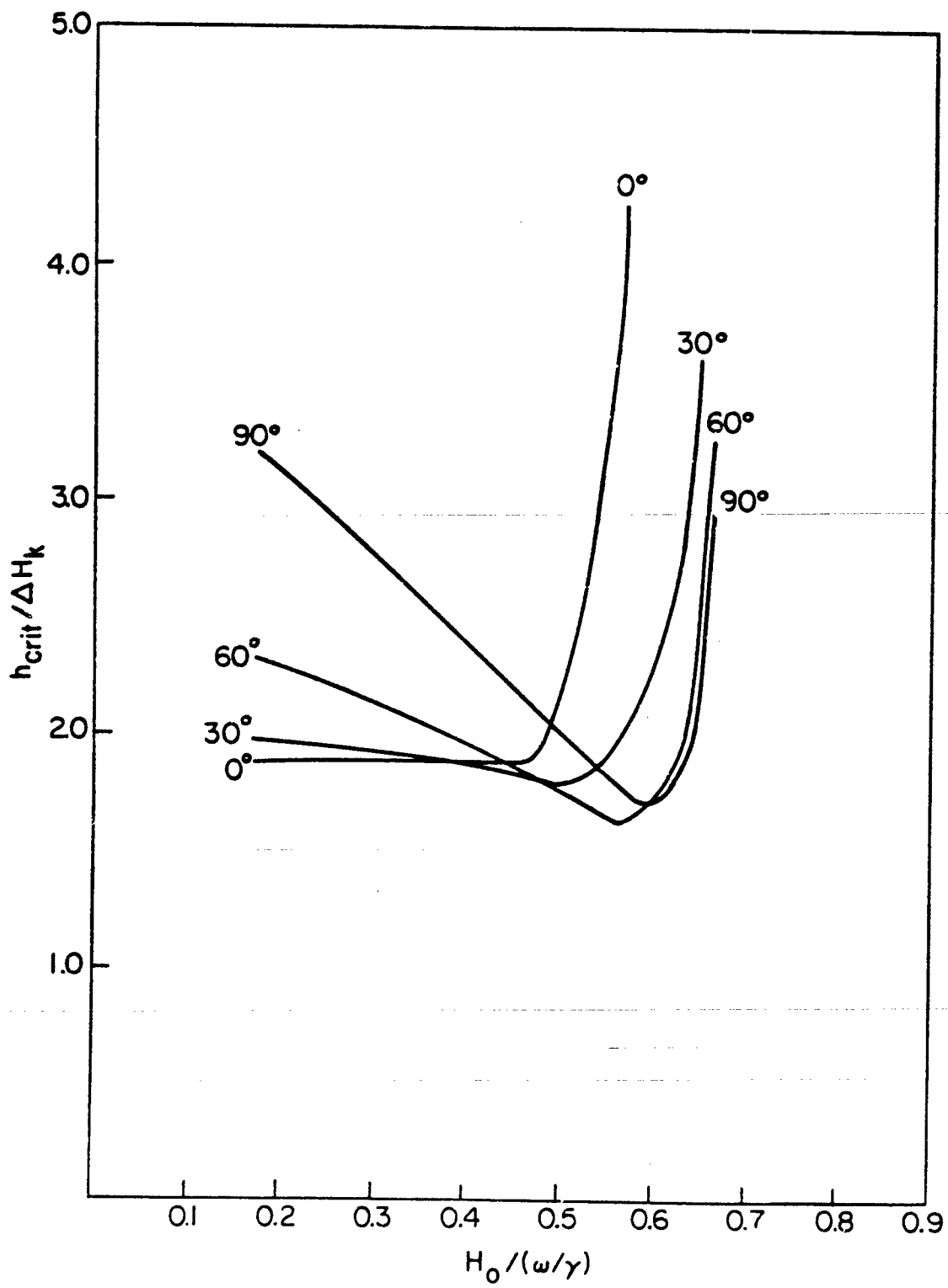


FIGURE 4

THRESHOLD MICROWAVE FIELD AMPLITUDE FOR THE UNSTABLE
GROWTH OF SPIN WAVES UNDER OBLIQUE PUMPING

J. J. Green*

Raytheon Company, Research Division, Waltham, Mass.

E. Stern

Lincoln Laboratory, Massachusetts Institute of Technology
Lexington, Mass. †

and C. E. Patton*

Raytheon Company, Research Division, Waltham, Mass.

ABSTRACT

The threshold microwave field amplitude h_{crit} required for the unstable growth of spin waves has been investigated for oblique pumping with a linearly polarized microwave field applied at an arbitrary angle with respect to the static magnetic field. The experiment was performed on YIG (1 percent Dy) spheres at 9.2 GHz using a rectangular TE_{102} cavity and a pulsed magnetron source. Data were obtained at static external fields of 400, 600, 1100, and 1500 Oe. In general, h_{crit} increases with the pump angle. Theoretical expressions for the oblique pumping h_{crit} have been derived for ferromagnetic insulators of ellipsoidal shape and with axial symmetry about the direction of the static magnetic field sufficient to saturate the sample. If the difference between the angular pump frequency divided by the gyromagnetic ratio and the static internal field is much greater than the ferromagnetic resonance linewidth at the pump frequency, the threshold field is determined by maximizing $1/h = \cos \psi/h_{\parallel} + \sin \psi/h_{\perp}$ with respect to the angle between the internal field and the spin wave propagation direction. Here, h_{\parallel} and h_{\perp} are the parallel and perpendicular pump threshold fields of Schlömann and Suhl. For external fields sufficient to magnetize the spherical samples to saturation, the theoretical predictions are in good agreement with the experimental data. For smaller fields, the agreement is poor. However, fair agreement is obtained by assuming a transverse demagnetizing factor N_t greater than the value of $1/3$ which is appropriate for saturated spherical samples. The value of N_t for the best theoretical fit depends on the way in which

the sample is demagnetized. This result indicates that for samples not magnetized to saturation, the magnetic structure consists of elongated domains and that the oblique pumping data can be explained from the theory for saturated systems assuming demagnetizing factors appropriate to the domain structure.

INTRODUCTION

The parallel and perpendicular pumping of spin waves in insulating ferromagnets has received considerable attention in recent years. Suhl¹ has calculated the threshold microwave field amplitude required for the unstable growth of spin waves with the microwave field perpendicular to the static magnetic field for saturated samples of ellipsoidal shape with a rotational axis of symmetry parallel to the static field. Schlömann et al.² have considered the situation for the microwave field parallel to the static field. There has been little work concerning the threshold fields for the unstable growth of spin waves under so-called oblique pumping with a linearly polarized microwave field at an angle $0 \leq \psi \leq 90^\circ$ with the static field direction. Stern³ has discussed oblique pumping as related to remanent ferrite device operation. Kitaev et al.⁴ have considered the theoretical problem of pumping with an arbitrary pump field, although specific results were shown only for an infinite medium. An experimental and theoretical investigation of oblique pumping is the subject of the present report. The experimental results for saturated spherical samples are in good agreement with the theory. For applied static fields insufficient to saturate the samples, fair agreement can be obtained by assuming transverse demagnetizing factors which correspond more closely to the domain shape than the sample shape.

EXPERIMENT AND RESULTS

The spin wave instability threshold for oblique pumping was determined from microwave susceptibility data obtained using cavity perturbation techniques and a rectangular TE_{102} reflection cavity at 9.2 GHz.^{5,6} Determinations of h_{crit} were made as a function of pumping angle ψ for $0^\circ \leq \psi \leq 90^\circ$ for a one percent dysprosium doped polycrystalline yttrium iron garnet sphere with a linewidth of 50 Oe at 9.2 GHz and a saturation magnetization of 1750 G. This particular sample was chosen for two reasons: (1) The rare earth contribution to the spin-wave linewidth should dominate over other contributions, thereby facilitating the theoretical interpretation of the data, and (2) the spin-wave linewidth is still small enough to allow measurement of the threshold field h_{crit} with the maximum attainable microwave field amplitude of 80 Oe.

In Figs. 1 to 4, the threshold field h_{crit} is shown as a function of pumping angle ψ for external static fields of 400, 600, 1100, and 1500 Oe respectively. At all but the highest field, h_{crit} increases with pumping angle. These data are in qualitative agreement with previous measurements by Green et al.⁷ which indicated that the parallel pump threshold corresponding to $\psi = 0$ was significantly lower than that for $\psi = \pi/2$ and perpendicular pumping. The present data on threshold field as a function of pump angle provide several new conclusions concerning spin-wave instabilities in ferromagnetic insulators. First, these data can be interpreted in terms of the previous calculations for parallel and perpendicular pumping, if the theories are extended to include oblique pumping. Second, the data for samples in a nonsaturated state are also in qualitative agreement with the theory developed for saturated systems if transverse demagnetizing factors appropriate to the domain shape and not the sample shape are used. In the next section, the theory of oblique pumping will be presented and in the following section, the above data will be interpreted in terms of the theory.

THEORY

The normal magnetic modes for ferromagnetic samples of ellipsoidal shape, have been calculated by Holstein and Primakoff,⁸ who obtain a dispersion relation of the form:

$$\omega_k = \gamma [(H_i + Dk^2) (H_i + Dk^2 + 4\pi M_s \sin^2 \theta_k)]^{\frac{1}{2}} \quad (1)$$

where ω_k is the angular frequency of a spin-wave with wave vector of magnitude k and at an angle θ_k with the direction of the internal field H_i , γ is the gyromagnetic ratio (1.76×10^7 Oe⁻¹ -sec⁻¹), D is a phenomenological exchange parameter ($\approx 5 \times 10^{-9}$ Oe-cm² for YIG), and $4\pi M_s$ is the saturation induction (≈ 1750 G). In Fig. 5, ω_k is shown as a function of k for $\theta_k = 0$ and $\pi/2$, as calculated for YIG from Eq. (1) with an internal field of 180 Oe. The region bounded by these two curves is called the spin-wave manifold.

If a linearly polarized microwave field $he^{i\omega t}$ of frequency ω is applied to the ferromagnetic sample, perpendicular to the static internal field (perpendicular pumping), Zeeman, dipolar, and exchange interactions give rise to a coupling between the uniform precession spin wave at ω driven by the microwave field and other spin-wave states. For sufficiently intense microwave drive, this coupling leads to the unstable growth of certain spin-wave amplitudes. If the microwave field is applied parallel to the static internal field (parallel pumping), the uniform precession amplitude is zero. For parallel pumping, however, spin-wave states are coupled directly to the microwave drive and spin-wave instabilities may also occur for sufficiently intense microwave field amplitudes. For the special case of saturated ferromagnetic insulators, in the shape of ellipsoids of revolution about the internal field direction, Suhl¹ has calculated the threshold field h_{\perp} required for the unstable growth of the spin-wave amplitude, for state (ω_k, k, θ_k) under perpendicular pumping and Schlömann et al.² have calculated the corresponding threshold h_{\parallel} for parallel pumping. The calculations indicate that the threshold is particularly low if $\omega_k = \omega/2$ and the pumping of unstable spin waves at $\omega/2$ has been termed a first order process (strong coupling). For a first order process, the results are

$$h_{\perp} = \frac{\omega}{\omega_m} \frac{\Delta H_k}{\sin \theta_k \cos \theta_k} \frac{[(\omega_0 - \omega)^2 + (\gamma \Delta H / 2)^2]^{1/2}}{\omega/2 + \gamma D k^2 + \gamma H_i} \quad (2a)$$

$$h_{\parallel} = \frac{\omega}{\omega_m} \frac{\Delta H_k}{\sin^2 \theta_k} \quad (2b)$$

where ω_m is given by $\gamma 4\pi M_s$, ω_0 is the uniform precession resonance frequency $\omega_0 = \gamma H_i + N_t \omega_m$ for a given internal field H_i and transverse demagnetizing factor N_t , ΔH_k is the spin-wave linewidth, and ΔH is the uniform precession linewidth at frequency ω . The particular magnon which has the lowest h_{\perp} for perpendicular pumping or h_{\parallel} for parallel pumping will be the one which goes unstable first and will control the experimentally determined threshold field h_{crit} . For perpendicular pumping the threshold field corresponds to spin waves with $\theta_k \approx \pi/4$ and for parallel pumping $\theta_k = \pi/2$ spin waves determine the threshold. These two states are indicated as black dots in Fig. 5 for an excitation frequency of 9.2 GHz. In the above and in the discussion to follow, it is assumed that ω is sufficiently high or H_i is sufficiently low so that $\omega/2$ is above the $\theta = \pi/2$ branch of the manifold at $k = 0$. The theory is strictly valid only for $k > 0$.

In an oblique pumping experiment both a parallel microwave field component $h e^{i\omega t} \cos \psi$ and a perpendicular microwave field component $h e^{i\omega t} \sin \psi$ are present and the possibility exists that some magnon state with $\pi/4 < \theta_k < \pi/2$ determines the threshold field. Such a state is represented by the open circle in Fig. 5. The oblique pumping threshold field can be calculated in a straightforward manner by considering the hamiltonian for the magnetic system in the presence of an oblique pumping field, calculating the spin-wave amplitude equation of motion, and proceeding according to the technique developed by Suhl and Schlömann. For the present purposes, however, it is more illustrative of the physical processes involved to calculate the threshold from a circuit analogy, as reported previously by one of the authors.³ The spin-wave theory is outlined in the appendix. Assuming linear coupling between the pumping field and the spin system, as illustrated by the equivalent circuit in Fig. 6, and taking the phases

of the perpendicular and parallel coupling coefficients, C_{\perp} and C_{\parallel} , to be equal, the effective spin-wave drive U may be defined as

$$U = C_{\parallel} h \cos \psi + C_{\perp} h \sin \psi \quad (3)$$

where C_{\parallel} and C_{\perp} depend on the particular magnon state $(\omega/2, k, \theta_k)$ being pumped. In Eq. (3), $h \cos \psi$ and $h \sin \psi$ are the parallel and perpendicular components of the microwave field amplitude, respectively. The instability for a particular spin wave occurs when U exceeds an effective drive threshold T which can be determined by considering the known theoretical threshold for that spin wave from Eq. (2) for $\psi = 0^\circ$ and $\psi = 90^\circ$. A parallel pumped instability occurs for $T = C_{\parallel} h_{\parallel}$ and a perpendicular pumped instability for $T = C_{\perp} h_{\perp}$. With $C_{\parallel} = T/h_{\parallel}$ and $C_{\perp} = T/h_{\perp}$, Eq. (3) becomes

$$\frac{U}{h} = \frac{T}{U} \left(\frac{\cos \psi}{h_{\parallel}} + \frac{\sin \psi}{h_{\perp}} \right)$$

Instability occurs when $U = T$ is satisfied so that the threshold field amplitude h_{oblique} required to drive state $(\omega/2, k, \theta_k)$ unstable is given by

$$\frac{1}{h_{\text{oblique}}} = \frac{\cos \psi}{h_{\parallel}} + \frac{\sin \psi}{h_{\perp}} \quad (4)$$

In the appendix Eq. (4) is obtained from spin-wave theory. It is shown that the equal phase assumption can be satisfied by correctly choosing the angle ϕ_k between the component of \underline{k} in the plane normal to \underline{H}_0 and the transverse component of the microwave field.

The oblique pumping threshold field h_{crit} is obtained by maximizing the right-hand side of Eq. (4), thereby minimizing h_{oblique} . If the spin-wave linewidth ΔH_k is independent of k and θ_k , h_{crit} as a function of ψ at constant external field can be calculated from Eqs. (2) and (4). If ΔH_k depends on k and θ_k , the minimization procedure necessary to determine the spin-wave state $(\omega/2, k, \theta_k)$ which gives the lowest threshold h_{crit} is more complicated. An approximate procedure was used to take the k and θ_k dependence of ΔH_k into account.

It was assumed that the k and θ_k dependences of ΔH_k could be expressed in a form

$$\Delta H_k = f_1(k) \cdot f_2(\theta_k) \quad (5)$$

with

$$f_1(k) = A + Bk \quad (6)$$

and

$$f_2(k) = 1 + C(\pi/2 - \theta_k) + D(\pi/2 - \theta_k)^2 \quad (7)$$

Both parallel and perpendicular data indicate that ΔH_k is approximately an increasing linear function of k . The A and B parameters were obtained from ΔH_k vs k determinations on the basis h_{crit} data for parallel pumping on the Dy doped material. These results are shown in Fig. 7. The A parameter was determined to be 15.0 and B is 0.5×10^{-5} . The parameters in $f_2(\theta_k)$ were determined by fitting the theoretical curve of $h_{oblique}$ vs pump angle, calculated from Eqs. (2), (4), and (5) - (7), to the experimental h_{crit} data for a static external field of 1100 Oe. Using this procedure, C was determined to be 0.15 and D was -0.3. For a heavy rare earth doping, ΔH_k is expected to be approximately constant and not exhibit strong k or θ_k dependences. This expectation is satisfied by the above result. The theoretical results would probably not be severely modified if ΔH_k was assumed to be constant. Consequently, the specific form for the weak k and θ_k dependences should not be critical.

DISCUSSION

First consider the data for external fields sufficient to magnetize the test sample nearly to saturation, as shown in Fig. 3 for an external field of 1100 Oe and in Fig. 4 for a field of 1500 Oe. As discussed in the last section, a qualitative best fit between the theory and data at 1100 Oe was used to determine the parameters A and B in the θ_k dependence of ΔH_k . As evident from Fig. 3, this two parameter fit gives good agreement with the data. The theoretical curve was obtained using a transverse demagnetizing factor of $1/3$, appropriate for saturated spherical samples. If oblique pumping simply consisted of simultaneous but independent parallel and perpendicular pumping, one would expect the observed threshold to correspond to either $h_{\parallel}/\cos \psi$ or $h_{\perp}/\sin \psi$ whichever was lower. The independent pumping model, therefore, predicts an increase in h_{crit} with ψ to about 60° , as indicated by the $h_{\parallel}/\cos \psi$ curve, and a subsequent decrease at higher angles, as indicated by the $h_{\perp}/\sin \psi$ curve. The agreement between the data in Fig. 3 and the independent pumping model is rather poor. In Fig. 4, the calculated h_{crit} vs ψ curve for a static field of 1500 Oe is shown for comparison with the data. The theoretical curve was obtained using the ΔH_k , θ_k and k dependence determined from the fit at 1100 Oe. There are no adjustable parameters available to adjust the fit between the data and theory for Fig. 4. The agreement is quite good. The close agreement between the theoretical curves and the data in Figs. 3 and 4 indicate that for saturated ferromagnetic insulators in the shape of ellipsoids of revolution about an axis parallel to the static field, the first order instability threshold for oblique pumping can be obtained from the extension of previous theories of parallel and perpendicular pumping.

For external fields less than $4\pi M_s/3$, or about 600 Oe for YIG, spherical samples are not magnetized nearly to saturation, and the samples consist of discrete domains. In the presence of domain structure, the theory is not strictly applicable. Nevertheless, it is informative to compare the data for external fields below $4\pi M_s/3$ with the theoretical predictions. Oblique pumping h_{crit} data as a function of ψ are shown in Figs. 1 and 2 for

external fields of 400 and 600 Oe, respectively. First consider the data at 400 Oe. The upper theoretical curve was calculated assuming a transverse demagnetizing factor of $1/3$, appropriate for saturated spheres. The agreement between the data and this theoretical curve is extremely poor. Better agreement can be obtained, however, if the transverse demagnetizing factor is assumed to be $1/2$, as shown by the lower solid curve. With this assumption the shape of the theoretical curve closely matches the data although the values are somewhat lower. Some variation in the experimental data has been noted which depends on the way in which the sample was demagnetized. In general, a good fit to any particular set of data could be obtained with $1/3 < N_t < 1/2$. Stern has previously reported data on partially magnetized toroids which agree with theory for $N_t = 1/2$.³ Agreement for $1/3 < N_t < 1/2$ indicates that the portions of the material which go unstable first correspond to elongated domains. Such domains would have $N_t \approx 1/2$. Further support for the proposal that the domain structure is important in determining the instability threshold is provided by the data at 600 Oe, shown in Fig. 2. At 600 Oe, the internal field is approximately zero for YIG and the material is nearly saturated. The theoretical curve shown in Fig. 2 which provided the best fit to the data was obtained for $N_t = 0.38$, slightly greater than the value of $1/3$ expected for saturated spheres due to the residual domain structure at 600 Oe. It should be emphasized that the same ΔH_k dependence which was used to obtain the theoretical curves for external fields greater than $4\pi M_s/3$ was used to calculate the curves shown in Figs. 2 and 1. The only adjustable parameter was N_t . Demagnetization effects due to domain structure have been used to explain large low field loss in ferromagnetic insulators.⁹ The present data and theoretical agreement indicate that domain structure also influences the instability threshold. Demagnetizing factors appropriate to the domain structure and not the sample shape should be used in theoretical estimates of h_{crit} for partially magnetized samples. Any quantitative comparison for systems below saturation, however, will require extension of the theory to include samples which are not ellipsoids of revolution and the effect of the antilararmor component of the linear drive, as well as more precise information concerning domain structure.

SUMMARY

This investigation has provided new information and new understanding concerning the microwave field thresholds for the excitation of spin-wave instabilities in ferromagnetic insulators. (1) Extensive data on the oblique pumping threshold as a function of pumping angle have been obtained for external fields both above and below that required to magnetize the sample to saturation. (2) The theory of parallel and perpendicular pumping in saturated ferromagnetic insulators has been extended to include oblique pumping. (3) The data for saturated samples can be explained by the theory. (4) The data for unsaturated samples can be qualitatively explained by the theory if transverse demagnetizing factors appropriate to the domain structure and not the sample geometry are assumed.

APPENDIX

Following the treatment by Schlömann,¹⁰ the spin-wave instability threshold field amplitude for oblique pumping can be obtained by considering a hamiltonian for the magnetic system of the form

$$\begin{aligned} \mathcal{H} = & \sum_{\mathbf{k}} \omega_{\mathbf{k}} b_{\mathbf{k}} b_{\mathbf{k}}^* \\ & + \frac{1}{2} \sum_{\mathbf{k} \neq 0} (f_{\mathbf{k}} b_0^* b_{\mathbf{k}} b_{-\mathbf{k}} + \text{c. c.}) \\ & - \frac{1}{2} \cos \omega t \sum_{\mathbf{k}} (c_{\mathbf{k}} b_{\mathbf{k}}^* b_{-\mathbf{k}}^* + \text{c. c.}) \end{aligned} \quad (\text{A1})$$

where $\omega_{\mathbf{k}}$ is the spin-wave frequency, the $b_{\mathbf{k}}$ are spin-wave amplitudes, $f_{\mathbf{k}}$ is a coupling coefficient for perpendicular pumping ($\psi = 90^\circ$), and $c_{\mathbf{k}}$ is a coupling coefficient for parallel pumping ($\psi = 0^\circ$) assuming a $\cos \omega t$ time dependence for the component of the microwave field along the static field. With parallel and perpendicular microwave field components $h \cos \omega t \cos \psi$ and $h \cos \omega t \sin \psi$, respectively, the coupling coefficients of Eq. (A1) are¹¹

$$f_{\mathbf{k}} = - \frac{\omega_m}{2\omega_{\mathbf{k}}} [\gamma H_i + \gamma Dk^2 + \omega_{\mathbf{k}}] e^{-i\phi_{\mathbf{k}}} \sin \theta_{\mathbf{k}} \cos \theta_{\mathbf{k}} \quad (\text{A2a})$$

and

$$c_{\mathbf{k}} = \frac{\omega_m}{2\omega_{\mathbf{k}}} \gamma h \cos \psi e^{2i\phi_{\mathbf{k}}} \sin^2 \theta_{\mathbf{k}} \quad (\text{A2b})$$

The perpendicular component of the microwave field is along the x-axis and $\phi_{\mathbf{k}}$ is measured with respect to this axis. The b_0 in Eq. (A1) is related to the uniform precession amplitude and is given by

$$b_0 = \frac{\gamma h \sin \psi}{2(\omega_0 - \omega)} e^{i\omega t} \quad (\text{A3})$$

if the antilararmor term in the transverse component of the linearly polarized microwave field is neglected. The f_k also neglects the contribution of this term to the coupling. For sufficiently large internal fields, the correction due to these antilararmor terms is small and may be neglected.

The first-order instability threshold is obtained from the equation of motion for the b_k ,

$$\begin{aligned} db_k/dt &= i \partial \mathcal{H} / \partial b_k^* \\ &= i [\Omega_k b_k + (f_k^* b_0 - c_k \cos \omega t) b_{-k}^*] \end{aligned} \quad (A4)$$

where $\Omega_k = \omega_k + i\eta_k$. Damping is taken into account by assigning an imaginary part η_k to the spin-wave frequency ω_k . The relaxation rate η_k is related to the spin-wave linewidth by $\eta_k = \frac{1}{2} \gamma \Delta H_k$. The instability threshold is obtained by determining the microwave field amplitude at which the equation of motion (A4) permit a stationary solution

$$b_k = b_{k0} e^{i\omega t/2} \quad (A5)$$

in the presence of damping. By considering only terms which vary as $e^{i\omega t/2}$ in db_k/dt and $e^{-i\omega t/2}$ in db_{-k}^*/dt , two homogeneous linear equations in b_{k0} and b_{-k0}^* result. The microwave field amplitude for which a non-trivial solution to b_{k0} and b_{-k0}^* exists corresponds to the instability threshold. From Eqs. (A4) and (A5), a nontrivial solution for b_{k0} is obtained only for

$$|\Omega_k - \omega/2| = \left| \frac{c_k}{2} - \frac{f_k^* \gamma h \sin \psi}{2(\Omega_0 - \omega)} \right| \quad (A6)$$

where the uniform precession frequency ω_0 has been replaced by Ω_0 in the expression for b_0 . The relaxation rate η_0 is related to the uniform precession linewidth ΔH by $\eta_0 = \frac{1}{2} \gamma \Delta H$. The right-hand side of Eq. (A6) is proportional to the microwave field amplitude h . Instability occurs for

the smallest value of h if the spin-wave frequency ω_k is equal to one-half the pump frequency ω . If $\omega_k = \omega/2$ is satisfied, the critical field is determined by

$$\eta_k = \frac{\omega_m}{\omega} \frac{\gamma h}{2} \left| \cos \psi \sin^2 \theta_k e^{i\phi_k} + \sin \psi \sin \theta_k \cos \theta_k \frac{(\gamma H_1 + \gamma Dk^2 + \omega/2)}{(\Omega_0 - \omega)} \right| \quad (A7)$$

The lowest threshold for a given magnon instability is realized for that value of ϕ_k for which the phases of the two terms inside the vertical bars of Eq. (A7) are equal. The threshold is given by

$$\frac{1}{h_{\text{oblique}}} = \frac{\omega_m \sin^2 \theta_k}{\omega \Delta H_k} \cos \psi + \frac{\omega_m \sin \theta_k \cos \theta_k (\omega/2 + \gamma Dk^2 + \gamma H_1)}{\omega \Delta H_k |\Omega_0 - \omega|} \sin \psi \quad (A8)$$

which is equivalent to Eq. (4).

It is important to realize that $\Omega_0 - \omega$ is negative and that the phase of $(\Omega_0 - \omega)^{-1}$, which is specified by the relative magnitudes of $\eta_0 = \frac{1}{2} \gamma \Delta H$, ω_0 , and ω , determines the ϕ_k which leads to the lowest threshold. For narrow linewidth materials, $\omega_0 \gg \eta_0$ is satisfied for sufficiently large applied fields and h_{oblique} corresponds to $\phi_k \approx \pi$. In general, however, the ϕ_k for which Eq. (A8) is valid is given by

$$\phi_k = \pi + \tan^{-1} [\eta / (\omega - \omega_0)] \quad (A9)$$

ACKNOWLEDGMENTS

The authors are indebted to E. Schlömann for helpful discussions concerning the theory of oblique pumping and to J. A. Hillier for making the measurements.

REFERENCES

- * The portion of this research performed by J. J. Green and C. E. Patton was supported by the Advanced Research Projects Agency of the Department of Defense and was monitored by Rome Air Development Center under Contract No. F30602-68-C-0005.
- + Operated with support from the U. S. Air Force.
- 1. H. Suhl, J. Phys. Chem. Solids 1, 209 (1957); see also Phys. Rev. 101, 1437 (1956).
- 2. E. Schlömann, J. J. Green, and U. Milano, J. Appl. Phys. 31, 386S (1960).
- 3. E. Stern, G-MTT International Microwave Symposium, Boston, 1967, IEEE Cat. No. 17C66, p. 103.
- 4. L. V. Kitaev, A. A. Goncharova, and G. I. Katamaran, Sov. Phys. Solid State 9, 246 (1967). Translation from Russian.
- 5. R. W. Damon, Rev. Mod. Phys. 25, 239 (1953).
- 6. J. J. Green, Scientific Report No. 2 (Series 2), Gordon McKay Laboratory, Harvard University, Cambridge, Massachusetts, December 1, 1959.
- 7. J. J. Green, J. A. Hillier, and J. H. Saunders, G-MTT International Microwave Symposium, Boston, 1967, IEEE Cat. No. 17C66, p. 100.
- 8. T. Holstein and T. Primakoff, Phys. Rev. 58, 1098 (1940).
- 9. D. Polder and J. Smit, Rev. Mod. Phys. 25, 89 (1953).
- 10. E. Schlömann, Technical Report, R-48, Research Division, Raytheon Company, Waltham, Massachusetts, October 1959.
- 11. The minus sign preceding the expression for f_k was omitted in Eq. (3.46) of ref. 10.

FIGURE CAPTIONS

- Figure 1** Experimental and theoretical microwave field threshold amplitudes for a YIG (1 percent Dy) sphere at 9.2 GHz as a function of the pump angle between the static magnetic field direction and microwave field polarization direction for an external static magnetic field of 400 Oe. The theoretical curves (solid lines) were obtained assuming transverse demagnetizing factors of $1/2$ and $1/3$, as explained in the text.
- Figure 2** Experimental and theoretical threshold amplitudes for a YIG (1 percent Dy) sphere at 9.2 GHz as a function of pump angle for an external static field of 600 Oe. The theoretical curve was obtained with a transverse demagnetizing factor of 0.38.
- Figure 3** Experimental and theoretical threshold amplitudes for a YIG (1 percent Dy) sphere at 9.2 GHz as a function of pump angle for an external static field of 1100 Oe. The lower theoretical curve was obtained by adjusting the dependence of the spin-wave damping on wave vector to give the best fit with a transverse demagnetizing factor of $1/3$. The two upper curves were obtained by considering parallel and perpendicular pumping processes which operate independently, as explained in the text.
- Figure 4** Experimental and theoretical threshold amplitudes for a YIG (1 percent Dy) sphere at 9.2 GHz as a function of pump angle for an external static field of 1500 Oe. The theoretical curve was obtained with no adjustable parameters, as explained in the text.
- Figure 5** Spin-wave frequency ω_k as a function of wave number magnitude k for \underline{k} parallel to the internal field direction ($\theta_k = 0$) and \underline{k} perpendicular to the internal field ($\theta_k = \pi/2$). The parallel pump instability for a spin wave at ω_k occurs at

$\theta_k = \pi/2$ and the perpendicular pump instability occurs at $\theta_k \approx \pi/4$ as indicated by the black dots. The oblique pump instability corresponds to an intermediate state, $\pi/4 < \theta_k < \pi/2$, as indicated by the open circle.

Figure 6 Equivalent circuit for the oblique pumping of a spin-wave state (ω_k, k, θ_k) with a microwave field polarization direction at an angle ψ with respect to the static internal field. The parallel and perpendicular pumping contributions are characterized by sources $h \cos \psi e^{i\omega t}$ or $h \sin \psi e^{i\omega t}$ and coupling coefficients $C_{||}$ or C_{\perp} , respectively.

Figure 7 The experimentally determined k-dependence of the spin-wave line width ΔH_k for parallel pumping in a 1 percent Dy doped YIG sphere at 9.2 GHz.

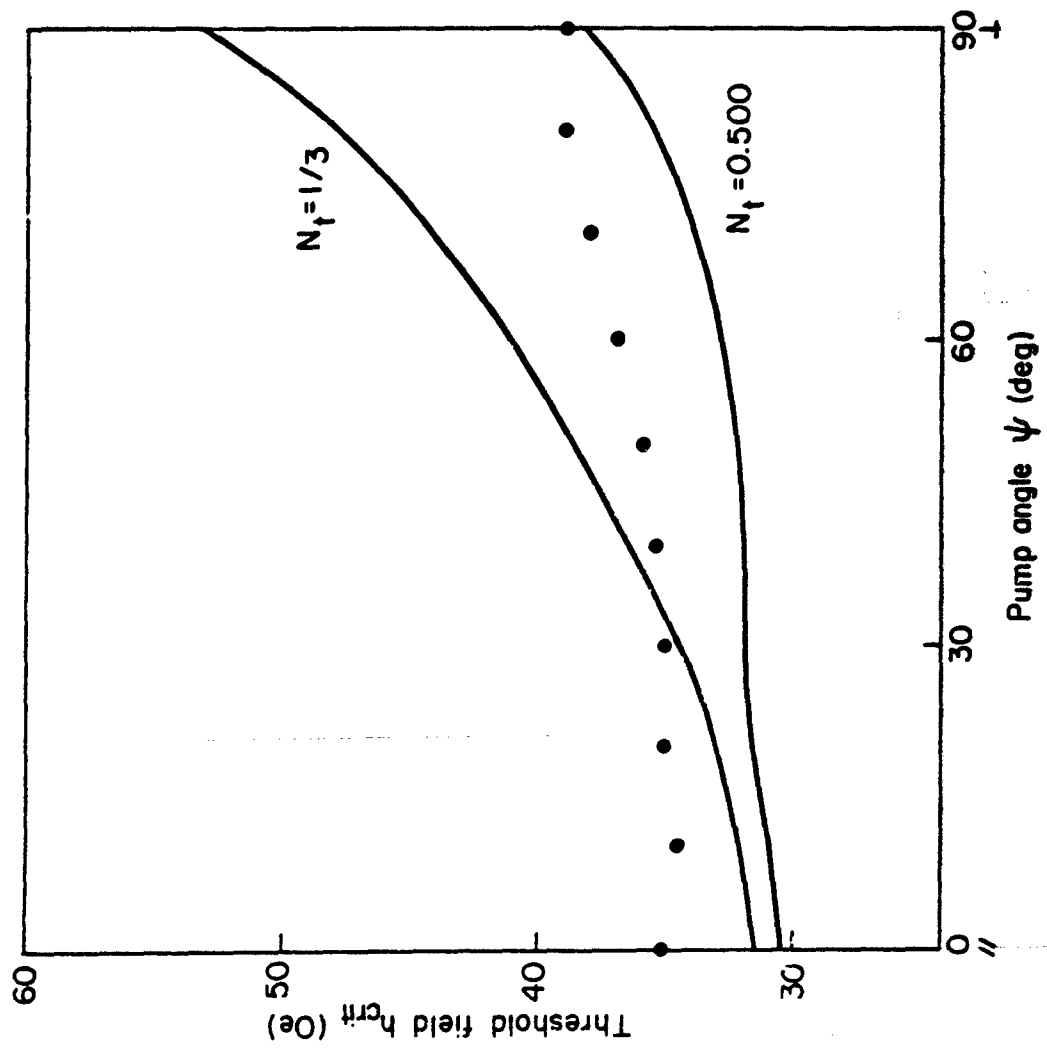


FIGURE 1

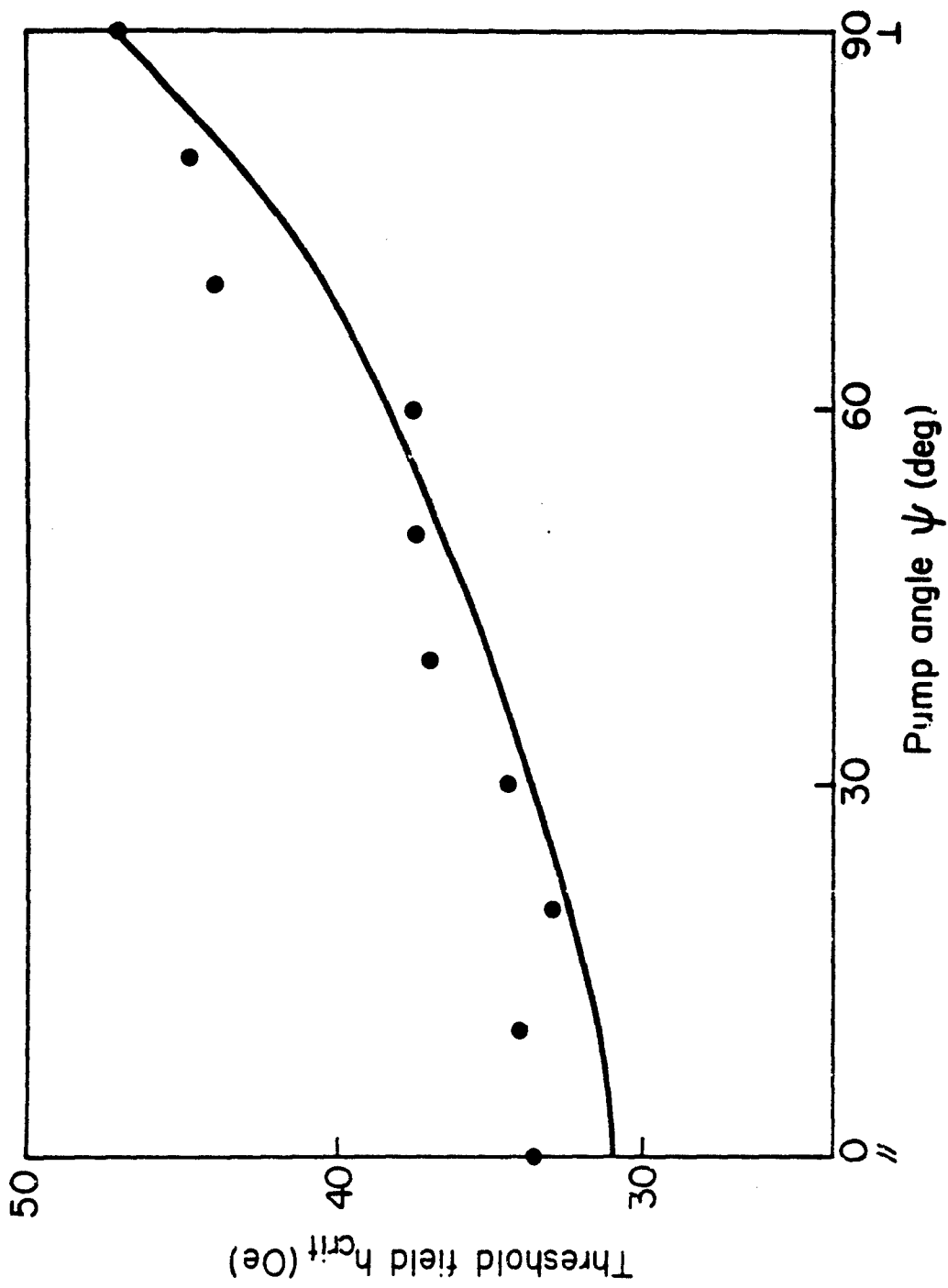


FIGURE 2

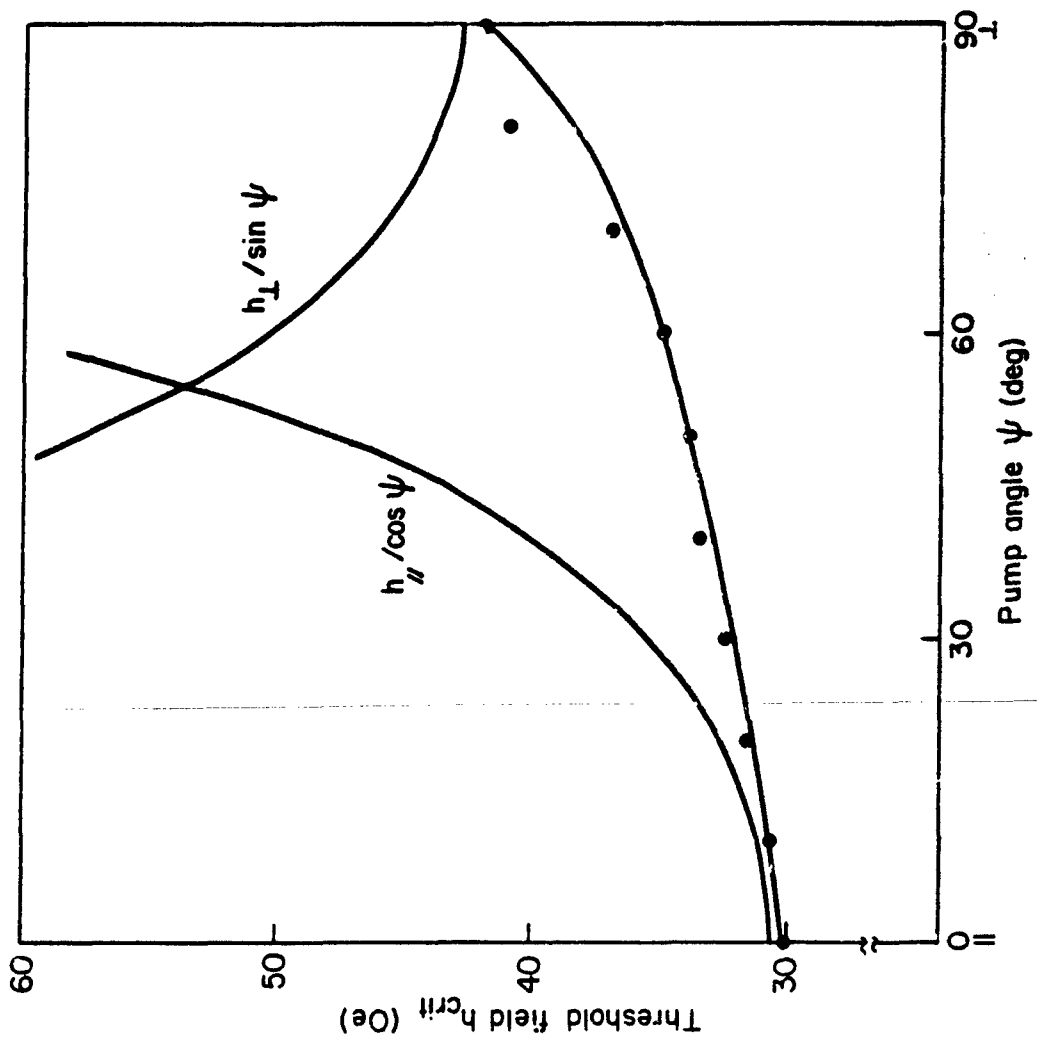


FIGURE 3

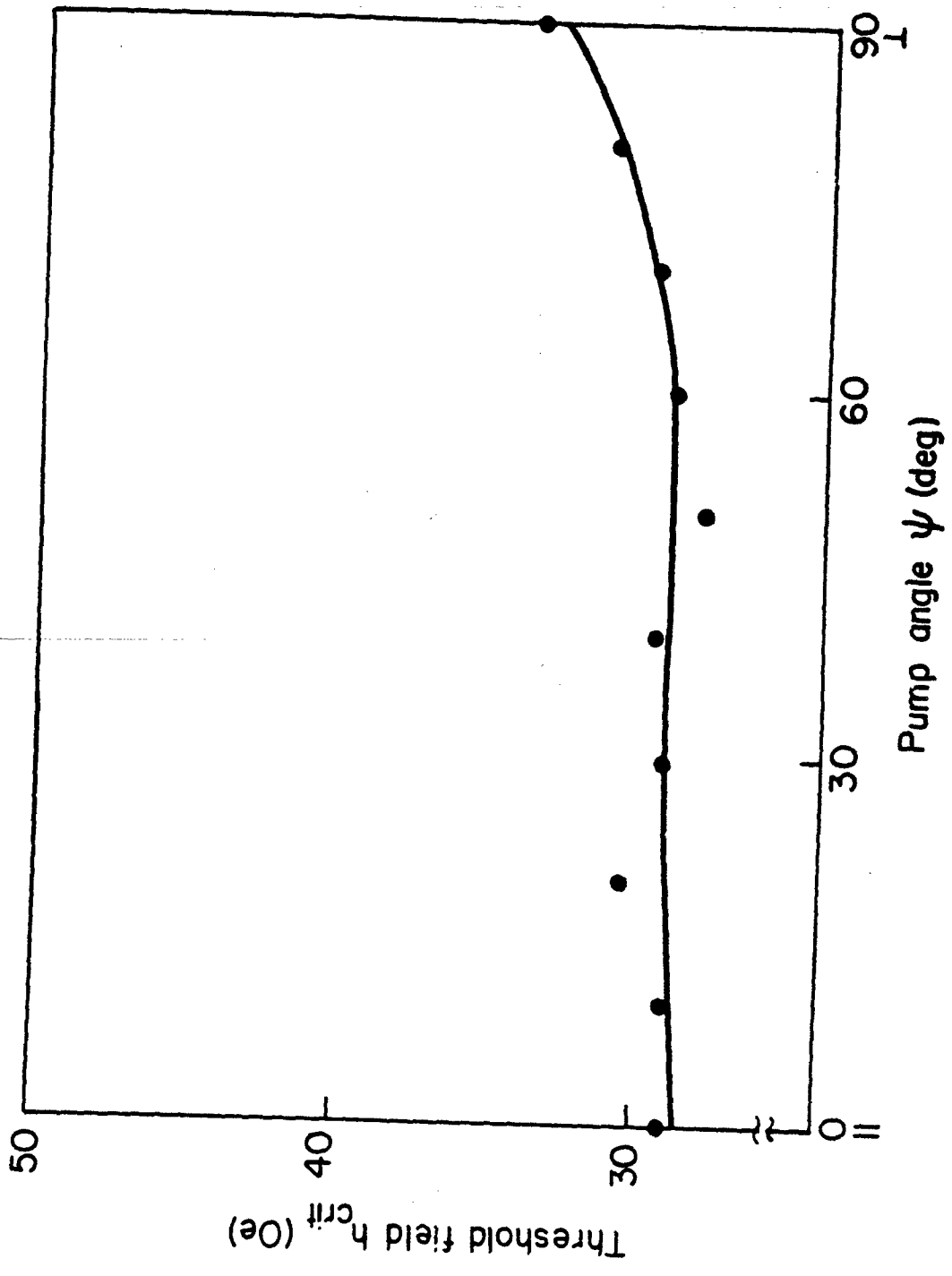


FIGURE 4

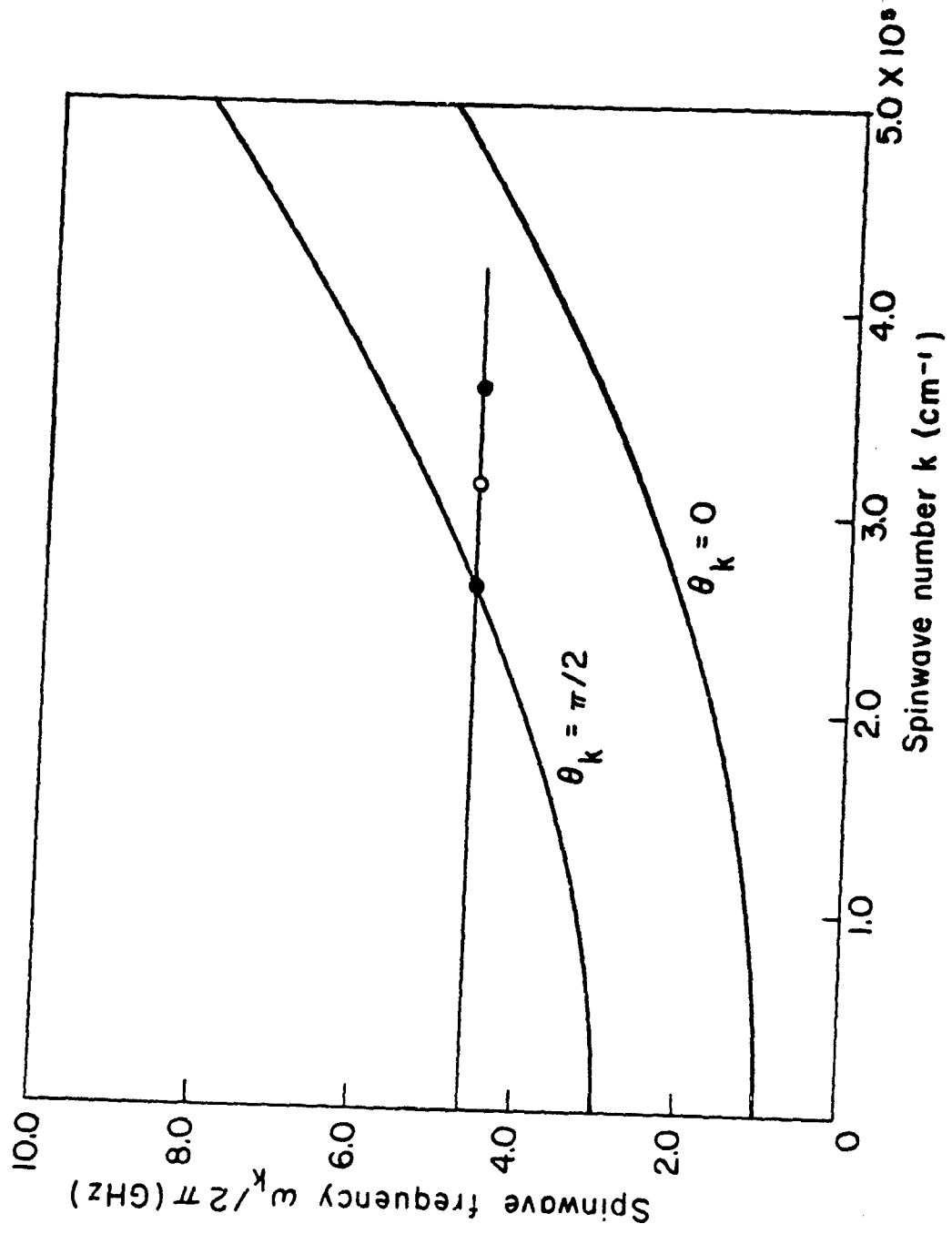


FIGURE 5

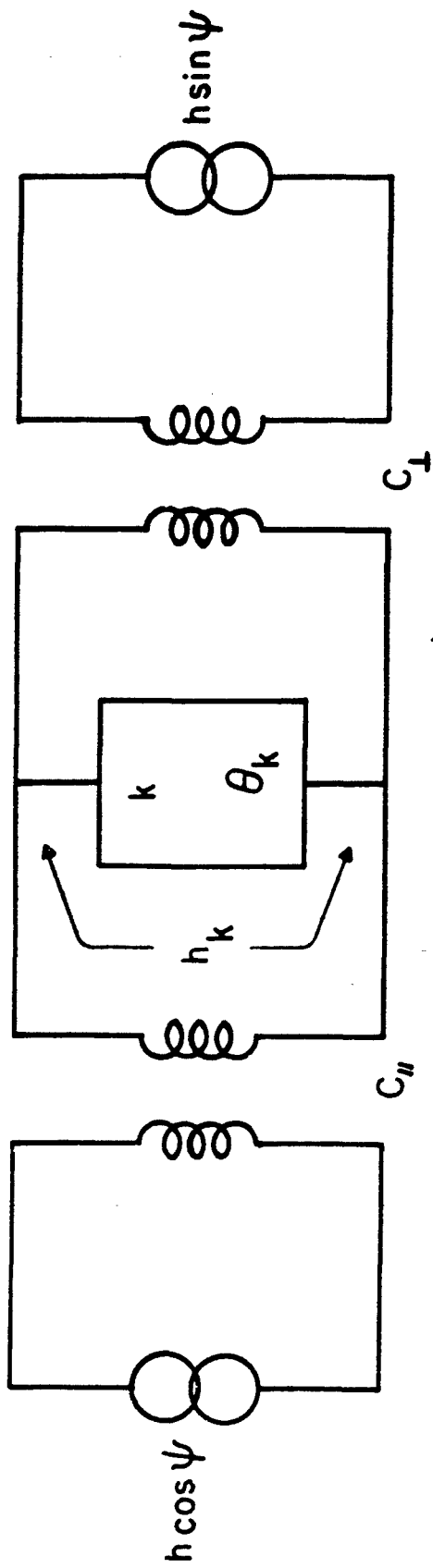


FIGURE 6

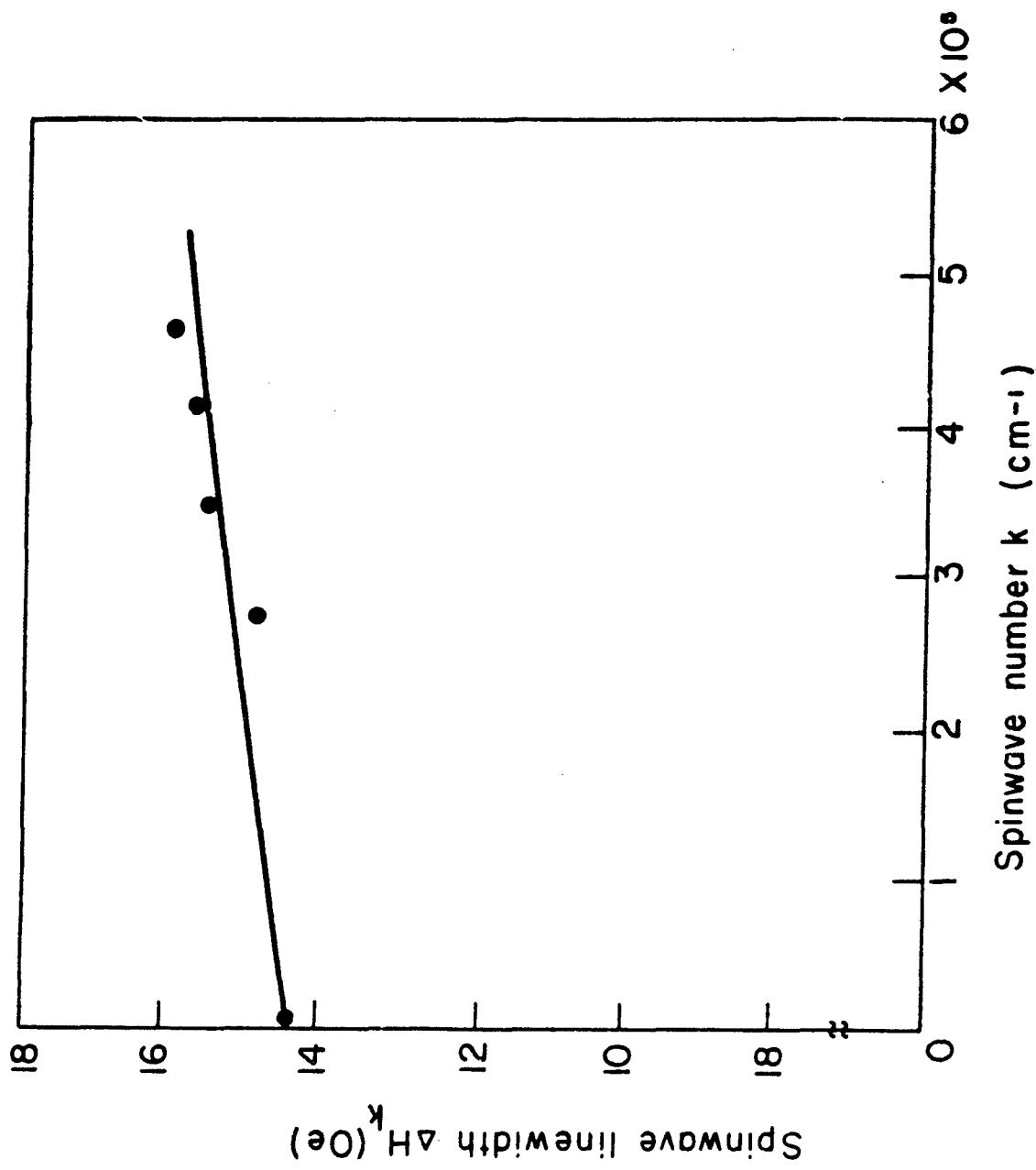


FIGURE 7

UNCLASSIFIED

Security Classification

DOCUMENT CONTROL DATA - R & D

(Security classification of title, body of abstract and indexing annotation must be entered when the overall report is classified.)

1. ORIGINATING ACTIVITY (Corporate author) Raytheon Company 28 Seyon Street Waltham, Massachusetts 02154		2a. REPORT SECURITY CLASSIFICATION UNCLASSIFIED	
		2b. GROUP N/A	
3. REPORT TITLE MICROWAVE PROPERTIES OF PARTIALLY MAGNETIZED FERRITES			
4. DESCRIPTIVE NOTES (Type of report and inclusive dates) Final Report (July 1967 - July 1968)			
5. AUTHOR (First name, middle initial, last name) J. J. Green, C. E. Patton, F. Sandy			
6. REPORT DATE August 1968		7a. TOTAL NO. OF PAGES 110	7b. NO. OF REFS 18
8a. CONTRACT OR GRANT NO. F30602-08-C-0005		8b. ORIGINATOR'S REPORT NUMBER(S)	
a. PROJECT NO. ARPA Order No. 550			
c.		9a. OTHER REPORT NO(S) (Any other numbers that may be assigned this report) RADC-TR-68-312	
d.			
10. DISTRIBUTION STATEMENT This document is subject to special export controls and each transmittal to foreign governments, foreign nationals or representatives thereto may be made only with prior approval of RADC (EMATE), GAFB, NY 13440			
11. SUPPLEMENTARY NOTES RADC PROJECT ENGINEER, EMATE Patsy A. Romanelli AC 315-330-4251		12. SPONSORING MILITARY ACTIVITY Rome Air Development Center Techniques branch Griffiss AFB, New York 13440	
13. ABSTRACT The microwave properties of partially magnetized materials have been investigated. The real parts (μ' , κ' , μ_z') of the components of the permeability tensor have been measured as a function of the ratios of saturation magnetization ($4\pi M_s$) to angular frequency (ω) and average magnetization ($4\pi M$) to angular frequency and location on the magnetic hysteresis loop on a yttrium iron garnet (YIG) and magnesium manganese ferrite (MgMnF). The off diagonal component, κ' , gives good agreement with Rado's prediction that $\kappa' \approx \frac{2\gamma M_s}{\omega}$. The diagonal components μ' , μ_z' do not fit Rado's prediction and the cause of the failure of Rado's analysis for μ' , μ_z' is suggested. The dependence of μ' , μ_z' upon $\frac{4\pi M_s}{\omega}$, $\frac{4\pi M}{\omega}$ has been empirically fitted by certain mathematical functions. The imaginary components (μ'' , κ'' , μ_z'') have been measured for $.7 < \frac{4\pi M_s}{\omega} < 1$ using circularly polarized cavities. For $\frac{4\pi M_s}{\omega} < .8$, it has been found that $\kappa'' \ll \mu''$ and that the loss of the partially magnetized state can be characterized by a single value of μ'' , that for the completely demagnetized state. For values of $\frac{4\pi M_s}{\omega} \leq .7$ large rectangular samples and exact the solution to the waveguide cavity mode have been utilized to obtain μ'' for the demagnetized state. The high power threshold has been measured on YIG as a function of sample shape, the polarization of the rf magnetic field and the orientation of the rf field to the static magnetization. The Suhl and Schloemann theories for high power non-linearity have been extended to include			

DD FORM 1473, NOV 65

UNCLASSIFIED

Security Classification

Best Available Copy

UNCLASSIFIED

Security Classification

14. KEY WORDS	LINE A		LINE B		LINE C	
	ROLE	WT	ROLE	WT	ROLE	WT
Ferrites Microwave phase shifter Garnets Tensor permeability						
13. Continued						
arbitrary ellipsoids, linearly polarized rf magnetic field, anti-Larmor circularly polarized rf magnetic field, and arbitrary orientation between the rf magnetic field and the static magnetization. The experi- mental data and the extended theory give good agreement for saturated samples. For thin disc geometries it has been found that the threshold is very critical to align- ment when the dc magnetic field is perpendi- cular to the plane of the disc. If a needle-like anti-parallel domain structure is assumed for the demagnetized state, then the experimental results for the demagnetized state can be explained in terms of the results of the saturated state.						

UNCLASSIFIED

Security Classification

Best Available Copy